INTERPLAY OF AXIS RATIO ON NEUTRON FLUX IN A SPHEROID NUCLEAR REACTOR CORE USING JACOBI ELLIPTIC THETA FUNCTIONS

By

Leting Silas Kering

A Thesis Submitted to the Department of Mathematics, Physics and Computing in Partial Fulfillment of the Requirements for the Degree of Doctor of Philosophy in Physics

Moi University

2022

DECLARATION

Declaration by the Candidate

This thesis is my original work and has not been presented for a degree in any other University. No Part of this thesis may be reproduced without the prior written permission of the author and / or Moi University.

Signature ……Date……

Leting Silas Kering

Phd/ Phy/004/13

Declaration by the Supervisors

This thesis has been submitted with our approval as University supervisors.

Signature ……Date……

Prof. Kapil. M. Khanna

Department of Mathematics, Physics and Computing

School of Sciences and Aerospace

Moi University

Signature ……Date……

Dr. Kiptiemoi.K. Korir

Department of Mathematics, Physics and Computing

School of Sciences and Aerospace

Moi University

DEDICATION

This thesis is dedicated to my beloved Wife Joyce Kering, My Sons Einstein K Kering and Leo K Kering to my beautiful Daughter, Angela C Kering.

ACKNOWLEDGEMENT

I sincerely acknowledge the relentless efforts played by My Supervisors Prof K. M Khanna and Dr.K. K. Korir, who have offered immense support to nurture me in the world of theoretical Physics. The members of the school of Pure and Biological sciences of Moi University did an excellent work in shaping my academic journey. The dean of the school of science, Prof Ambrose Kiprop, Coordinator head of Physics Department, Dr. Nyamwala have been instrumental in providing the required support.

Lastly, I lack words to describe the efforts of my Parents David Leting and Hellen Leting who went a mile extra to ensure that I completed my studies. Kerita Primary school, Tambach secondary school and Rurigi secondary schools were critical in offering me a strong foundation in Physics. I thank the Kenya Nuclear Energy and Power Agency (NUPEA) for the moral support and my employer the County Government of Uasin Gishu.

I give the Almighty God, Jehovah, Thanks.

ABSTRACT

The instantaneous neutron's density in a reactor core is influenced by several factors. Some of them include the reactor material's characteristics and the reactor configuration geometry properties. The role of the former has been well explored and understood while the latter continues to arouse interest in research and applications despite being poorly understood for some configuration types. In particular, spheroid configuration exhibits relatively higher robustness compared to other. However, the behavior of time dependent neutron flux at varying axis ratios and how the latter affects neutron leakage rates has not been well explored for this type of configuration. Therefore, this study is aimed at establishing how the axis ratio determines the behavior of neutron flux and neutron leakage rates. Specifically; modeling and determining the behavior of time dependent neutron diffusion flux in a spheroid reactor core at varying axis ratios, formulating the relationship between the axis ratio and neutron leakage rates and elaborating the behavior of neutron leakage rates for both spheroids at axis ratios equal, smaller and larger than unity. In order to carry out this, Fick's law of diffusion was modified into a Jacobi elliptic theta function to describe the desired time dependent neutron diffusion problem in spheroid coordinates system. The quasi-radial component was adapted to represent the axis ratio and thereafter appropriate boundary conditions were imposed. Secondly, a relationship between neutron leakage rate and the axis ratio of spheroids was formulated using geometric buckling and neutrons thermal life time equations, and the results were evaluated for axis ratios equal, smaller and larger than unity with software used to solve all the formulated equations. It was found that neutrons diffuse outwards from the core towards the boundaries of the spheroid exhibiting the characteristics of Jacobi elliptic theta curves of the third kind. Various configurations of diffusion configurations were obtained that included ternary surfaces, continuous and discontinuous surfaces of various characteristics as the value of 'n' was varied. In addition, neutrons diffusion behavior along the quasi-angular component and the time component was found to be largely similar. In the investigation of neutron leakage rate versus the axis ratio, both configurations (with the same volume and same neutron leakage constant (k)) exhibited similar profile, although the neutron leakage rate for prolate was lower compared to that of oblate at axis ratios smaller than unity. In contrast, at axis ratios larger than unity, it was found that the neutrons leakage rate for prolate became greater than that of an oblate of the same volume. The results further showed that, at axis ratio larger than unity, the neutron leakage rate was mildly affected by the axis ratio of the spheroid. Finally, the values for neutron leakage rates for both prolate and oblate spheroids converged when the axis ratio was unity, for instance, the neutron leakage rates for both types of spheroids was 2.5 neutrons/square unit for neutron leakage constant of $k = 200$. The findings of this study could be utilized in the design of superior reactors with enhanced safety that can mitigate against nuclear accidents by varying core axis ratios in order to alter reactor criticality conditions. Further research needs to be conducted on multigroup neutron diffusion for a similar problem and determining the flux behavior for each type of spheroid separately

ACRONYMS

ARDC	Axis Ratio Dependent Component
TDC	Time Dependent Component
PWR	-Pressurized water reactor
BWR	-Boiling water reactor
CANDU	-Canadian Deuterium Uranium Reactor
AGR	-Advanced Gas Reactor
VVER	-Vodo-Vodyanoi Energetichesky Reactor
IAEA	-International Atomic Energy Agency
KNEB	-Kenya Nuclear Electricity Board
GCFR	-Gas Cooled Fast Reactor
LCFR	-Liquid Cooled Fast Reactor
MSR	-Molten Salt Reactor
SCWR	-Supercritical Water-Cooled Reactor
VHTR	-Very High Temperature Reactor
ICF	-Inertial Confinement Fusion
MCF	-Magnetic Confinement Fusion
DOE	-Department of Energy
PRA	-Probability Risks assessments
MSCR	-Molten Salt Cooled Reactor
LMFBR	-Liquid Metal Fast Breeder Reactor

DEFINITION OF SYMBOLS

Neutron thermal lifetime	$l_t,$
Neutron thermal lifetime when there is no leakage	$l_0,$
Neutron leakage rate	$L,$
Spheroid Semi-minor axis	$M_2,$
Spheroid Semi-major axis	M_1
Neutron and neutron thermal life time constant	k
Geometric buckling	(B_g)
Materials buckling	(B_m)
Azimuthal component of the wave function in spherical geometry	$Z(z)$ -
Radial component of the wave function in cylindrical geometry	$R(r)$
Bessel's function of the first kind	$J_0(Br)$
Bessel's function of the second kind	$Y_0(Br)$
Angular Variable of spheroidal coordinate system	η
Radial Variable of spheroidal coordinate system	ξ
Azimuthal Variable of spheroidal coordinate system	φ
Focal distance	c
Jacobi elliptic theta function of the third kind	ν_3
Azimuthal wave number	m
Core reactivity	ρ
Diffusion coefficient	D
Neutron velocity	v
Neutron thermal lifetime constant	k

TABLE OF CONTENTS

LIST OF TABLES

LIST OF FIGURES

CHAPTER ONE

INTRODUCTION

1.1 Background

A nuclear reactor generates nuclear energy through nuclear fission or fusion in a controlled system Ragheb (2015b). The current study focuses on fission based reactors. It is understood that nuclear reactors have naturally existed for billions of years (Petrov et al., 2006). However, the Second World War occasioned the need for powerful warfare weaponry, which gave rise to the development of nuclear bombs. The idea of utilization of nuclear reactors for civilian applications was conceived after 1945 (Röhrlich, 2013), and since then, significant progress has been made in nuclear reactor technology particularly for electricity production (Ripani, 2015). Nuclear electricity currently accounts for 11 % of global energy production and is projected to rise to 15% once all nuclear reactors have been commissioned (Findlay, 2010a). Nuclear energy possesses risks and challenges but remains an important source of energy today and in the future, if the current statistics were to remain the same (Findlay, 2010b). Developing nations are also including nuclear energy in their national energy mix because of these aforementioned reasons (Amano, 2011). Fusion-based reactors technology is yet to be commercialized because it's still in experimental stages (Jeffrey, 2007; Ongena, 2016).

Historically, reactors have evolved through four generations, this evolution has been informed by several factors that include: the need to enhance their resistance to proliferation, the need to develop economical designs, the need for ease of waste disposal, the need for increased sustainability, the need for reactors with smaller grids requirements, improvement of thermal efficiencies, modularization,

elongated lifespan, widening public acceptance (Goldberg & Rosner, 2011; Zelevinsky & Volya, 2017). Lately, events at Fukushima and Daichi involving reactor meltdown shifted attention to the enhancement of safety features to mitigate the impact of abnormal events without active controls (Zelevinsky & Volya, 2017). The events inspired the search for enhanced safety protocol in nuclear reactors.

Fission based reactors rely on the diffusion of neutrons to split heavy nuclei like that of Uranium, which in turn releases energy through chain reaction (Masterson, 2017; Murray & Holbert, 2014). Fick's law of diffusion plays a central role in understanding this process (Srivastava, 2020). Analytical and numerical methods based on Legendre polynomials and Bessel's functions have been adopted to study neutron diffusion problems in various geometry and one commonality is the process of neutron flux attenuation as the wave propagates away from the source. This common finding was made elaborately for different types of reactor geometry; cylindrical geometry, spherical geometry, cubical geometry and for a point source. In all these studies, the neutron flux and its associated geometric buckling for the configuration were evaluated; the geometric buckling was understood as the first eigenvalue of the neutron diffusion problem (Carayannis et al., 2020; Ragheb, 2015a). Sjoestrand (1958), gave the earliest method for the computation of flux and the relationship between the axis ratio and the geometric buckling of a reactor and remains relevant to date. However, the determination of the relationship between the axis ratio of the spheroid and the flux was not determined explicitly.

Multigroup neutron diffusion problems have also been considered. Studies have shown that fast neutrons have lower flux because the population of such neutrons inside the nuclear reactor is relatively lower compared to thermal neutrons, (Sjöstrand et al., 1959).

Neutron flux and neutron leakage rates in cylindrical and spherical geometry, unlike spheroid geometry, have been studied fairly well. This is partly attributed to the wide applications of such geometry in nuclear reactor designs (Linde, 1960), with the main advantage being the ease in fitting nuclear fuels to the core compared to spheroid geometry and their relative robustness (Bektas, 2017; Kim & Kim, 2013)

The relationship between flux and the semi focal distance of the spheroid has been explored by Zeppenfeld (2009), and the results showed that a slight deformation of the sphere does not affect the fundamental mode properties significantly at least to the first order. Secondly, it was found out that a disk and a sphere are two limiting cases for the spheroids that exhibited smooth transitions between two limits. Thirdly, full contours were found to be nearly circular near the source but slowly develop into elliptical shapes moving towards the boundaries.

The diffusion in spheroids has been done for other physical phenomena and adopted in this study for comparison. The works of Alassar (1999) discuss numerous applications of wave equations in spherical coordinate systems and were used to explain eigen -functions and eigen - frequencies of spherical mirror resonators. Paraxial approximations have been found useful in this study for reducing quasi radial and quasi angular functions.

The time-dependent heat diffusion equation that uses the method of Jacobi elliptic theta function was adopted to explore heat leakage in spheroids; where it was concluded that a slight deformation of the sphere does not affect the fundamental modes at least to the first order (Alassar et al., 2014; Lima et al., 2004). The Galerkin method (Carmo & Lima, 2008; Vega Carrillo, 2014)was proposed to be useful in solving diffusion problems in ellipsoidal geometry and found that Spheroids exhibit the tip effect whereby an area with a high moisture gradient is more significant since the aspect ratio was found to directly influence drying process; this study provided a macroscopic equivalent of the problem under study.

Whereas it is important to note that reactor reactivity is affected by temperature and other conditions, the role of reactor design remains a fundamental factor in the criticality formula (Qvist & Greenspan, 2012). Alassar et al. (2014), also provides a study on the behavior of neutron decay constant versus focal semi distance. This problem was solved using analytical and Monte Carlo methods, which showed that at small focal semi distance, neutron decay was relatively higher, however, as focal semi distance increases; neutron decay was observed to decrease exponentially. In a study on heat leakage rates, (Lima et al., 2004) showed that when volume was kept constant and at large axis ratios, there was little dependence on the heat transfer rate on the axis ratio.

From the foregoing discussion, it is evident that the role of axis ratio in the design and optimization of nuclear reactor has not been comprehensively studied, yet a proper understanding of the role of axis ratio in the determination of flux, leakage and reactor reactivity has a profound consequence on the improvement of reactor designs. For instance, an in-depth understanding of the effects of variation of axis

ratio with; neutron flux, neutron leakage and reactor core reactivity will have two main likely applications; first, in reactors that have been designed as Spheroid geometry and secondly in reactors that are non-spheroidal geometry but are slowly deforming with time. In both cases, the understanding will enhance design of reactors with improved efficiency and in mitigation of extreme events.

1.2 Statement of the Problem

The solution of diffusion problems for neutrons in spheroids has had several limitations that include; complexity of the resulting eigenvalues and eigenfunctions, emerging orthogonality problems and inseparable boundary conditions. Therefore, studies have mainly been focused on spherical and cylindrical geometry. Scientists and engineers have relied more on computer software to simulate neutron diffusion problems in spheroid geometry. There is a need to develop new mathematical models that simulate such problems in light of the current knowledge.

The model provided in this study adopts Jacobi's elliptic theta functions to solve these problems and the results are validated using the analytic method. The solutions are then applied to study neutron diffusion in the spheroid coordinate system. The understanding of neutron diffusion for such curved surfaces has not only proved complicated in dealing with neutron diffusion problem particularly where time-dependent neutron diffusion in 3-Dimensions is being considered. Secondly, unlike previous methods that had little or no consideration of the axis ratio, the new method provides an explicit relationship between the time-dependent flux and the axis ratio of the spheroid. Furthermore, the behavior of neutrons leakage outside a spheroid has been provided.

Unlike previous methods for determining leakage of neutrons in spheroids that have been provided in literature, the current provides a unique method that introduces a new term called neutron thermal lifetime constant which enables computation of leakage rates at various values of thermal lifetime constant and axis ratio of the spheroid, which enhances the computation of leakage rates at various axis ratios. The introduction of neutron thermal lifetime constant and axis ratio in the formula is a fairly new concept and has been incorporated in the relationship. In a similar manner, a new relationship between reactor core reactivity and the axis ratio was also developed.

Poor understanding of the diffusion problems in spheroid nuclear reactors could lead to nuclear accidents. In practice, even reactors that were initially spherical or cylindrical could get deformed as discussed thus consequently, the undetected deformation could result in the continued use of incorrect safety protocol and may lead to occurrences of accidents.

1.3 Justifications

- The rapidly growing demand for clean and sustainable energy to satisfy current and future global energy needs.
- The growing need to develop nuclear reactors that have enhanced safety protocol.
- The need to develop solutions for better understanding diffusion of neutrons in the curved spheroid reactor core configurations.

1.4 Objectives

1.4.1 Main Objective

Study the behavior of neutron flux, neutron leakage rates, and core reactivity under varying axis ratios in spheroid coordinate system using the method of Jacobi elliptic theta functions.

1.4.2 Specific objectives of Study

i. To formulate an appropriate time-dependent neutron equation with flux variation dependent on the axis ratio of the spheroid.
ii. To analyze time-dependent of and axis ratio of the spheroid core.
iii. To examine the effects of neutron leakage rates on the axis ratio of a spheroid.
iv. To investigate the effects of core reactivity and axis ratio on the spheroid.

1.5 Scope of the Study

- Neutron diffusion is being considered for spheroids without reflector walls
- Only thermal neutrons are being considered
- The neutron flux has been carried without distinguishing between the flux's behaviors for each type of spheroid separately

1.6 Significance of the Study

The results obtained from this work may assist in the improvement of reactor designs, where a comprehensive understanding of the flux behavior, leakage rate patterns, and core reactivity under varying axis ratio may lead to:

i) Optimal reactor designs that can have reduced core sizes which consequently have a less fuel-moderator assembly. This implies that such reactors are economical and reduces waste disposal challenges.

ii) Spheroids are generally robust compared to other forms of geometry, and in case of mechanical deformation due to heating, radiations and mechanical forces (including earthquakes), computer simulations can be developed that can assist in proper planning of reactor shutdown during such times

iii) Even reactors that are originally spherical and cylindrical, the effects stated in 1.4(ii) above are found to cause them to deform into spheroids. Thus, planning of mitigation measures in times of adverse events can be put in place.

iv) Therefore, this study is in line with Generation IV technological goals that laid down the requirements for safe, economical and reliable reactors.

1.7 Thesis Layout

This thesis is divided into six chapters as follows; - Chapter one gives the introduction to the subject matter. Chapter two provides a discussion of the subject in the context of related recent relevant studies that are available in literature. Chapter three gives the methodology that was adopted in the study while Chapter four provides a results and a detailed discussion of the results. Chapter five and six provides the conclusions and recommendations respectively

CHAPTER TWO

LITERATURE REVIEW

2.0 Introduction

In this section, we trace the development of various reactor geometries, considerations that have informed nuclear reactor design in the past and the present, the methods and approaches that have been used to study diffusion theory and their gaps, an overview of the concepts used to study leakage and reactivity in spheroid geometry and that of other physical phenomena are presented. A review of the diffusion of neutrons in other geometries and other physical phenomena is provided for comparison with this study. A literature review of key terms and concepts central to the current study have been provided.

The role of the moderator in a reactor core (Figure 2.1) slows down fast neutrons into thermal neutrons to be able to initiate chain reaction (Van Dam et al., 2005). There are many types of reactor core geometry where the main ones include spherical, cylindrical and cubical. Spheroid geometry has not been well applied due to the complications associated with such curvatures. We have provided a review of diffusion in a sphere which is a special case of a spheroid. Cylindrical geometry has some inherent properties of curved geometry such as emergence of eigenvalues and that justifies their inclusion in this study.

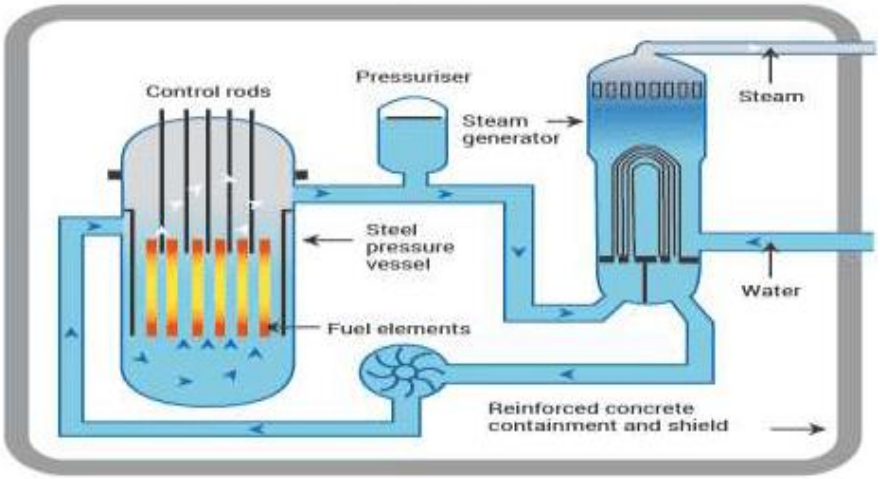

Figure 2.1: Schematic diagram of Pressurized Water Reactor Showing the Spheroid Nature of Such Design (https://world-nuclear.org)

The control rods are used to regulate chain reaction by lowering or withdrawing them from the core. They are made from materials with high neutron absorption cross-section such as Boron. Such materials are also known as neutron poison (Hannaske et al., 2013; Plompen et al., 2020). Figure 2.2 illustrates a reactor core fitted with fuel pellets and control rods.

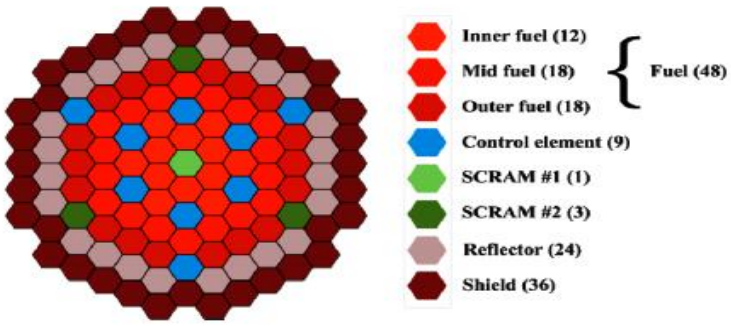

Figure 2.2: Showing a Cylindrical reactor core fitted with nuclear fuel

In cylindrical geometry, such a core is fitted by interfering with the smooth walls of the inner reactor walls. It was established that performing such fittings in

spheroidal geometry was bound to present more difficulties due to the associated curvature complexities.

The diffusion of neutrons through a reactor core results in their moderation as they undergo collisions with the fuel-moderator assembly leading to the production of thermal neutrons. The later have energy range within the fission cross-section of most nuclear fuel such as Uranium, Thorium, and Plutonium (See Table 2.1). This means that they possess a higher probability to cause fission and avoid absorption with the fuel-moderator assembly. Therefore, thermalization is essential to ensure that reactor criticality is attained for sustainability.

Table 2.1: Showing Cross sections for different nuclear fuels Neutron parameters for ANL-800

	Nuclide	Neutrons per fission event	Fission cross section	Capture cross section	Transport cross section
1.	Plutonium(239)	2.98	1.85	0.260	6.8
2.	Uranium(235)	2.6	1.40	0.250	6.8
3.	Uranium(238)	2.6	0.095	0.16	6.9
4.	Fe	-	-	0.006	2.7
5.	Na	-	-	0.0008	3.3
6.	Al	-	-	0.002	3.1

(Agency, 2015)

Uranium is a nuclear fuel that is commonly used in nuclear reactors (Caldicott, 2013; Murty & Charit, 2013). Plutonium exhibits the highest neutron per fission event than Uranium thus making it a better nuclear fuel. However, its applications are limited due to its less relative abundance and higher rates of proliferation. Nuclear cross-sections play a significant role in the thermalization of neutrons. Materials with comparative nuclear cross sections as the neutrons tend to absorb

them at a higher threshold. Consequently, such materials are not good for the Fuel-moderator assembly. The population of neutrons inside a nuclear core at any given time can be said to be decreasing, remaining constant or increasing (Ayyoubzadeh et al., 2012).

A term referred to as the reactor criticality defined in equation 2.01 and 2.02 is used to measure the changes in the core instantaneous neutron population. The neutron multiplication factor, which is the ratio of the number of neutrons produced in one generation to that produced in the previous generation, is used to define reactor criticality. It depends on a four variables term also known as the four-factor formula stated in equation 2.01;

$$\boldsymbol{k = \varepsilon \eta f P} \qquad 2.01$$

Where;- ε - Neutron fast fission factor, $\eta -$ Average neutron per fission , f - Neutron Thermal factor ,P-Neutron escape probability. These terms have been well further expounded in section 3.1.5 of this Thesis.

In a practical reactor set up, leakage of neutrons is bound to occur. Therefore, instead of using the infinite multiplication factor, a related term called the effective multiplication factor (k_{eff}) is adopted. This term considers the thermal non-leakage probability, fast non-leakage probability and the infinite multiplication factor. It is a six-factor formula that is related to the four factor formula as shown in equation 2.02.

$$k_{eff} = k_{\infty} \varepsilon \eta f P \qquad 2.02$$

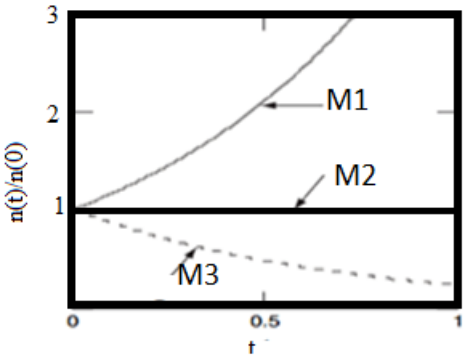

Figure 2.3: Showing Reactor Criticality Conditions (M1-Supercritical state, M2-Critical state, M3-Subcritical state)

Based on the effective multiplication factor, k_{eff}, three reactor criticality conditions are observed for an infinite reactor core (See Figure 2.3). **M1**, refers to a condition in a nuclear reactor core when the population of neutrons keeps increasing as time progresses. It is also called a supercritical system and causes the system to be self-sustaining. Secondly, the condition, **M2**, also called a critical state causes the system to be self-sustaining and indicates a condition when the population of neutrons remains the same even as time progresses in a reactor core. Lastly, **M3**, is known as a subcritical state and causes the system not to be self-sustaining and refers to the reactor core when the population of neutrons is decreasing as time progresses.

The applications of curved geometry in nuclear reactor cores and their cooling systems have been considered in the past and have been gaining popularity with Pressurized water reactor, Gas Cooled reactors, and Water-cooled reactors among others. This is because curved geometry possesses salient robust characteristics that are outstanding over the other geometry.

The design of the tower for the cooling the reactor is spheroid configuration with a wide at the top and the base (See Figure 2.4). The wider top enables hot air from

inside of the reactor core to mix freely with the atmospheric air for efficient cooling. Straight beams are used to build the tower making it resistant to external forces compared other geometry besides offering adequate space. This robustness in the reactor geometry is key component that continues to be explored particularly in reactor cores designs save for the practical complexities it portents.

Figure 2.4: Cooling towers of nuclear reactors that are Hyperbolic Paraboloids

(Bektas, 2017).

2.1 Behaviour of Neutron Flux in Non-Spheroidal Geometry

A sphere and a disc are considered to form special case of spheroid geometry, Rajai et al (Lima et al., 2004). It follows therefore that certain aspects of spherical geometry could be extended to spherical geometry and vice versa. So whereas this study is premised on spheroid geometry, the neutron flux and associated geometric buckling for members of non-spheroidal geometry that include spherical, cylindrical, and cubical, among others have been included for comparison. A summary table of flux and geometric buckling for the various types of reactor geometry is presented in Table 2.2.

Table 2.2: Summary of the geometric buckling and flux for various nuclear reactor geometry

	Geometry type	**Geometric Buckling**	**Neutron Flux**
i	Spherical	$B^2 = \left[\frac{\pi}{R_{ext}}\right]^2$	$\varphi(r) = A\frac{sin\left[\frac{\pi}{R_{ext}}\right]}{r}$
ii	Finite Cylinder	$B^2 = \left\{\frac{2.145}{R_{ext}}\right\}^2 + \left\{\frac{\pi}{H_{ext}}\right\}^2$	$\varphi(r) = AJ_0\left\{\frac{2.405r}{R_{ext}}\right\} cos\left\{\frac{\pi z}{H_{ext}}\right\}$
iii	Cubical	$B^2 = \pi\left[\frac{1}{a^2} + \frac{1}{b^2} + \frac{1}{c^2}\right]^2$ Where and c are the sides of a parallelepiped.	$\varphi(x,y,z) = A\, cos\left\{\frac{\pi x}{a}\right\} + cos\left\{\frac{\pi y}{b}\right\} + cos\left\{\frac{\pi y}{c}\right\}$
iv	Point source		$\varphi(r) = \frac{S_0}{4\pi rD} e^{-r/L}$

The equations in the table 2.2 can be understood better by looking at the graphs depicting the behavior of the neutron diffusion presented in Figure 2.5(i) (ii) for cylindrical geometry. It is common evident that the amplitude of the neutron flux propagation is higher at the beginning of the wave and slowly attenuates as the wave progresses towards the end of the dimensions of the respective geometry far from the source, a commonality with all the physical waves.

In a finite cylinder, the flux is described as a Bessel function of the first kind(Y) as demonstrated by the Figure 2.3(i) while for an infinite cylinder; the neutron diffusion is a Bessel function of the second kind (J) figure 2.3(ii)

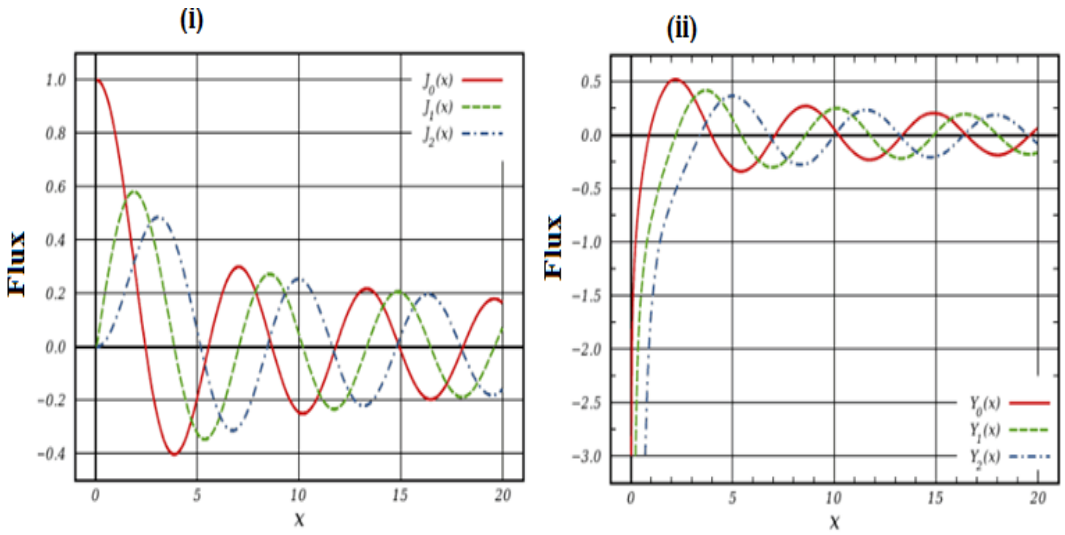

Figure 2.5: Neutron diffusion for (i) Finite cylinder and (ii) Infinite Cylinder

(Ragheb, 2006)

In spherical geometry, Figure 2.6(i), it is observed that flux drops from maximum and falls to a minimum in a behavior that is proportional to the reciprocal radius of the sphere. The amplitude of the flux was considered to attenuate faster for smaller radii than for larger radii. The second observation was that while the exact neutron flux theory predicts neutron flux vanishing at the walls of the reactor, diffusion theory predicts that flux vanishes at an extrapolated distance as shown in Figure 2.6(ii). This observation is not practically the case since the exact flux differs by flux dropping to a minimum then remaining at a plateau stage as it propagates towards the extrapolated distance. Thirdly, the difference in flux between fast and thermal neutrons was discussed and presented in Figure 2.6 (iii), where it was realized that fast neutrons flux remains unaffected by a boundary or a reflector, and is attributed to the fact that in practice fast neutrons do not get absorbed by nuclear cross-sections of materials. The neutron flux for a point source is seen to behave like an exponential decay, see Figure 2.6(i). A point source can then be considered as a sphere with an extremely small radius.

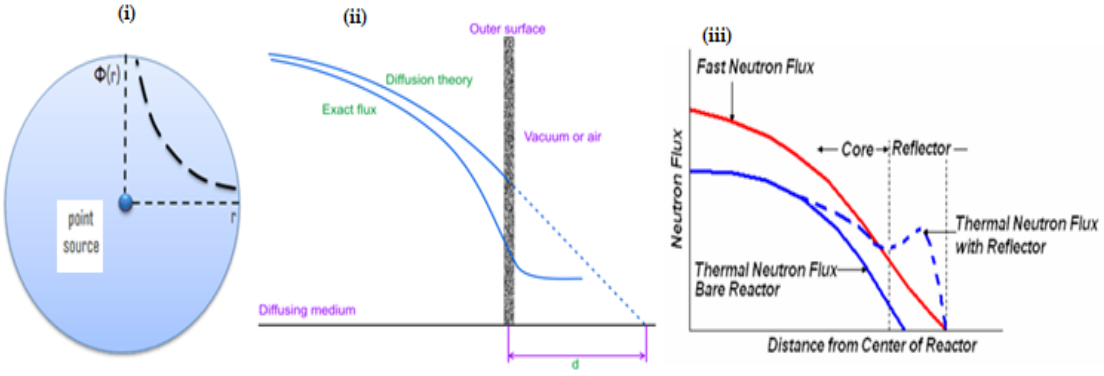

Figure 2. 6: Neutron flux for (i) a point source (ii), spherical reactor flux for thermal neutrons, (iii) and fast neutrons

(Sjoestrand, 1958).

In a study Apostol et al., 2010 discretization was achieved using the numerical technique on the Finite Differences Method where it was established that the smoothness of neutron distribution curves in 3-D figures was reliant on the number of mesh points present. More mesh points were observed to increase the smoothness of the curves.

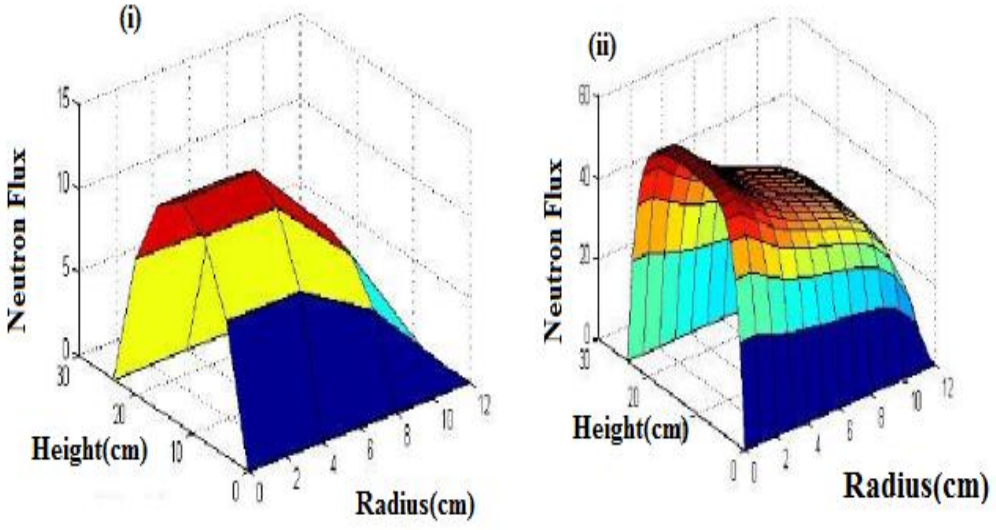

Figure 2. 7: Three dimensional surfaces in cylindrical geometry

(Zeppenfeld, 2009)

2.2 Behavior of Neutron Flux in Spheroid

It is worth noting that the field of curved geometries has attracted numerous studies in the past and has continued to arouse interest in recent times, (Zeppenfeld, 2009). However, many of these studies have focused mostly on non-spheroidal geometry due to the constraints that have been discussed hitherto.

To address some of these challenges, several proposals have been advanced. To begin with, the problem of inseparable boundary conditions was solved using the extrapolation distance method (Walters et al., 2018). Secondly, eigenvalue problems were solved using Real-time Analysis for particle transport Insitu (RAPID) solutions (Williams, 1986). In this methods, more accurate fission matrix values near radial and axial reflectors are obtained using the method.

A study on Neutron flux in spheroidal, spherical and toroidal geometry in non-absorbing media Blokhin et al. (2015) showed that spheroidal geometry has equivalent spherical approximation that gives accurate values of rates of absorption.

The spatial distribution of neutrons in a reactor core computed using both analytical and Monte Carlo method (Lima et al., 2004; Zeppenfeld, 2009), showed that disks and spheres are special cases of spheres. Furthermore, it was established that a slight deformation from a sphere has a mild effect on the fundamental mode properties of a sphere at least to the first order. In addition, full contours are formed and found to be nearly circular near the source but slowly develop into elliptical shapes moving towards boundaries.

The behaviour of neutron flux diffusion against its energy is an important subject particularly in this study. One research, Blokhin et al., 2015, modelled how flux

versus the neutron energy for Molten Salt Reactor (MNSR) using Low enriched Uranium Oxide (LEU-U02), (See Figure 2.8).

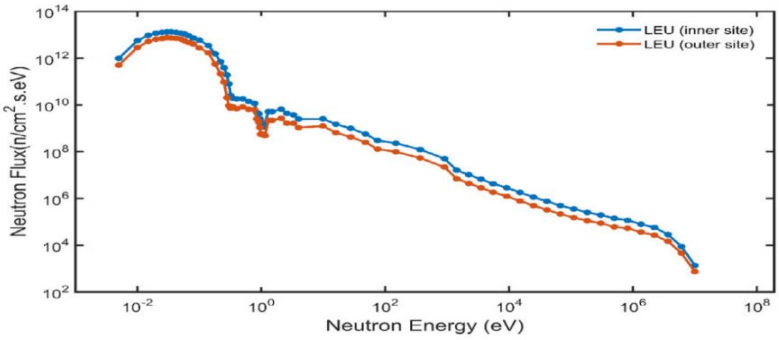

Figure 2.8: Behavior of neutron flux as a function of Neutron energy in an MNSR for LEU-UO2
(Falloon et al., 2003)

The results showed that the flux inside the reactor core was always higher than that outside the reactor for any energy value. Secondly, the presence of oscillations from the rather smooth curve was observed between (0 - 1 eV). This was attributed to the cross-sections of the materials in the fuel moderator assembly, and at such energies, absorption of neutrons was more pronounced.

In the study of diffusion of physical phenomena other than neutrons in spheroids. A number of studies have presented observations that are significant to this study. For example, the works of Li et al. (2004) discusses numerous applications of wave equations in spherical coordinate systems, where they have been used to obtain an exact treatment of scattering by a conducting disc or diffraction through a disc in infinite media. It was applied in a short wavelength range to the equation in the oblate spheroid system leading to Gauss Laguerre solutions to the paraxial approximation in optics. The paraxial approximation has been used to explain phenomena such as propagation of beams through the lens system, wavefront in

curvature and phase shifts in the focus of beams as well as eigen-functions and eigen-frequencies of spherical mirror resonators.

The time-dependent heat diffusion equation problem has been considered Shqair et al. (2019), adopts Jacobi elliptic theta function to understand the problem of leakage heat from spheroids.

The drying of grains in spheroids (Lima et al., 2004), provided a macroscopic comparison to the problem adopted in this study. The problem was investigated using the Galerkin method which proved useful in solving drying and cooling of solids in spherical and ellipsoidal geometry. The results established that Spheroids exhibit the tip effect whereby an area with a high moisture gradient is more significant since the aspect ratio was found to directly influence the drying process. The dimensionless moisture content at any location inside the spheroid was found to decrease with increasing Fourier number.

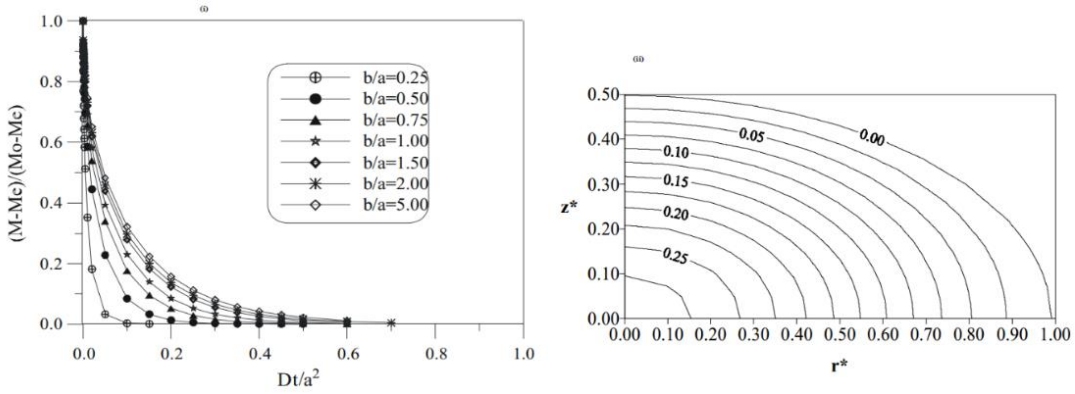

Figure 2. 9: The dimensionless moisture content as a function of (i) aspect ratio (ii) radius (Carmo & Lima, 2008)

2.3 Neutron Leakage and Reactor core reactivity in Spheroids

A related problem was presented by Ayyoubzadeh et al. (2012), that involved the variation of effective multiplication factor and Neutron decay constant investigated against focal semi distance. The problem was solved using analytical

and Monte Carlo methods. It was established that neutron effective multiplication factor decreased exponentially with increasing focal semi distance. However, a slight difference between the two methods was observed whereby; the effective multiplication factor was always slightly higher for Monte Carlo method than analytical method, Figure 2.10 (i). On the other hand, the neutron decay was observed to increase exponentially with increasing focal semi distance for both Analytical and Monte Carlo methods, Fig 2.10(ii).

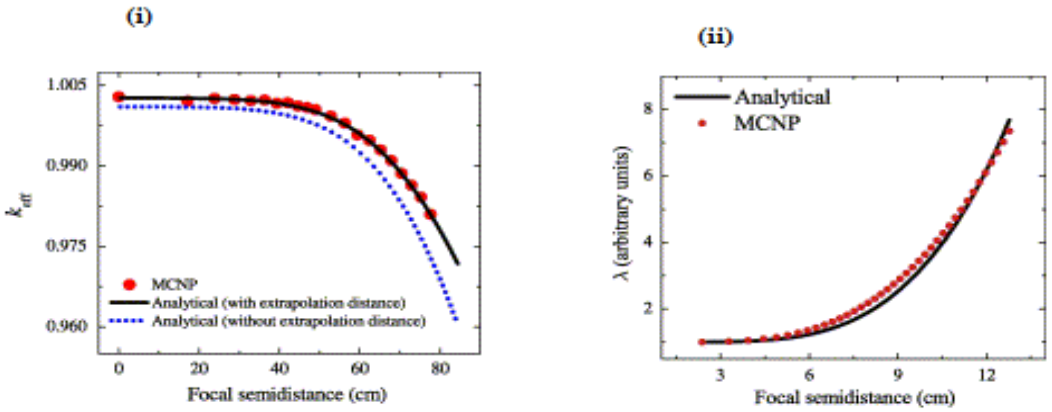

Figure 2. 10: Neutron's decay plotted against the semi focal distance (b) Neutron decay plotted against the semi focal distance
(Alassar et al., 2014).

In the study by Alassar et al. (2014), a differentiation between heat leakage in Prolate and Oblate spheroid was made. The study showed that prolates leak heat energy faster than oblate spheroids with the same axis ratio, Fig 2.11(i), and when the volume is kept constant and small axis ratios adopted, oblate spheroids were observed to transfer heat faster than prolate Fig 2.11(ii).

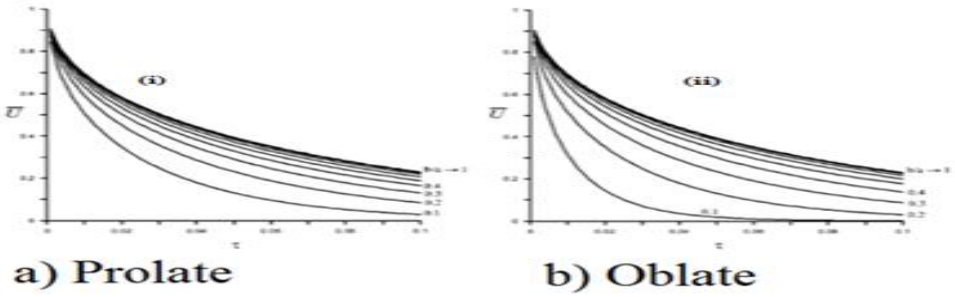

Figure 2.11: Heat leakage rates as a function of dimensionless time in (i) prolate (ii) Oblate (Vega Carrillo, 2014)

The leakage of neutron spectra from a Lead -Lithium spherical shell with a californium-deuterium source placed at the center was performed experimentally (Blokhin et al., 2015). The aim of the study was to measure the spectrum of leakage of neutrons from a 14 cm thick Lithium lead ($Li_{17}Pb_{83}$) spherical assembly with a 252 - Cf neutron source at its center and to verify the evaluated neutron data based on these measurements and earlier measurements with a 14 MeV source of neutrons. There was a slight variation between the experimental and theoretical results. Similar experimental designs were proposed for the current study to understand how the theoretical results could fit into the experimental results.

The results were as presented in Figure 2.12.

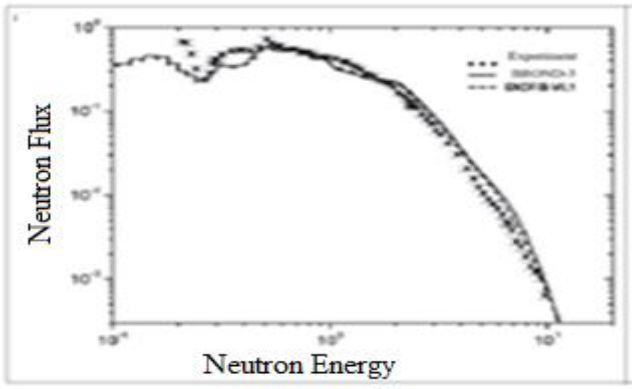

Figure 2.12: The variation of Neutron flux with the energy of the incident neutron
(Amano, 2011)

Solutions of two and four energy groups was studied in Welch et al. (2017), the method provided accurate results than analytical methods. Welch et al. (2017), also provided a study of the multigroup neuron problems in a heterogeneous reactor using Isogeomatic analysis (IGA) using NURBS (Non-Uniform Rational B-splines), It was shown that the rate of convergence of the higher order finite element schemes saturated for order greater than two. Woods and Palmer (2017) performed the discretization of transport equation using higher order finite element methods and established that complicated surfaces of the source and stream terms dominated the diffusion.

Jacobi elliptic theta functions have been dealt with extensively (Prasolov & Solov_ev, 1997). They have been applied in the study of Cosmology using the Friedmann-Robertson-Lemaitre -Walker Cosmological model of the Universe (Ho, 2020) and heat diffusion. They are useful in understanding the behaviour of matter in curved geometry thus informing their choice in this thesis.

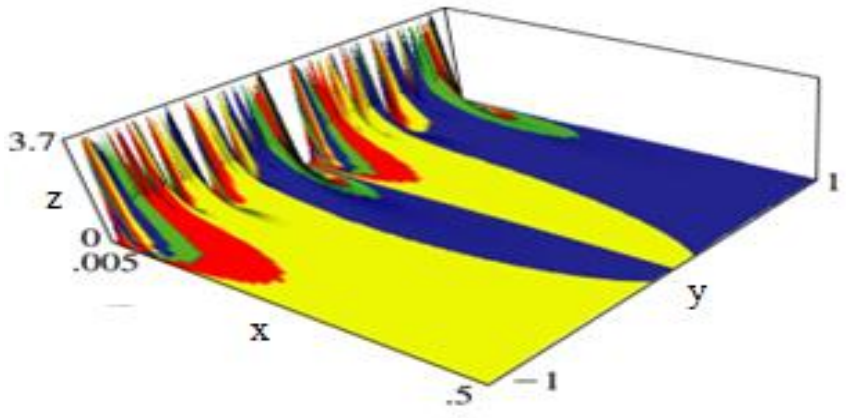

Figure 2. 13: Shows Jacobi elliptic theta functions
(Wolfram. matworld)

It is evident from the foregoing discussions that the subject of variation of neutron flux, leakage rates and reactivity against spheroids axis ratio is yet to be addressed, yet such knowledge is critical in the design of robust, efficient and safe reactors.

CHAPTER THREE

METHODOLOGY

3.1 Introduction

In this section concepts that were useful in the understanding of diffusion equation, neutron leakage rates and reactor core reactivity are presented. Thereafter, the concepts were applied in the development of the required formulae necessary for understanding the subject matter.

3.1.1 Spheroids

A spheroid is a quadric figure obtained by revolving an ellipse about the minor and major axis (Patra et al., 2018). A prolate is obtained by revolving the ellipse about the major axis while an oblate is obtained by revolving an ellipse about the minor axis. The semi major axis was indicated as (2a) while the semi minor axis was indicated as (2b) as illustrated in figure 3.1.

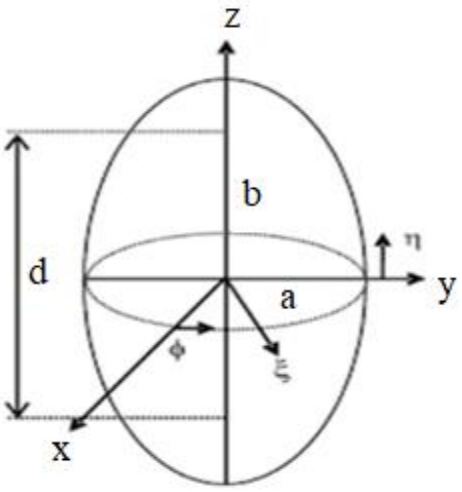

Figure 3.1: Figure Showing (a) Oblate and (b) Prolate spheroids

The coordinates of a spheroid are denoted using the symbols ξ,η and ϕ.The relations shown in equation 3.00(a) – 3.02 (d) can be used to transform Cartesian coordinate system to spheroid coordinate system

$$x = {}^{d}\!/_{2}\sqrt{(1-\eta^2)}(1+\xi^2)\cos\phi \qquad 3.00(a)$$

$$y = {}^{d}\!/_{2}\sqrt{(1-\eta^2)}(1+\xi^2)\sin\phi \qquad 3.01(b)$$

$$z = {}^{d}\!/_{2}\eta\xi \qquad 3.02(c)$$

Where $\eta \in [0,1], \xi \in (-\infty,\infty)$, $\phi \in (0,2\pi)$ 3.02(d)

(Where, $\boldsymbol{\eta}$, Angular variable of the spheroid coordinate, $\boldsymbol{x}$, radial variable of the spheroid coordinate and $\boldsymbol{\emptyset}$, azimuthal coordinate of the spheroid coordinate system)

Axis Ratio of Spheroids

If the major axis of a spheroid is, $2a$ and that of minor axis to be, $2b$. Then the ratio between the semi-minor axes to the semi major axis defined as the axis ratio of the spheroid is given by;

$$\frac{2b}{2a} = \frac{b}{a} \qquad 3.03$$

The surface of the spheroid, ξ_0 is associated with term, ξ through the relation,

$$\xi = \xi_0 \qquad 3.04$$

Such that,

$$\xi_0 = Tanh^{-1}({}^{b}\!/_{a}) \qquad 3.05$$

The oblate spheroid becomes flat circular disk as $\xi_0 \to 0$ and becomes spherical when $\xi_0 \to \infty$

3.1.2 Fick's Law of Diffusion

Fick's law postulates that the flux diffuses from regions of high concentration to regions of low concentration, with a magnitude that is proportional to the concentration gradient (Lamarsh & Baratta, 2001). Fick's law makes several assumptions that include; that there is no fission source in the system, the media for diffusion is uniform medium, Neutron density does is time independent among others.

Fick's law has several limitations that include; - First, the law is valid near the edges of medium the term in the exponential makes a significant impact to the integral points near the free paths. The assumption that contribution to the flux occurs only due to scattering is not sufficient since sources can also be present. The flux that was assumed to be varying slowly in an anisotropic media is limited by the fact that it rapidly changes in a strongly absorbing media. Other assumptions that were made include the fact that flux is independent of time and that a uniform media was being used.

The use of this law in reactor theory leads to the diffusion approximation. This is because most of the assumptions don't hold in a practical reactor.

3.1.3 Neutron Diffusion Equation

In order to understand the diffusion equation, the Figure 3.2 was considered and proceed to obtain the that is used to obtain the flux and the geometric buckling of the reactor,

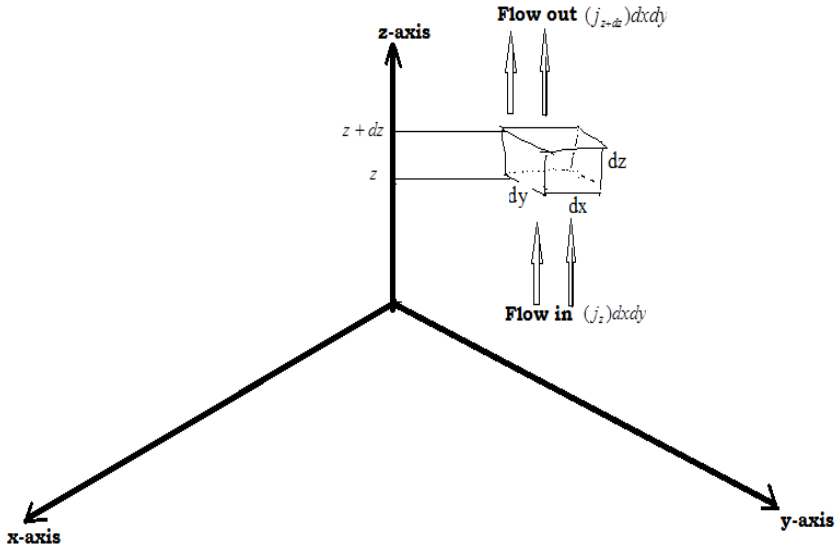

Figure 3.2: Typical Neutron diffusion flux inside a nuclear reactor core

To start with an isolation of an infinitesimal small cube of volume element, dv, is made and given by:

$$dv = dxdydz \qquad 3.06$$

In each of the surfaces of the cube, a net neutron current, j exists. It is assumed that only one surface perpendicular to the z-axis and that neutrons don't disappear (Beta decay). The difference between the neutrons current densities is discussed at length in (Murray & Holbert, 2014) and given as eqn 3.07:

$$j_{z+dz} - j_z = (\frac{dj}{dz})_z dz \qquad 3.07$$

Based on Fick's' law of diffusion, the neutron current density is given by;

$$j = -D\nabla\varphi \qquad 3.08$$

Where $D_x = D_y = D_z = D$ is the neutron diffusion coefficient for an isotropic system (Therefore, D is constant), and φ is the neutron flux.

Combining the eqns (3.06), (3.07) and (3.08) we obtain,

$$j = -{}^{d}/_{dz}\left(D\,\frac{d\varphi}{dz}\right)dxdydz \qquad 3.09$$

The total leakage rate per unit volume,L_v, is given by;

$$L_v = -D\left[\left(\frac{d^2\varphi}{dx^2}\right) + \left(\frac{d^2\varphi}{dy^2}\right) + \left(\frac{d^2\varphi}{dz^2}\right)\right] \qquad 3.10$$

Therefore,

$$-D\left[\left(\frac{d^2\varphi}{dx^2}\right) + \left(\frac{d^2\varphi}{dy^2}\right) + \left(\frac{d^2\varphi}{dz^2}\right)\right] = -D\nabla^2\varphi \qquad 3.11$$

We now move to consider a nuclear reactor core. From the previous discussions [1, 4 and 6], it was noted that neutrons supply to the reactor, (X)**,** is at a rate given by the sum of neutrons leakage rate (L_v) and neutron absorption rate (A_R). At a steady state condition, the neutrons change rate, N_c, the equation of neutron balance will be given by

$$X = L_v + A_R \qquad 3.12$$

The equation for neutron absorption rate is given by,

$$A_R = \sum_a \varphi \qquad 3.13$$

Therefore, neutron diffusion equation will be given by,

$$D\nabla^2\varphi - \sum_a \varphi + X = 0 \qquad 3.14$$

We can write the neutron supply rate to the reactor as,

$$X = v\sum_f \varphi \qquad 3.15$$

Σ_f is the fission cross section while v is the neutron fission fraction. Eq (3.15) becomes;

$$\nabla^2\varphi + {B_g}^2\varphi = 0 D\nabla^2\varphi - \sum_a \varphi + v\sum_f \varphi = 0 \qquad 3.16$$

Therefore, eq (3.16) finally reduces to,

$$\nabla^2\varphi + \frac{(v\sum_f - \Sigma_a)\varphi}{D} = 0 \qquad 3.17$$

3.1.4 Materials and Geometric Buckling

Geometric buckling is a relationship between the properties of the fissile material in a reactor core and the dimensions and configuration of the core (Ragheb, 2006). The geometric buckling factor term, is given by,

$$B_g{}^2 = \frac{(v\sum_f - \sum a)}{D} \qquad 3.18$$

and eq (3.18) can be written as,

$$\nabla^2\varphi + B_g{}^2\varphi = 0 \qquad 3.19$$

Equation (3.19) is the desired neutron diffusion equation at steady state conditions.

For a critical reactor, the materials B_m and geometric buckling found to be equal i.e;

$$B_g = B_m \qquad 3.20$$

Geometrical buckling is the lowest eigen-value of the equation 3.19.

3.1.5 Neutrons in a Nuclear Reactor

It is well understood that neutrons are a form of subatomic particles with no electrical charge to provide the attractive nuclear force sufficient to offset the electrostatic repulsive forces and hold atoms together. All atoms found in nature, except the basic hydrogen atom, have one or more neutrons in their nuclei in a nuclear reactor. There are two categories of neutrons. First there are prompt neutrons which are those accompanying the two nuclear fragments, e.g. the **2n** neutrons in the reaction;

$$^{235}\text{U} + {}^{1}_{0}n \longrightarrow {}^{93}\text{Rb} + {}^{141}\text{Cs} + 2\text{n}$$

In the case of ^{233}U, there are on the average 2.42 prompt neutrons for every successful bombardment with a neutron. Secondly, there are delayed neutrons which are associated with the beta decay of the fission products. In some cases, the available energy in the beta decay is high enough for leaving the residual nucleus in such a highly-excited state that neutron emission instead of gamma emission occurs (beta delayed neutron emission). Delayed neutrons have delays of order of seconds and are essential for the control of nuclear reactors (Al Zain et al., 2018)

3.1.5.1 Neutron flux

This refers to the product of neutrons density and neutrons velocity (Van Dam et al., 2005). For neutrons traveling in a certain direction only, the term neutron current may be applied; the total neutron flux is mathematically defined by

$$\varphi(E) = \int_0^\infty \varphi(E_i)\mathrm{dE}_i \qquad 3.21$$

Where the term is the flux of neutrons with energies between E_i and $E_i + dE_i$. The S.I unit for neutron flux is nm-2s-1.

3.1.5.2 Neutron interaction with matter

Whenever neutrons interact with materials atoms, different scenarios may arise (Plompen et al., 2020) which include; Elastic scattering whereby the kinetic energy and momentum of the neutrons is conserved. The second scenario is inelastic scattering whereby the kinetic energy of the neutron nuclide is conserved while momentum is not. Thirdly transmutation may occur whereby formation of a new nuclide occurs. Such nuclides are isotopes of the original nuclides. Examples

of reactions of transmutation include; Alpha decay (n, α), proton decay (n, p), Beta decay (n, β^+) and nuclear fission (n, f) .Different materials exhibit neotrun cross sections as shown in Figure 3.3.

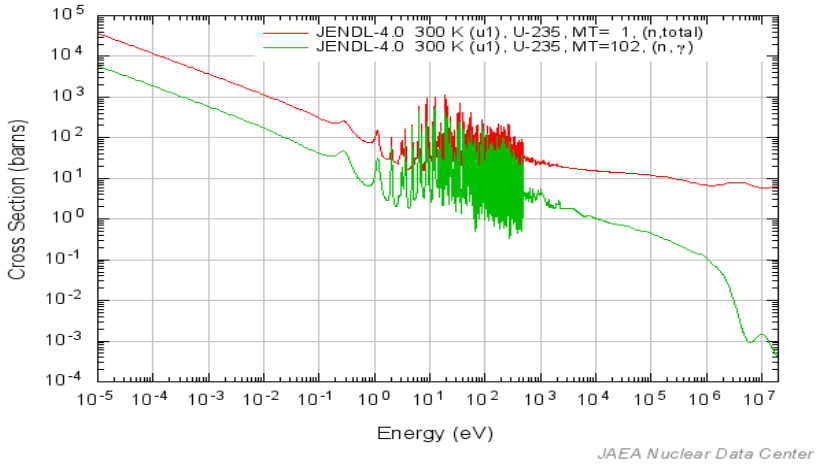

Figure 3.3: Showing Neutron cross sections at various energies for Uranium 235

(Source: JAEA Nuclear Data Center)

3.1.5.3. Thermal lifetime of Neutrons

It refers to the time neutrons exist in a critical reactor as thermals. It can be expressed as,

$$l_t = \frac{Number\ of\ thermals\ present}{Rate of\ supply\ of\ thermals} \qquad 3.22$$

3.1.5.4 Average Neutrons per fission

The average number of neutrons produced per neutron absorbed in a nuclear fuel is denoted by η_n. For a single fissile isotope, the value is given by,

$$\eta_n = \frac{v\sigma_f}{\sigma_a} \qquad 3.23$$

Where, σ_f-Fission Cross section, σ_a-Absorption cross section, v-Total neutrons produced per fission.

3.1.5.5 Neutron multiplication factor (k)

This is the ratio of the number of neutrons produced in one generation produced in the preceding generation i.e.

$$k_{eff} = \frac{\text{No.of neutrons produced in one generation}}{\text{No.of neutrons produced in preceeding generation}} \quad 3.24$$

The ratio of k denotes the criticality of the reactor.

$k_{eff} < 1$, Subcritical; $k_{eff} = 1$, Critical and $k_{eff} > 1$, Supercritical

3.1.5.6 Neutron Thermal Utilization Factor (f)

This is the ratio between total fission neutrons from thermal together with fission and fission neutrons from thermal neutrons only i.e.

$$f = \frac{Thermal\ Neutrons\ absorbed\ by\ fuel}{Total\ Thermal\ neutrons\ absorbed}$$

$$f = \frac{\sum_a^{Fuel}}{\sum_a^{Total}} \quad 3.25$$

3.1.5.7 Resonance Escape Probability (P)

It is the ratio of number of neutrons slowing to thermal and the total number of fast neutrons available for slowing i.e.

$$P = \frac{Number\ of\ neutrons\ slowing\ to\ thermal\ energy}{Total\ number\ of\ fast\ neutrons\ available\ for\ slowing}$$

$$P = \frac{N_{thermal}}{N_{Fast}} \quad 3.26$$

3.1.5.8 Neutrons Fast Fission factor (ε)

It is the ratio between thermal neutrons absorbed by the fuel and the total thermal neutrons absorbed i.e

$$\varepsilon = \frac{Total\ fission\ neutrons\ from\ thermal\ and\ fast\ fission}{Fission\ neutrons\ from\ thermal\ fission} \qquad 3.27$$

Table 3.1: Categories of Neutron based on their energies

	Neutron Category	Energies
1	Fast Neutrons	>20 Mev
2	Slow Neutrons	1-10eV
3	Thermal Neutrons	0.025eV
4	Cold Neutrons	0.000-0.02eV

Neutrons have been categorized into various classes defined by their energies as shown in table 3.1. Apart from this, there exist other categories of neutrons such as cadmium, resonance, intermediate and ultrafast neutrons. Thermal neutrons are responsible for causing chain reaction since they energies are in the range of fission cross section of nuclear fuels such as uranium.

3.1.6 Chain reaction

When a heavy nucleus is bombarded with a neutron, it yields several daughter nuclei in a reaction that is accompanied by energy release and radiation emission. This process is referred to as Chain reaction. Consider Figure 3.4 depicting the splitting of a Uranium nucleus into smaller daughter nuclei.

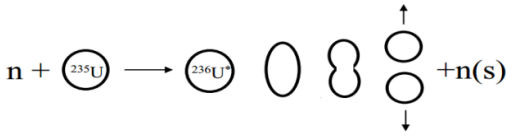

Figure 3. 4: Fission Uranium (U-235) nuclei with a neutron resulting in the formation of two lighter daughter nuclei and neutrons
(Cohen et al., 2018).

The actual process of splitting a heavy nucleus involves an incident neutron bombarding the nucleus resulting in the production of fission products, neutrons, energy and radiations. The process can be self-sustaining through chain reaction.

3.2 Formulation of the Diffusion Equation for Spheroid Geometry Problem

The time dependent neutron diffusion, famously known as the Fick's law of diffusion is given by the following equation;

$$(\tfrac{1}{v}\delta/_{\delta t} - (v\sum_f - \sum_a) - D\nabla^2)\psi(\xi,\eta,\varphi,t) = S(\xi,\eta,\varphi,t) \quad 3.28$$

Where the wave and the source terms in spheroid geometry are denoted by 3.28(a) and 3.28(b) respectively;

$$\psi(\xi,\eta,\varphi,t) \quad 3.29$$

$$S(\xi,\eta,\varphi,t) \quad 3.30$$

The source term 3.29 and 3.30 is further defined as;

$$S(\xi,\eta,\varphi,t) = \frac{1}{2\pi}S_R(\xi,\eta)\delta(t) \quad 3.31$$

While the diffusion equation is defined by

$$\psi(\xi,\eta,\varphi,t) = \psi_1(\xi,\eta,\varphi)\psi_2(t) \quad 3.32$$

Further, we can rewrite the second term of 3.32 as;

$$\psi_1(\xi,\eta,\varphi) = \psi_{1\xi}(\xi)\psi_{1\eta}(\eta)\psi_{1\varphi}(\varphi) \quad 3.33$$

If we further assume that there are no external sources of neutrons, then, from 3.30(b)

$$S(\xi,\eta,\varphi,t) = 0 \quad 3.34$$

So, that equation 3.28 reduces to;

$$(\frac{1}{v}\delta/_{\delta t} - (v\sum_f - \sum_a) - D\nabla^2)\psi(\xi,\eta,\varphi,t) = 0 \quad 3.35$$

Which upon rearranging we obtain;

$$\frac{1}{v}\delta/_{\delta t}\,\psi(\xi,\eta,\varphi,t) = (v\sum_f - \sum_a)\psi(\xi,\eta,\varphi,t) + D\nabla^2)\psi(\xi,\eta,\varphi,t) \quad 3.36$$

By separating equation 3.36 using the method of separation of variables, we get four main solutions

3.2.1 Solution for Time (t)

Using equation 3.32 and 3.35 we derive the following equation

$$\frac{1}{vD\psi_t}\partial/_{\partial t}\,\psi_t(t) + \lambda_{m\varepsilon} = 0 \quad 3.37$$

The solution for t is therefore given by;

$$\psi_t(t) = e^{-(\lambda_{m\varepsilon} vD)t} \quad 3.38$$

Where: $\lambda_{m\varepsilon}$- Is the time separation constant

3.2.2 Solution for the Quasi Radial Function (QRF), $\boldsymbol{\psi_{1\xi}(\xi)}$

In order to solve for the remaining variables, we rewrite the second term in equation 3.32 without the time variable as follows;

$$\psi_1(\xi,\eta,\varphi) = \psi_{1\xi}(\xi)\psi_{1\eta}(\eta)\psi_{1\varphi}(\varphi) \quad 3.39$$

Using 3.11, equation 3.08 can now be rewritten

as;

$$\partial/_{\partial\xi}\,(1+\xi)\,\partial/_{\partial\xi} + \partial/_{\partial\eta} - (\frac{1}{1+\xi^2} - \frac{1}{1-\eta^2})\,\partial^2/_{\partial\varphi^2} + \sigma^2(\eta^2+\xi^2)\psi_1(\xi,\eta,\varphi) = 0 \quad 3.40$$

We now proceed and solve for the three spatial functions in equation 3.39 using 3.35.

We get three pairs of equations as follows;

$$(\partial/\partial\xi\,(1+\xi)\,\partial/\partial\xi + \frac{m^2}{1+\xi^2} + \sigma^2\xi^2 - \lambda_{m\alpha}^2)\psi_{1\xi}(\xi) = 0 \qquad 3.41$$

$$(\partial/\partial\eta\,(1-\eta^2)\,\partial/\partial\eta + \frac{m^2}{1-\eta^2} + \sigma^2\eta^2 + \lambda_{m\alpha}^2)\psi_{1\eta}(\eta) = 0 \qquad 3.42$$

$$\frac{\partial\psi_{1\varphi}}{\partial\varphi^2} + im\psi_{1\varphi}(\varphi) = 0 \qquad 3.43$$

We start with the quasi radial function using the method adopted in (Alassar, 1999) by solving 3.43. The result is given by;

$$\psi_{1\xi}(\xi) = e^{i\sigma\xi}\frac{(1-i\xi)^{\alpha+m/2}}{(1+i\xi)^{\alpha+m/2+1}}R_{m\alpha}^{(p)}(\xi) \qquad 3.44a$$

Since practically neutrons flux is a decreasing with increasing values of ξ, we let The second term of 3.44 takes different values depending on the value of 'p' as indicated below;

$$R_{m\alpha}^{(0)}(\xi) = 0 \qquad 3.45(a)$$

$$R_{m\alpha}^{(1)}(\xi) = \frac{(\alpha+1)(\alpha+m+1)}{2(1+i\xi)} - \frac{\alpha(\alpha+m)}{2(1-i\xi)} \qquad 3.46(b)$$

The values of 'p' = 2 through 'p' = 4 are defined in Zeppenfeld M(2009)

3.2.3 Solution for Quasi Angular Function (QAF) using Rodriguez formula

Using the method discussed in Shqair et al. (2019), we proceed to solve for 3.44 and obtain;

$$\psi_{1\eta} = (1-\eta^2)^{\frac{m}{2}}e^{-\sigma(1-\eta)}A_{m\alpha}(\eta) \qquad 3.47$$

The equation of $A_{m\alpha}$can be written as;

$$A_{m\eta}(\eta) = L_\alpha^{(m)}(2\sigma(1-\eta)) + \vartheta(\frac{1}{\sigma}) \qquad 3.48$$

We also make an assumption that;

$$\vartheta(\frac{1}{\sigma}) \approx 1 - \eta^2 \qquad 3.49$$

We then solve the first term of 3.48 using Rodrigues

Such that

$$L_{\alpha}^{(m)} = \sum_{m=0}^{n}(-1)^m \frac{(\alpha+m)}{(n-m)!(\alpha+m)!m!}(2\sigma(1-\eta))^m \qquad 3.50$$

The quasi-angular solution now becomes

$$\psi_{1\eta}(\eta) = (1-\eta^2)^{m/2} e^{-\sigma(1-\eta)} \sum_{m=0}^{n}(-1)^m \frac{(\alpha+k)!}{(n-m)!(\alpha+m)!m!}(2\sigma(1-\eta))^m + (1-\eta^2)$$

..... 3.51

3.2.4 Solution for, $\boldsymbol{\psi_{1\varphi}(\varphi)}$

The solution for $\psi_{1\varphi}(\varphi)$ can be obtain by solving 3.43. The following differential equation is found

$$\frac{\partial^2}{\partial\varphi^2}\psi_{\varphi}(\varphi) + im\psi_{\varphi}(\varphi) = 0 \qquad 3.52$$

Using a method similar to the one discussed in Shqair et al. (2019) we obtain,

$$\psi_{\varphi}(\varphi) = e^{-im\varphi} \qquad 3.53$$

3.2.5 Resulting diffusion equation

The resulting diffusion equation for the diffusion equation is,

$$\psi(\xi,\eta,\varphi,t) = \sum_{m=0}^{\infty}\sum_{\varsigma=0}^{\infty} e^{-(\sigma+\lambda_m \upsilon D t-\eta\sigma)+i(m\varphi-\sigma\xi)}\{(\frac{(1-i\xi)^{\varsigma+m/2}}{(1+i\xi)^{\varsigma+m/2+1}}(1-$$

$$\eta^2)^{m/2} A_{m\alpha}(\eta) R_{m\alpha}^{(p)}(\xi)\} \qquad 3.54$$

We now make the following relationships to equation 3.54

- $g_1 = (\eta\sigma - \sigma - \lambda_m \upsilon D t)$ and $g_2 = (m\varphi - \sigma\xi)$
- $G_1(\eta) = \sum_{m=0}^{\infty}((1-\eta^2)^{m/2} A_{m\alpha}(\eta))$

$$G_2(\xi) = \sum_{m=0}^{\infty}\sum_{\varsigma=0}^{\infty} \left(\frac{(1-i\xi)^{\varsigma+m/2}}{(1+i\xi)^{\varsigma+m/2+1}} R_{m\alpha}^{(p)}(\xi)\right.$$

We then make substitutions for the equations in 3.54 such that;

$$\psi(g_1,g_2) = G_1(\eta)G_2(\xi)e^{g_1+g_2 i} \qquad 3.55$$

Finally,

$$\psi(g_1,g_2) = G(g_1,g_2)e^{g_1+g_2 i} \qquad 3.56$$

Equation 3.56 is the desired equation for neutron diffusion problem under investigation.

We recall the relation in equation (3.05);

$$\xi_0 = Tanh^{-1}(b/a)$$

Where the ratio (b/a) is the axis ratio of the spheroid,

Therefore, it can be seen that for small values of,φ, the axis ratio of the spheroid is proportional to the value of g_2 i. e

$$g_2 \propto b/a. \qquad 3.57$$

The coefficient of the term $G(\eta,\xi)$ for values of $-1 \leq \eta,\xi \leq 1$ can be generalized to take the values

$$G(\eta,\xi) = a + bi. \qquad 3.58$$

a, b are random integer values.

3.2.6 Relationships with Jacobi elliptic Theta functions

We consider the equation (3.56),

$$\psi(g_1,g_2) = G(g_1,g_2)e^{g_1(\tau)+g_2(\xi)i}$$

We start by converting g_1 into a function of time andg_2 quasi angular component i.e

$$\psi(g_1(\tau), g_2(\xi)) = G(g_{1,}g_2)e^{g_1(\tau)+g_2(\xi)i} \quad 3.59$$

- We then make the assumption that,

$g_1 \approx -\lambda_m vDt$

Also, we make g_1 periodic function of time so that;-

$2\pi in = -\lambda_m vD$

$g_1 \approx -2\pi int$

- We further introduce a timeless component(τ) related to time as follows;-

$t \approx n\tau$ and as such, g_1 becomes,

$g_1 \approx -2\pi in^2\tau$

- For g2, we proceed as follows;-

$g_2 = (m\varphi - \sigma\xi)$

- If we introduce the condition that, τ⋙⋙σ and ξ⋙⋙φ , then it follows that;-

$g_2 \approx -\sigma\xi$

Again, we know that g_2 takes numerous eigen values in the spheroid coordinate systems. Thus, we let σ take some arbitrary even values of 'n', we introduce the relations

$\sigma \approx -2n$. Hence, $g_2 \approx -2n\xi$

Substituting for 3.60 and 3.61 in equation 3.59 we obtain the following relationship,

$$\psi(\tau,\xi) = G(g_{1,}g_2)\sum_{-\infty}^{\infty} e^{-i\pi n^2\tau}e^{-2in\xi} \quad 3.62$$

We then make an assumption that;

$$A_i = G(g_1, g_2) \quad 3.63$$

Then equation 3.62 becomes,

$$\psi(\tau,\xi) = A_i\sum_{-\infty}^{\infty} e^{-i\pi n^2\tau}e^{-2in\xi} \quad 3.64$$

Equation 3.64 is indeed a Jacobi elliptic theta function of the third kind and can be written as;

$$\psi(\tau,\xi) = A_i\sum_{-\infty}^{\infty} e^{-i\pi n^2\tau}e^{-2in\xi} \quad 3.65$$

Further we introduce the following relationship

$$\tau_q = e^{-i\pi\tau} \quad 3.66$$

Using the substitution of equation 3.66, the desired Jacobi elliptic theta function was found to be;

$$\psi(\xi,\tau_q) = A_i\sum_{n=0}^{\infty} \tau_q^{n^2}e^{-2in\xi} \quad 3.67$$

In the study of heat conduction in spheroids by Alassar et al. (2014), similar findings were established.

3.2.7 Axis Ratio-Neutron leakage for prolate spheroid

The separation of variables technique was applied in Yip et al. (2002) to yield a relation between axis ratio and geometric buckling (B_g) for prolate (eqn 3.68) and oblate spheroid (eqn 3.69) respectively;

$$B_g^2 M_2^2 = \frac{\pi^2}{3}\{\frac{2c^2+1}{c^2}\} \quad 3.68$$

$$B_g^2 M_2^2 = \frac{\pi^2}{3}\{\frac{c^2+2}{c^2}\} \quad 3.69$$

The geometric buckling for prolate and oblate spheroids is presented in 3.70 and 3.71 respectively.

$$B_g^2 = \frac{\pi^2}{3}\{\frac{2c^2+1}{c^2 M_2^2}\} \quad 3.70$$

For Oblate, the geometric buckling is given by,

$$B_g^2 = \frac{\pi^2}{3}\{\frac{c^2+2}{c^2 M_2^2}\} \quad 3.71$$

For a prolate spheroid, the neutron thermal life time is defined as ;-

$$l_t = \frac{l_0}{(1+B_g^2 L^2)} \quad 3.72$$

Or

$$l_t(1 + B_g^2 L^2) = l_0 \quad 3.73$$

Making B_g the subject of the formula, we obtain,

$$B_g^2 = \frac{l_0 - l_t}{L^2 l_t} \quad 3.74$$

Further, we let

$$T = \frac{l_0 - l_t}{l_t} \quad 3.75$$

Substituting eq (3.75) in eq (3.74) we obtain,

$$B_g^2 = \frac{T}{L^2} \tag{3.76}$$

From (Plans & Ground), the derivation of geometrical buckling for a prolate spheroid is defined according to equation;

$$c = \left[\frac{\pi^2}{3B_g^2M_2^2 - 2\pi^2}\right]^{1/2} \tag{3.77}$$

Inserting equation eq (3.76) into equation (3.77), we obtain;

$$c = \left[\frac{\pi^2}{3\frac{T}{L^2}M_2^2 - 2\pi^2}\right]^{1/2} \tag{3.78}$$

We also introduce the neutron thermal life time constant, k, given by,

$$k = 3M_2^2T \tag{3.79}$$

The thermal lifetime constant is not related to criticality of a reactor.

Therefore, eq (3.78) becomes,

$$c = \left[\frac{9.86L^2}{k - 19.72L^2}\right]^{1/2} \tag{3.80}$$

The Neutron leakage rate versus the axis ratio of the prolate spheroid is given as,

$$L = \left[\frac{kc^2}{9.86 + 19.72c^2}\right]^{1/2} \tag{3.81}$$

3.2.8 Axis Ratio-Neutron leakage rates for Oblate spheroid

The geometric buckling for oblate spheroid is defined according to (3.69); recalling equation (3.76), for geometric buckling

$$B_g^2 = \frac{T}{L^2}$$

The eq (3.69) can be rearranged as;

$$B_g^2M_2^2c^2 = \frac{\pi^2}{3}\{c^2 + 2\} \tag{3.82}$$

Finally, the relation in eqn (3.83) was obtained,

$$c = \left[\frac{19.72L^2}{k-9.86L^2}\right]^{1/2} \quad 3.83$$

The neutron leakage rate versus axis ratio of the oblate spheroid is given as;

$$L = \left[\frac{kc^2}{19.72+9.86c^2}\right]^{1/2} \quad 3.84$$

Where; Neutron thermal lifetime = l_t, Neutron thermal lifetime when there is no leakage = l_0, Neutron leakage rate = L, Semi-minor axis = M_2, Semi-major axis = $M_1$and Neutron and neutron thermal life time constant = k.

3.2.9 Reactivity of a reactor

The relationship between reactivity constant and the axis ratio of a spheroid reactor is being developed. Recalling equations 3.80 and 3.81 below showing the leakage relationships for Prolate and Oblate,

$$L = \left[\frac{kc^2}{9.86+19.72c^2}\right]^{1/2}$$

$$L = \left[\frac{kc^2}{19.72+9.86c^2}\right]^{1/2}$$

The relationship between the effective multiplication factor and leakage rates of a spheroids was discussed in (Sjoestrand, 1958) and presented as equation

$$K_{eff} = \frac{v^{\Sigma_f}/_{\Sigma_a}}{1+L^2B^2} \quad 3.85$$

Furthermore, the core reactivity (Walters et al., 2018) of a nuclear reactor was shown to be;

$$\rho = \frac{K_{eff}-1}{K_{eff}} \qquad 3.86$$

If we let $\Omega = \frac{v\Sigma_a}{\Sigma_f}$

If we combine (3.80), (3.85) and (3.86), we obtain for Oblate spheroid,

$$\rho = 1 - \frac{19.72+(9.86+kB^2)c^2}{(19.72+9.86c^2)\Omega} \qquad 3.87$$

And combining (3.84), (3.85) and (3.86) we obtain for prolate spheroid,

$$\rho = 1 - \frac{9.86+(19.72+kB^2)c^2}{(9.86+19.72c^2)\Omega} \qquad 3.88$$

Again, if we let, $\beta^2 = kB^2$. 3.89

We obtain equation (3.60) and (3.61) for reactivity coefficients for oblate and prolate spheroids

$$\rho = 1 - \frac{19.72+(9.86+\beta^2)c^2}{(19.72+9.86c^2)\Omega} \qquad 3.90$$

and

$$\rho = 1 - \frac{9.86+(19.72+\beta^2)c^2}{(9.86+19.72c^2)\Omega} \qquad 3.91$$

CHAPTER FOUR

RESULTS AND DISCUSSIONS

4.1 Introduction

In this section results obtained from the study are presented and discussed. The main results presented include; the behavior of time dependent neutron diffusion flux in a spheroid reactor core investigate using Jacobi elliptic theta functions in combination with analytical method; the relationship between the axis ratio and neutron leakage rates at axis ratios equal, smaller and larger than unity and finally the behavior of the of reactors core reactivity at various the axis ratios of the spheroid.

In the resolution of the results using Analytic method, the values for the coefficients in $G(\eta,\xi) = a + bi$ were set within the range of 0 to 100; the real part of the coefficient was represented by 'a' while the complex part was represented by 'b', and their interval varied. Secondly, the exponential part of the derived equation $\psi(g_1(\tau), g_2(\xi)) = G(g_{1,}g_2)e^{g_1(\tau)+g_2(\xi)i}$ was shown to possess two main variables. The first variable, (**g_1**) was mainly dependent on time (t) and referred to as Time Dependent Component (TDC) while the second variable, **(g_2)** was the Axis Ratio Dependent Component (ARDC) and was dominated by quasi angular component; (ξ) which was related to the axis ratio of the spheroid. The range of the two variables, were set arbitrarily between lower Boundary (-1) and upper Boundary (100) using an interval varied between $0.01 \leq i \leq 1$.

In the second part the diffusion problem was modified into a Jacobi elliptic theta function, $\psi(\xi,\tau_q) = A_i \sum_{n=0}^{\infty} \tau_q^{n^2} e^{-2in\xi}$. This equation had two parts; the (TDC) defined as (τ_q) and the quasi-angular dependent component (ξ) related to the (ARDC). The results obtained after imposing appropriate boundary conditions pre-

specified for each case. The coefficients; A_i , were varied from 0 to 100 units while the limits of TDC and ARDC were varied between, Lower Boundary (L) at 0 and the upper boundary (U) at 100. Similarly, the value of 'n' was 1 also increased from 0 to 100.

Similarly, the sets for limit in the results were defined as L (TDC 1, ARDC 1) and U (TDC 2, ARDC 2). 'a' and 'b' were used to compute the amplitude as defined by equation $G(\eta,\xi) = a + bi$.

As for the neutron leakage rate, the function; $L = \left[\frac{kc^2}{9.86+19.72c^2}\right]^{\frac{1}{2}}$ was adopted for prolate and $L = \left[\frac{kc^2}{19.72+9.86c^2}\right]^{\frac{1}{2}}$ adopted for oblate with the value of 'c' varied. In the determination of reactivity, the equation, $\rho = 1 - \frac{9.86+(19.72+\beta^2)c^2}{(9.86+19.72c^2)\Omega}$ was adopted for a oblate and$\rho = 1 - \frac{9.86+(19.72+\beta^2)c^2}{(9.86+19.72c^2)\Omega}$, for prolate spheroids with the value of **Ω** =5 and β (0.1, 0.5, 1, 2.5, 5) adopted in a selected range of ARDC values and intervals.

Lastly, Python software was used to generate and analyze the data. This software was selected because of its versatility and ease of computations.

4.2 Analysis of Neutron flux using Jacobi Elliptic Theta Functions

In this section, analysis of the resulting diffusion equation was carried out. This was accomplished by changing the value of 'n' to $0 \leq n \leq 1$ In addition; the other terms of equation were also varied through a set of conditions that were defined for every graph. They were subjected to values of 'n'=0.01, 0.1 and 0.5 which

1 TDC -Time Dependent Component, ARDC-Axis Ratio Dependent Component

were considered significant because they were observed to fairly represented the main set of results.

4.2.1 Diffusion surfaces for values of 'n' less than unity i.e. ('n'<1)

When the value of 'n' in equation $\psi(\xi,\tau_q) = A_i \sum_{n=0}^{\infty} \tau_q^{n^2} e^{-2in\xi}$ was set at 0.001, while the other conditions were set such that, the lower boundary, L (0,0), the upper boundary as, U (1,1), while the TDC and ARDC values both set at 0.01, a graph shown in Fig 4.01 was obtained.

Table 4. 1: Boundary conditions set 1

	Lower Boundary	Upper Boundary	Interval	'n'
TDC	0	1	0.01	0.001
ARDC	0	100	1	

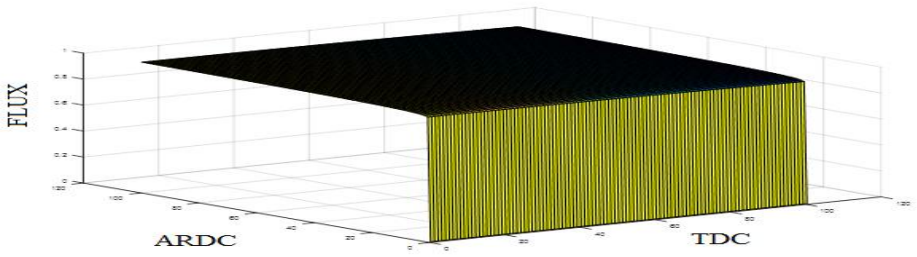

Figure 4. 1: Neutron Flux in Spheroid in a Typical Cubical Surface
(Plotted Using Conditions in Table 4.1)

Regarding the results obtained in the Figure 4.1, it can be deduced as a characteristic cubical ternary surface. Neutrons diffusion was nearly perpendicular; from vertical plane minimum flux (0) to maximum (1) almost instantaneously and then diffused through a horizontal plane as ARDC increased from 1 to 120 units. The flux indicated a cubical surface whereby at the core of

the spheroid; neutrons reached and remained constant at maximum flux even when ARDC and TDC were varied.

When plotted along the flux versus ARDC plane, with conditions set such that the lower boundary, L (0, 0), the upper boundary, U (1, 1), with the TDC and ARDC both set at 0.01, and the amplitude at A = 1 and equation 3.68 adopted.

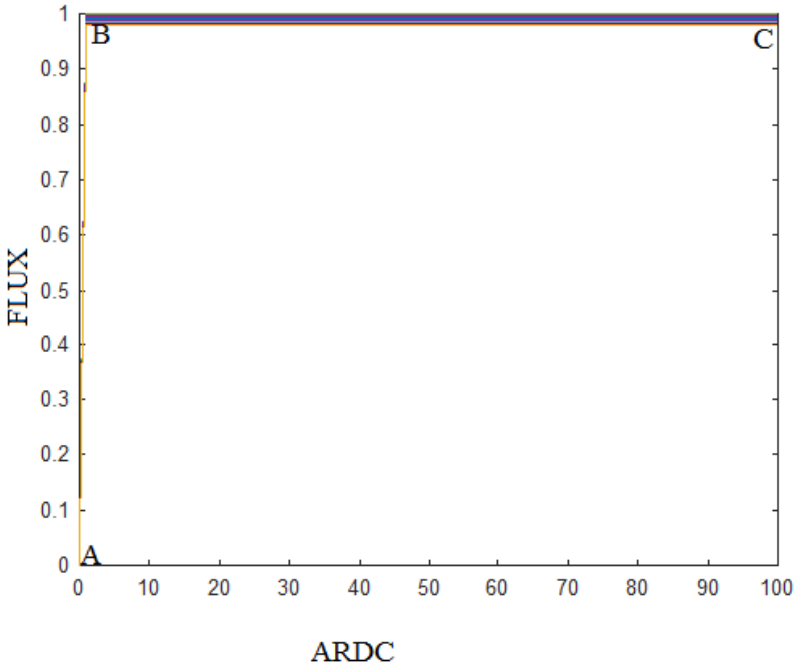

Figure 4. 2: Neutron Flux In 2-Dimensional Spheroid Geometry Using Jacobi Elliptic Theta Function

(Plotted using Conditions in Table 4.1).

It was observed that neutrons flux jumped from minimum (0) to maximum (1) in an infinitesimal change in ARDC (0-1) but remained fairly constant between ARDC (1-100). This depicted a pulsed behavior of neutrons occurring under the imposed conditions. It was also established that flux intensity was greater at the plateau stage of diffusion i.e. between ARDC (1-100) compared to the stage AB as shown in Figure 4.2.

In order to investigate the effects of the amplitude on flux, the value of 'n' in equation was set at 0.1, while the remaining conditions were altered such that at lower boundary, L (0,0) and the upper boundary as, U (1,1), and the TDC and ARDC both set at 0.01. In addition, the amplitude values where considered at A_i =1 and A_i = 5.

The results showed that as the amplitude of the wave increased, the maximum flux also increased proportionately. This was exemplified by the amplitude of 4.3 (i) that jumped to unity while the amplitude for Fig 4.3 (ii) had jumped to 5 units within a similar ARDC interval. Secondly, the angles between fluxes surfaces and the TDC/ARDC planes were observed to have slightly increased. This was a deviation from an almost perpendicular characteristic that was exhibited initially in figure 4.2. This particular result highlighted the fact that neutrons reached its maximum flux at relatively smaller values of 0 < ARDC < 0.1 and remained constant even as TDC and ARDC varied at relatively higher values.

Table 4. 2: Boundary Conditions Set 2

	Lower Boundary	Upper Boundary	Interval	'n'
TDC	0	1	0.1	0.1
ARDC	0	1	0.1	
Amplitude	1(Fig i), 5(Fig ii)			

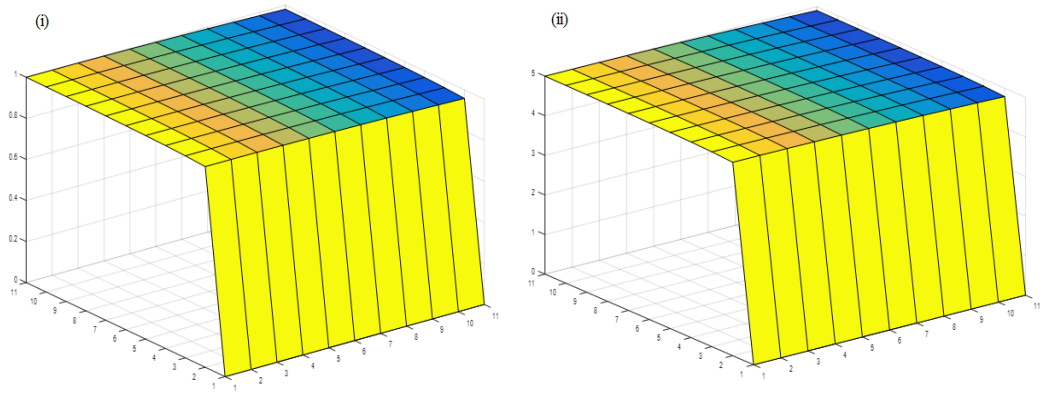

Figure 4. 3: Neutron Flux in Spheroid Using Jacobi Elliptic Theta Function Under

Upon re-configuring the imposed conditions such that, the lower boundary, L (0,0) and the upper boundary was set as, U (1,1) and both the TDC and ARDC set at 0.01 and A_i =100. Thereafter, the equation $\psi(\xi,\tau_q) = A_i \sum_{n=0}^{\infty} \tau_q^{n^2} e^{-2in\xi}$ was plotted in 2 - dimensions leading to the generation of Figure 4.4.

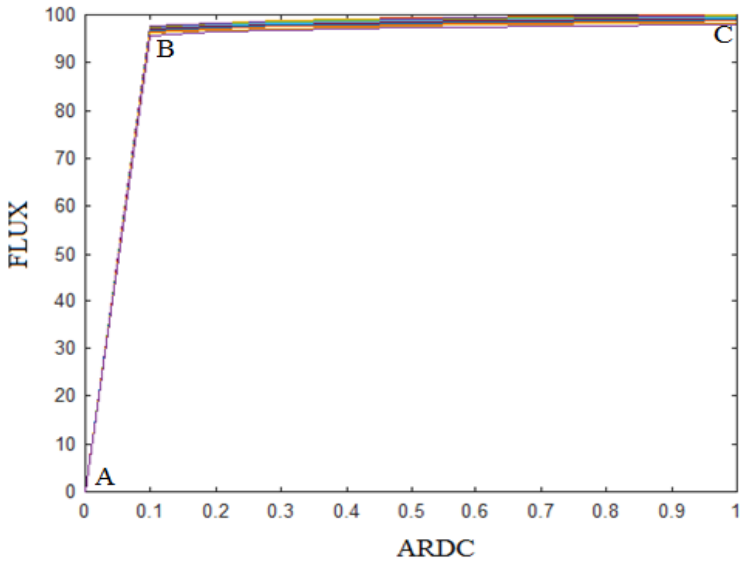

Figure 4. 4: A 2-dimensional neutron flux in spheroid using Jacobi elliptic theta function under

It became evident that an increased amplitude of the wave function resulted in a corresponding increase in angle **ABC** (Figure 4.4). The amplitude of plane **ABC**

in Figure 4.4 was found to be unity and that of Figure 4.01 was found to be 100. The increased amplitude was inferred to have increased the gradient of **ABC** of the graph 4.4.

In the second investigation, the value of 'n' was set at 'n'= 0.01. Thereafter, conditions imposed on the equation, $\psi(\xi,\tau_q) = A_i \sum_{n=0}^{\infty} \tau_q^{n^2} e^{-2in\xi}$,such that the lower boundary was L (0, 0), the upper boundary set as U (1,100), and the TDC interval as 0.01 and an interval of ARDC set at unity. The results are presented in Figure 4.03a.

Table 4. 3: Boundary Conditions set 3

Table 4.03: Conditions set 3.	Lower Boundary	Upper Boundary	Interval	'n'
TDC	0	1	0.01	0.01
ARDC	0	100	1	

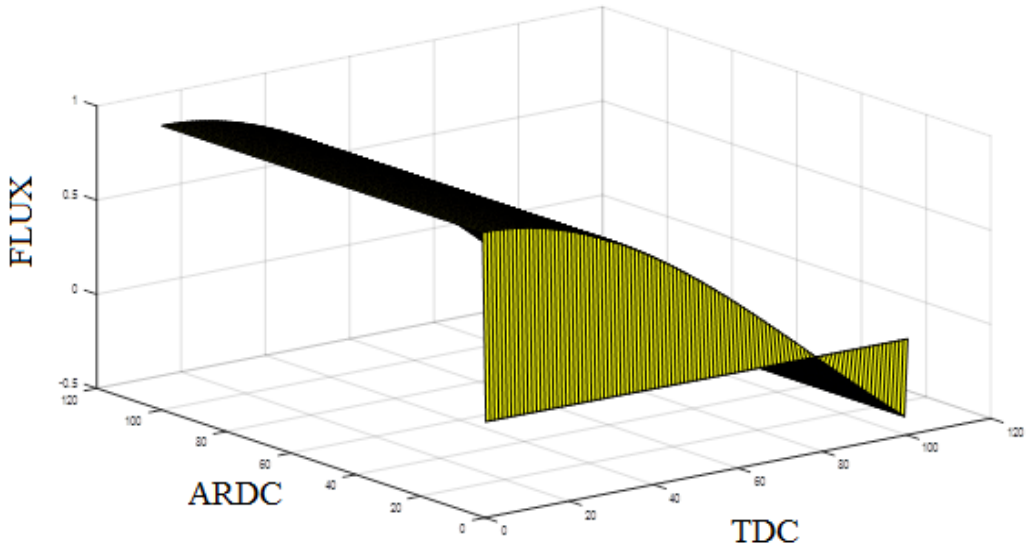

Figure 4. 5: Neutron Flux in Spheroid Using Jacobi Elliptic Theta Function
(Plotted using conditions in Table 4.3)

In this scenario, neutron flux increased from the initial flux (0) to maximum flux between TDC (0-80) and decreased from initial flux (0) to (-0.5) between TDC

(81-100). Secondly, diffusion of neutrons along the plane surface between ARDC and TDC characterized flux variation as a characteristic cylindrical surface. Therefore, from Figure 4.03a, it is shown that neutrons exhibited two surfaces of diffusion; first they diffused along the planes between TDC-Flux.

In two dimensions, conditions were imposed on equation $,\psi(\xi,\tau_q) = A_i \sum_{n=0}^{\infty} \tau_q^{n^2} e^{-2in\xi}$, such that the lower boundary was L (0, 0), the upper boundary set as U (1,100), and the TDC interval set as 0.01 while the interval of ARDC was set at 1. In addition, the value of 'n' was maintained at 'n'= 0.01. The result was as shown in Figure 4.6 where it was evident that flux became nearly uniform as ARDC increased between 1-100 with greater intensity of flux observed at maximum flux (1). Secondly, flux from the source, between ARDC (0-1), was largely non-uniform but spread to different flux values ranging between (0.3 > Φ <1). The flux was also observed to be asymmetrical along the flux line zero.

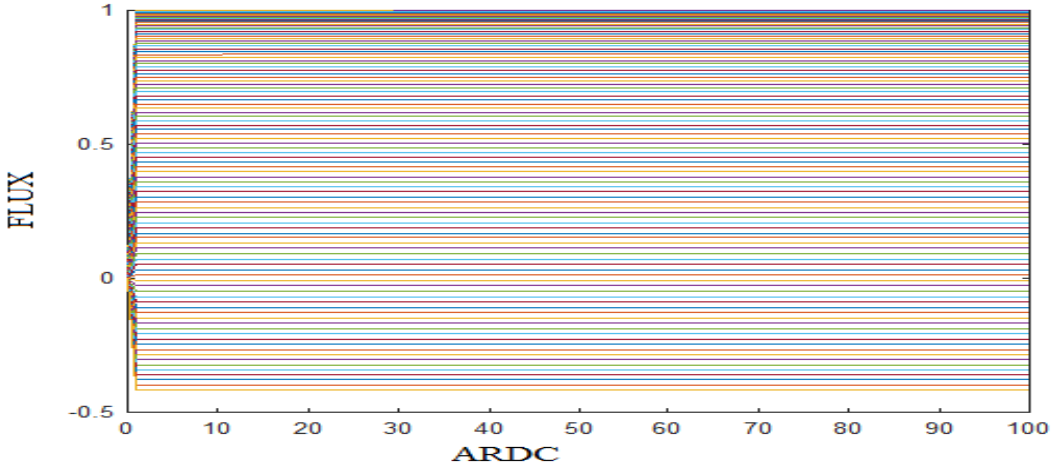

Figure 4. 6: A 2-Dimensional Neutron Flux in Spheroid Using Jacobi Elliptic Theta Function
(Plotted using Conditions in Table 4.03)

Another major finding in this section was the emergence of continuous 3-dimensional waves when the equation; $\psi(\xi,\tau_q) = A_i \sum_{n=0}^{\infty} \tau_q^{n^2} e^{-2in\xi}$ was plotted under conditions such that the lower boundary, L (0, 0) and the upper boundary U (1,100) the TDC and ARDC components set at 0.01 and 1 respectively. Furthermore, the value of 'n' was set at 'n'= 0.01, the Fig 4.7 was obtained.

Table 4. 4: Boundary Conditions set 4

	Lower Boundary	Upper Boundary	Interval	'n'
TDC	0	1	0.01	0.1
ARDC	0	100	1	

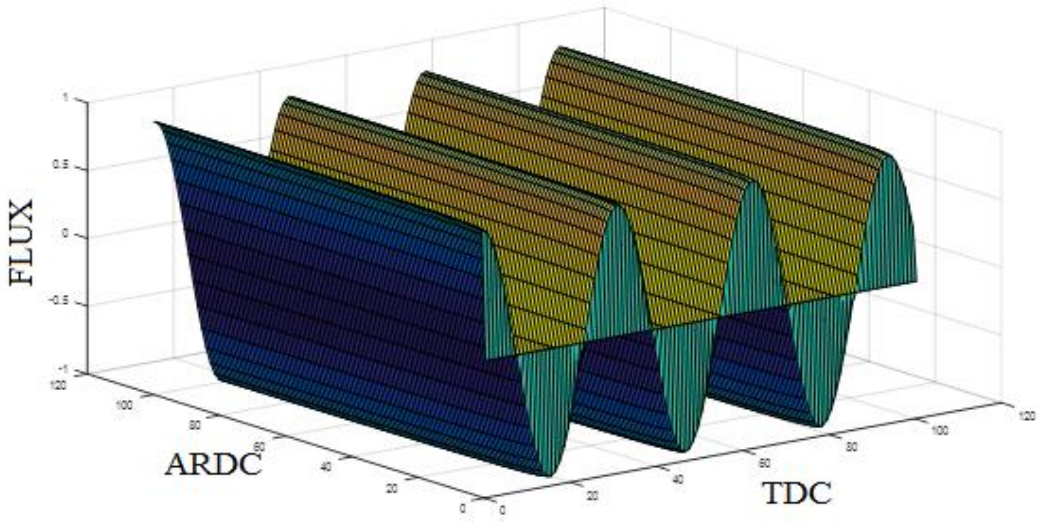

Figure 4. 7: A 3-Dimensional Continuous Cylindrical Surface at 'N'=0.1 Using Jacobi Elliptic Theta Function

(Plotted using conditions 4 in Table 4.04)

The results shown in Figure 4.7 explicitly portrayed a smooth continuous 3-dimensional wave with a period of 20, amplitude of 1 and a frequency of 3.5/20. When ARDC was increased from 0 to 120, the flux behavior of the wave also increased from an initial ARDC=0 to a maximum which was determined by the TDC. A case in point is that, at TDC =0, 40, 60 and 100 the flux reached its peak and conversely, the flux reached its minima when the TDC=20, 40, 60 and 100.

This type of diffusion surface was established to be a cylindrical topological surface (Ayyoubzadeh et al., 2012). This observation suggests that inside the spheroid, there existed flux configuration that conformed to a cylindrical surface (Walters et al., 2018).

When the value of 'n' was adjusted to 'n'=0.5, a new flux behavior was established as the equation $\psi(\xi,\tau_q) = A_i \sum_{n=0}^{\infty} \tau_q^{n^2} e^{-2in\xi}$, was adopted with lower boundary, L (0, 0), the upper boundary U (1,100) while the TDC and ARDC components set at 0.01 and 1, respectively and the results presented in Figure 4.8 was obtained.

Table 4. 5: Boundary conditions set 5

	Lower Boundary	Upper Boundary	Interval	'n'
TDC	0	1	0.01	0.5
ARDC	0	100	1	

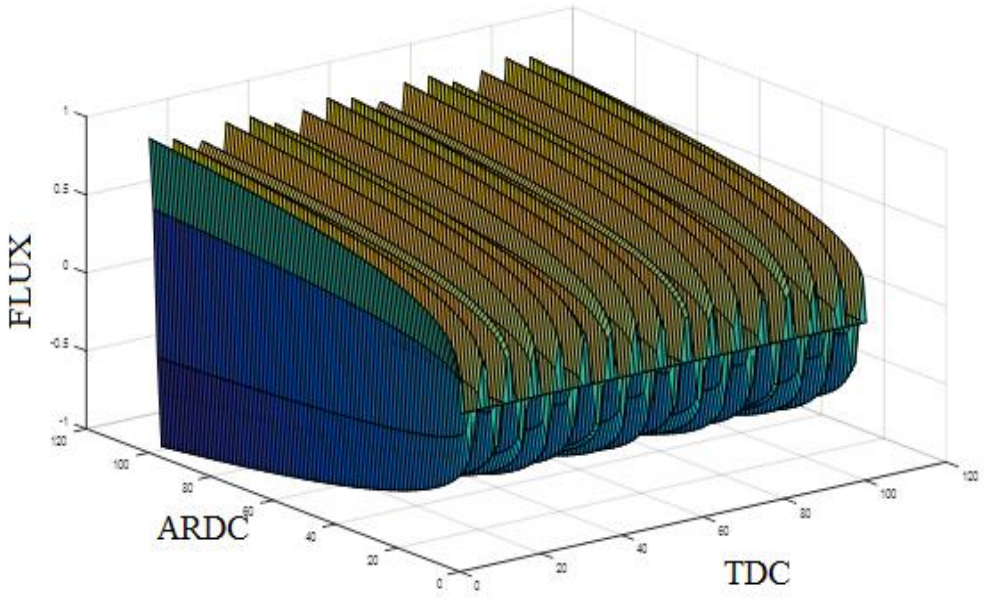

Figure 4.8: A 3-Dimensional Continuous Wave At 'N'=0.5 Using Jacobi Elliptic Theta Function

(Plotted using conditions in Table 4.05)

The Figure 4.8 espoused multiple waves generated as time progressed; several wavelets emerged as flux rose from 0 to 1 and as ARDC increased from 0 to 120

units. The figure displayed the shape of a spheroid when viewed along the ARDC/flux plane. Furthermore, it was inferred that the figure was indeed a continuous periodic 3-dimensional wave akin in some aspects to Figure 4.7. However; it was observed that while the Figure 4.7 projected fairly equal amplitude for nearly all the TDC values while Figure 4.08 had varying amplitudes for various TDC values.

In order to explore the various features of neutron flux in Fig 4.05a, it was plotted in two dimensions by adopting the equation , $\psi(\xi, \tau_q) = A_i \sum_{n=0}^{\infty} \tau_q^{n^2} e^{-2in\xi}$,under boundary conditions such that the lower boundary was L (0, 0), the upper boundary U (1,100), the TDC and ARDC components set at 0.01 and 1 and the value of 'n' was adjusted such that 'n'= 0.5.

As per these boundary conditions the results were as presented in Figure 4.05**b**. It was elucidated that neutrons originated from the source and diffused outwards while taking the shape of the spheroid; a case of an oblate spheroid as can be seen in figure 4.9 (ii), demonstrated that flux behaved inside the spheroid nuclear reactor core from their source at point '**E1'** as they diffused to the other end '**E2'** of the spheroid perfectly fitted the shape of the core. The second observation made was that the neutron flux lines progressed as wave packets.

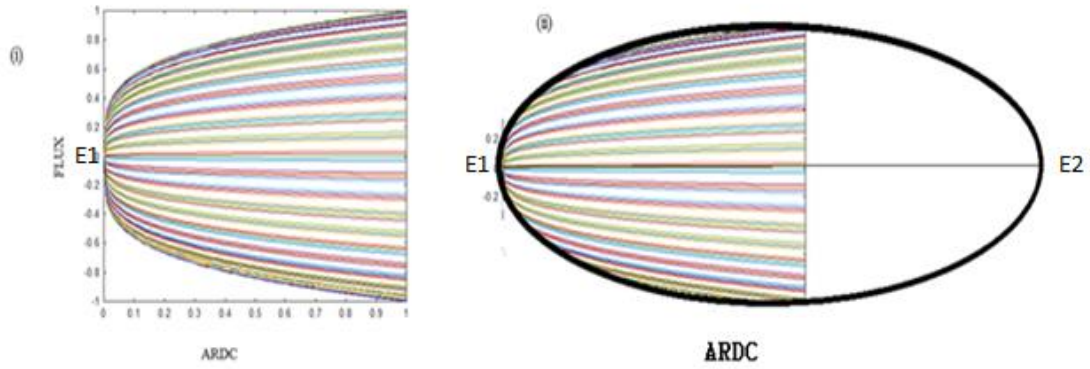

Figure 4. 9: 2-Dimesional Continuous Wave At 'N'=0.5 Using Jacobi Elliptic Theta Function

4.2.2. Diffusion surfaces for Values of 'n' equal to 1, i.e. ('n'=1)

The equation $,\psi(\xi,\tau_q) = A_i \sum_{n=0}^{\infty} \tau_q^{n^2} e^{-2in\xi},$ was plotted in 3-dimensions with conditions imposed such that the lower boundary was, L (0, 0) and the upper boundary, U (1, 1). The TDC had an interval of 0.1 while ARDC had a similar time interval of 0.1. The result was the formation of Fig 4.7.

Table 4. 6: Boundary conditions set 6

	Lower Boundary	Upper Boundary	Interval	'n'
TDC	0	1	0.1	1
ARDC	0	1	0.1	

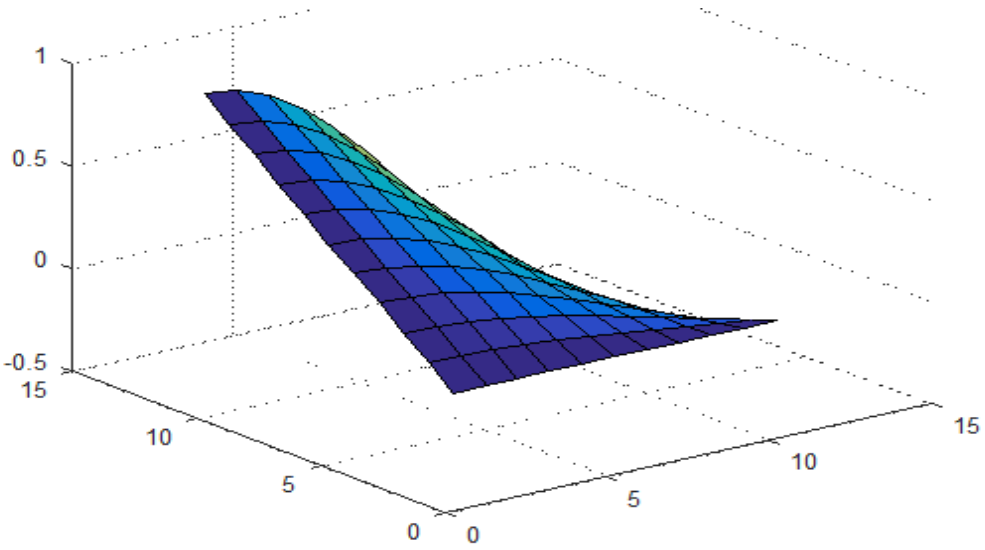

Figure 4. 10: Hyperboloid Paraboloid Surface Showing Neutron Flux in Spheroid Using Jacobi Elliptic Theta Function
(Plotted using conditions in Table 4.6)

The Fig 4.10 showed that neutrons flux increased from zero (minimum) reaching unity (maximum flux) as ARDC increased from 0 to 15. It was also observed that between 0 and 15 seconds, the flux initially increased then decreased exponentially. The Fig 4.10 was established to be a hyperboloid parabolic surface; a figure associated with Oblate Spheroids and thus confirmed that the diffusion occurred in an oblate type of spheroid, in agreement with previous studies (Alassar, 1999).

The Fig 4.11 was obtained when equation $,\psi(\xi,\tau_q) = A_i \sum_{n=0}^{\infty} \tau_q^{n^2} e^{-2in\xi}$ was adopted and conditions imposed such that the lower boundary was, L (0,0) and the upper boundary as, U (1,1), but the value of TDC and ARDC both adjusted to 0.01, respectively, while the value of 'n' maintained at unity.

Table 4. 7: Boundary conditions set 7

	Lower Boundary	Upper Boundary	Interval	'n'
TDC	0	1	0.01	1
ARDC	0	1	0.01	
Amplitude	1			

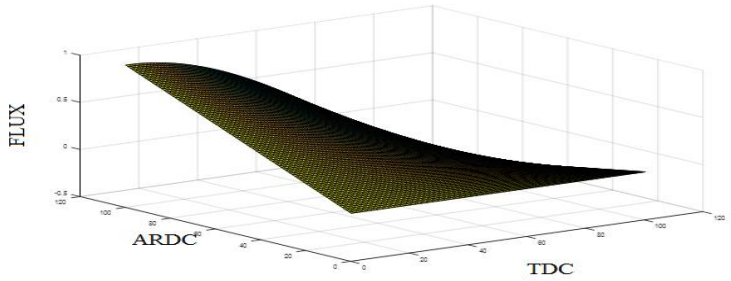

Figure 4. 11: Hyperboloid Parabolic Surface Showing Neutron Flux in Spheroid Using Jacobi Elliptic Theta Function
(Plotted using conditions in Table 4.7).

A hyperboloid paraboloid surface was obtained, as shown in Figure 4.11 but with a much smoother surface. This indicated that when smaller ARDC and TDC intervals were adopted the result was the smoothening of the diffusion surface. This observation is consistent with the study (King, 1924) that indicated the smoothening of the waveform as the number of mesh points in the plotted diffusion surface was increased.

In 2-dimensions, Fig 4.10 and Figure 4.11, respectively, were replotted and presented as shown in the Fig 4.12 b (i) and (ii) where radiative neutron flux lines were observed as ARDC increased. Interestingly, in Fig 4.12 b (ii) the flux lines regrouped into families exhibiting greater intensity than those in Fig 4.12 a (i) attributed to closer sources of neutrons described earlier. The result meant that for neutron sources that are brought closer together there's a tendency to produce smoother diffusion surfaces than when the sources are farther apart. In addition, flux behavior was shown as symmetrical along the F0-F1 shown in Figure 4.12 b

(i) - 4.12 b (ii) meaning that flux emanating from the pointed areas of the spheroid core diffused equally in all directions. Thus, despite giving new insight on the subject matter, these results also validated earlier findings in the study (King, 1924).

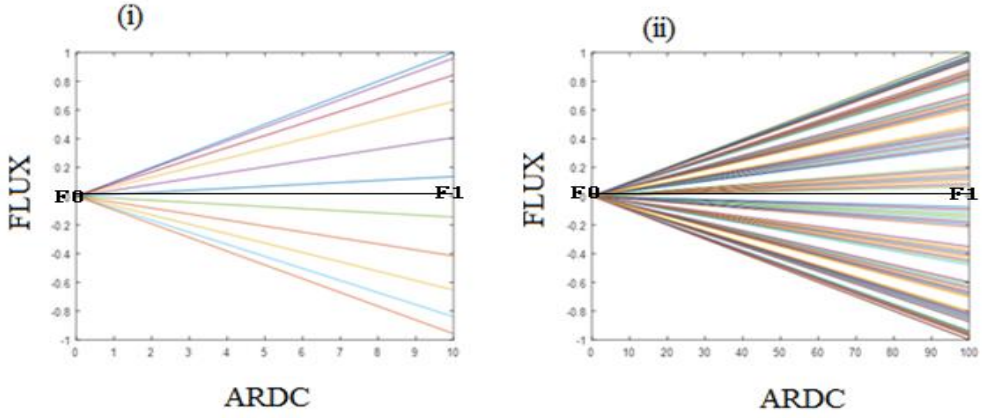

Figure 4. 12: A 2-Dimensional Neutron Flux in Spheroid Using Jacobi Elliptic Theta Function
(Plotted using conditions in Table 4.09)

When the interval for TDC was increased to 0.1 and that of ARDC maintained at unity under the wave function defined by equation 3.68 but the value of 'n' maintained at unity. The lower boundary set at L (0,0) and the upper boundary set at, U (1,10) as shown in Table 4.8 the Fig 4.13 was obtained.

Table 4. 8: Boundary Conditions Set 8

	Lower Boundary	Upper Boundary	Interval	'n'
TDC	0	1	0.1	1
ARDC	0	10	1	

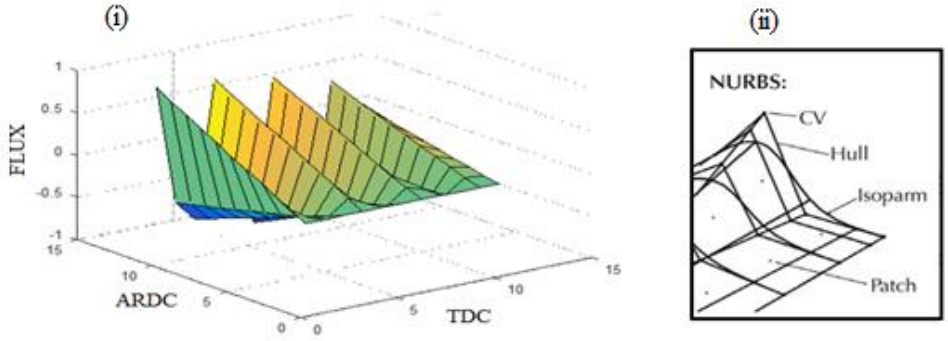

Figure 4. 13: A 3-dimensional continuous wave at 'n'=1 using Jacobi elliptic theta function

(Plotted using conditions in Table 4.8)

The results from Figure 4.13(i) showed a characteristic topological surface with tapering amplitudes along Flux/ARDC planes. Similar problems were analyzed using the method of Non uniform rational B-spline (NURBS) discussed in [(Shqair, 2019)NURBS is a mathematical method of representing curves and surfaces using computer simulations. NURBS are a form of mathematical simulations of figures in 2-D and 3-D. It provides an easy method for manipulating control vertices, curvatures and smoothness of contours. A B - Spline on the other hand uses four local functions that lie outside the curve to guide the shaping of the surfaces. This method was well illustrated in Figure 4.13 (ii).

With regard to this information, the control vertices (CV) for instance for the Figure 4.07a (i) are located at ARDC =15 when Flux = 1. The diffusion problem is therefore conforming to that of tapering isosceles triangular prisms.

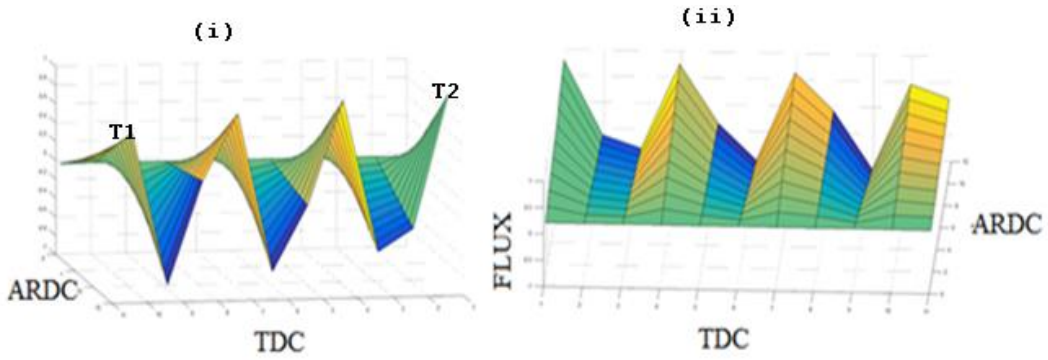

Figure 4. 14: Rear (i) and Front (ii) Flux-TDC plane view of the 3-dimensional continuous wave at 'n'=1

(Plotted using Conditions in Table 4.8)

It was observed that there were more perturbations appearing at smaller values of TDC than at larger values of TDC as attested by Figure 4.14 (i). This is shown in Figure 4.07b (i) whereby flux for T1 = 5 and T2 = 17, thus flux was progressively undergoing damping as TDC progressed. It is also evident that flux increased in amplitude with increase in ARDC between 0-15 alluding to more perturbations at higher values of ARDC.

A slightly different scenario from Figure 4.14(i) and 4.14(ii) emerged when the equation , $\psi(\xi, \tau_q) = A_i \sum_{n=0}^{\infty} \tau_q^{n^2} e^{-2in\xi}$,was adopted under conditions such that the lower boundary was L (0, 0) and the upper boundary U (1,100) the TDC and ARDC components were set at 0.01 and 1 respectively. The conditions in Table 4.9 have been used to obtain the results obtained in Figure 4.15.

Table 4. 9: Boundary conditions set 9

	Lower Boundary	Upper Boundary	Interval	'n'
TDC	0	1	0.01	1
ARDC	0	100	1	

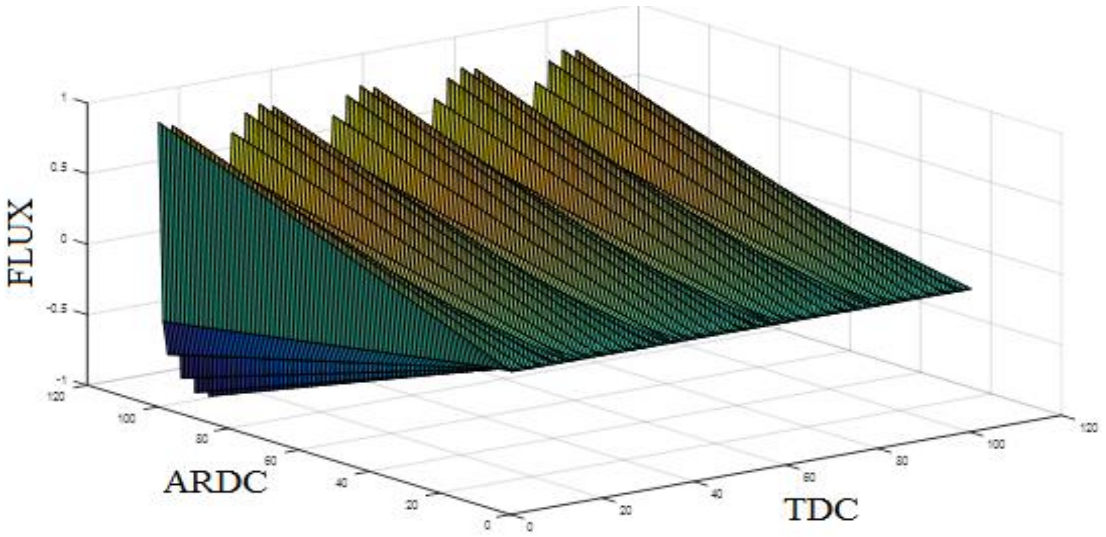

Figure 4. 15: A 3-Dimensional continuous wave at 'n'=1 using Jacobi elliptic theta function

(Plotted using conditions in Table 4.9)

Although the Figure 4.15 exhibited some similarities with Figure 4.14 i.e. periodicity and continuity, a major difference was that whereas Figure 4.14 was relatively smoother than Figure 4.15 at higher values of ARDC compared to smaller values. Specifically, the unevenness of the wave function was observed between ARDC (60 - 120). This was an indication of increased perturbation occurring at the set conditions.

The waves further projected the property of damped oscillations at smaller ARDC values than at larger values. It was summed that while Figure 4.14, exhibited a behavior of a cylindrical surface, Figure 4.15 presented major similarities to a rough, right conical diffusion properties.

Using conditions presented in Table 4.10, equation $,\psi(\xi,\tau_q) = A_i \sum_{n=0}^{\infty} \tau_q^{n^2} e^{-2in\xi}$,was adopted and the lower boundary set at L (0, 0) and the upper boundary U (1,10), TDC and ARDC intervals set at 0.01 and unity respectively while the value of 'n'=1, the Figure 4.16 was obtained.

Table 4. 10: Boundary conditions set 10

	Lower Boundary	Upper Boundary	Interval	'n'
TDC	0	1	0.01	1
ARDC	0	100	1	

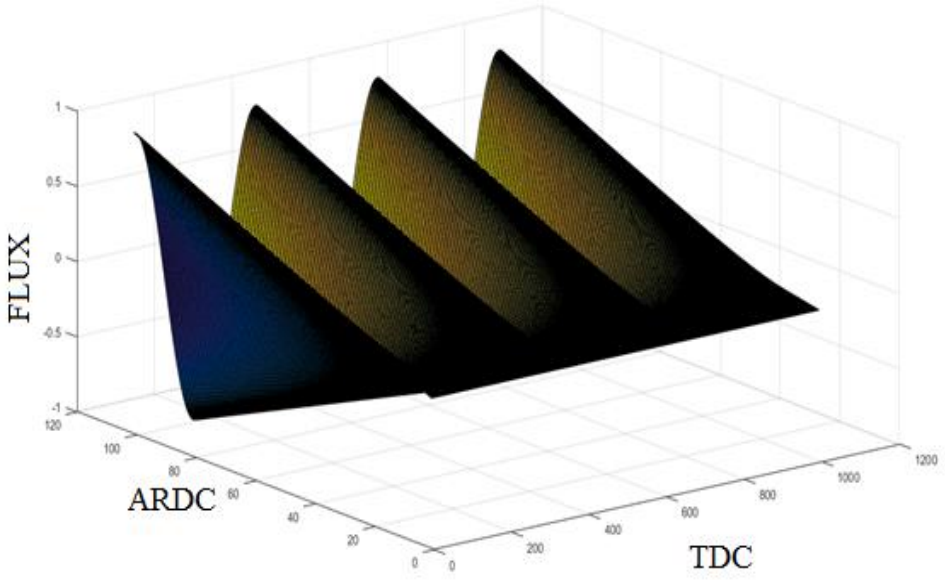

Figure 4.16: A 3-dimensional continuous wave at 'n'=0.1 using Jacobi elliptic theta function

(Plotted using conditions in Table 4.10)

It was observed that at TDC = 0, the flux amplitude of the wave increased gradually from zero to maximum (1), a behavior that was replicated periodically at TDC = 400, 800 and 1200. Secondly, it was noted that as TDC elapsed between 0 to 1200 units flux remained unique to the value of TDC at that point. It was concluded that the figure was affected by changes in both ARDC and TDC according to the equation of diffusion. The results presented in Figure 4.16 provided a typical illustration of a continuous periodic 3-dimensional wave with smooth surfaces. Unlike Figure 4.11 where the interval was set at a similar value for both ARDC and TDC, in Fig 4.16, the intervals were varied such that interval (TDC = 0.01) and interval (ARDC = 0.1) were dissimilar. Thus, this difference in

the interval set for the wave function was deduced to have largely contributed to the apparent change in the flux behavior in the latter. This figure can be described as a continuous periodic right conical diffusion surface.

We now conclude this sub-section by asserting that the diffusion surfaces obtained when ‘n’=1 were mostly continuous periodic surfaces with tapering ends. Secondly, smaller intervals between ARDC and TDC were found to enhance the smoothness of the diffusion surface. In addition, the diffusion surfaces are mostly parabolic hyperboloids and asymmetrical continuous 3-dimensional surfaces with tapering ends. The later phenomenon was attributed to the attenuation of the waves as they propagate through the spheroid core.

4.2.3 Diffusion surfaces for values of ‘n’ greater than unity i.e. ($1 \geq n \leq 100$)

In this section, the values of ‘n’ were varied between $1 \geq n \leq 100$ specifically selected at ‘n’ = 2, 5, 10 and 100. This range of values selected arbitrarily since they gave the possible range of values expected from the perturbations.

To start with, the value of ‘n’ was set at ‘n’ = 2 and conditions imposed such that the lower boundary, L (0,0) and the upper boundary U (1,100), the TDC and ARDC components set at 0.01 and 1 respectively. The Fig 4.17 was obtained.

Table 4. 11: Boundary conditions set 11

	Lower Boundary	Upper Boundary	Interval	‘n’
TDC	0	1	0.01	2
ARDC	0	100	1	

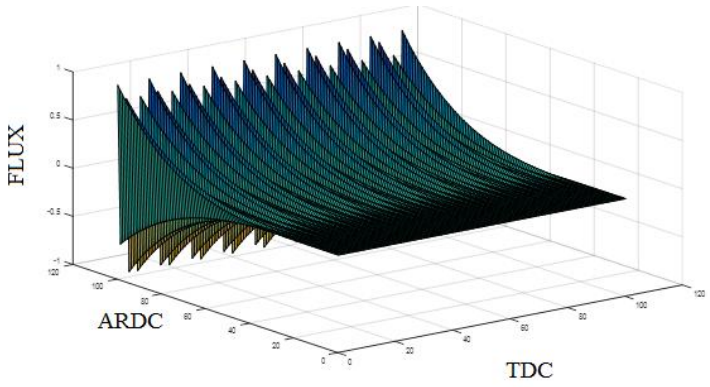

Figure 4.17: A 3-Dimensional Discontinuous Periodic wave at 'n' = 2 using Jacobi elliptic theta

(Plotted using conditions in Table 4.11)

The results were characterized by the waveform exhibiting rapid oscillations at values of ARDC > 60 compared to values of ARDC < 60 and appeared rapidly fractal as the values of ARDC approached 120 (Figure 4.17). Another observation made along the TDC was that the waveform was largely periodic. Thus, the graph exhibited the behavior of dynamic evolution of linearly dispersive waves on periodic domains. It evolved into an asymptotic sub linear dispersion relation with dispersive fractalization.

Secondly, the value of 'n' was increased further to 'n' = 5 and conditions applied on equation , $\psi(\xi,\tau_q) = A_i \sum_{n=0}^{\infty} \tau_q^{n^2} e^{-2in\xi}$,such that the lower boundary was set was L (0,0) and the upper boundary set as U (1,1), the TDC and ARDC components set at 0.01, Fig 4.18 was obtained.

Table 4. 12: Boundary conditions set 12

	Lower Boundary	Upper Boundary	Interval	'n'
TDC	0	1	0.01	5
ARDC	0	1	0.01	

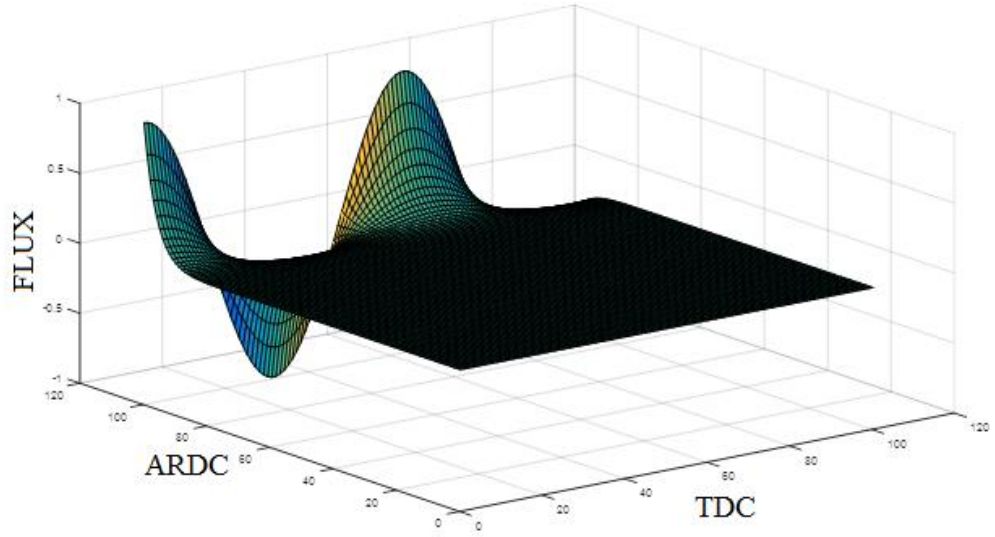

Figure 4. 18: A Hyperboloid paraboloid graph showing neutron flux in spheroid using
JETF (Plotted using conditions in Table 4.12)

The results from Figure 4.18 characterized a ternary surface whereby neutrons flux developed two maxima and two minima at higher values of ARDC > 80. The maxima occurred at TDC = 0 and TDC = 60, while the local minima occurred at TDC = 20 and TDC = 120.The results therefore pointed to wave damping at large axis ratios (ARDC > 80) where rapid oscillations of the wave function resulted in the formation two saddles compared to smaller axis ratios (ARDC < 40) where flux was observed to be constant. Based on these findings, it was concluded that the diffusion surface shown was thus a hyperboloid paraboloid diffusion surface.

A 2-dimensional neutron diffusion flux was also plotted using 'n'=5 and conditions imposed on equation , $\psi(\xi,\tau_q) = A_i \sum_{n=0}^{\infty} \tau_q^{n^2} e^{-2in\xi}$,such that the lower boundary was set as L (0,0) and the upper boundary set as U (1,1), the TDC and ARDC components set at 0.01. Figure 4.19 was formed.

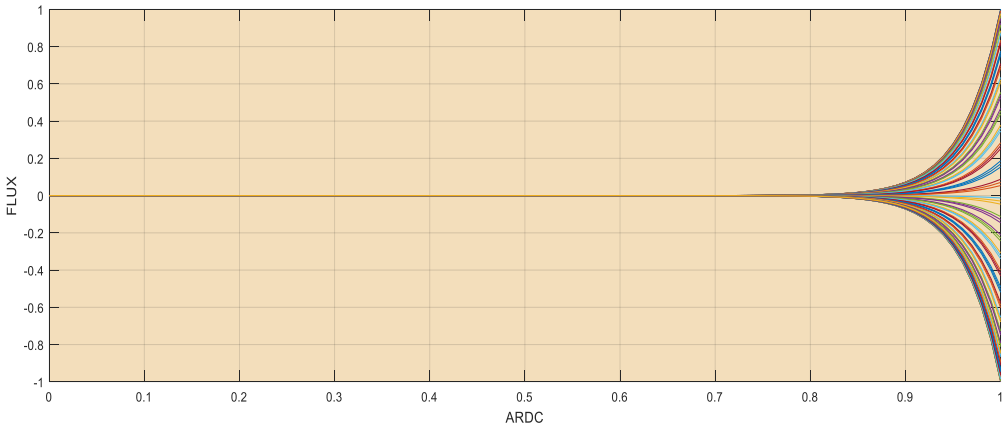

Figure 4. 19: A 2-dimensional graph showing neutron flux in spheroid using Jacobi elliptic

(Plotted using Conditions in Table 4.12)

The results exhibited neutron flux emerging in a linear pattern between ARDC (0 - 0.8), thereafter, i.e. between ARDC (0.8 > 1), it developed into a family of symmetrical curves along the flux line (Zero) as shown in Figure 4.19. These curves provided an indication that the wave underwent rapid oscillations at higher ARDC values and damped to zero for smaller ARDC values (0 - 0.8).

Table 4. 13: Boundary conditions set 13

	Lower Boundary	Upper Boundary	Interval	'n'
TDC	0	1	0.01	5
ARDC	0	100	1	

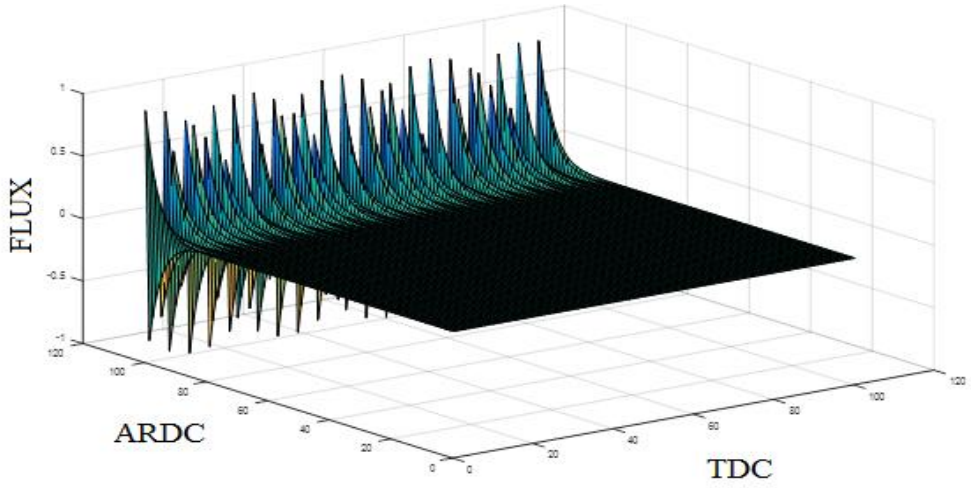

Figure 4. 20: A 3-Dimensional Discontinuous Periodic wave at 'n'=5 using Jacobi elliptic theta function

(Plotted using conditions in Table 4.13)

The fractalization of the waveforms in the Figure 4.20 at higher values of ARDC was found to be similar to that in Figure 4.17 and 4.18 but appeared more pronounced in the latter. This meant that there was the existence of more rapid oscillations than in Figure 4.17/18. In contrast, one similarity exhibited was on the fact that the waveform remained periodic for both graphs a TDC increased. The increased fractalization of the waveform was attributed to the change in the value of 'n' that was increased from 2 to 5. This could have signified that higher order Jacobi elliptic theta functions produced more wave fractalization of waves than smaller order functions.

The value of 'n' was set at 10 and 100 under the conditions such that the lower boundary was set was L (0,0) and the upper boundary set was U (1,100), the TDC interval was 0.01 and ARDC interval set at unity Fig 4.21 was obtained.

Table 4. 14: Boundary conditions set 14

	Lower Boundary	Upper Boundary	Interval	'n'
TDC	0	1	0.01	10 for Figure (i)
ARDC	0	100	1	100 for Figure(ii)

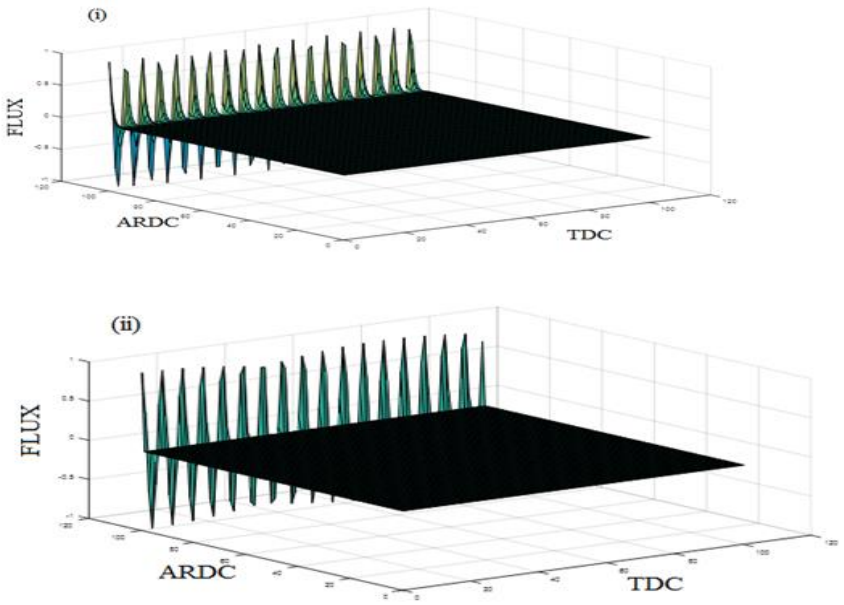

Figure 4. 21: 3-dimensional discontinuous Periodic wave at (a) 'n'=10 and (b) 100 using Jacobi elliptic theta function

(Plotted using conditions in Table 4.14).

The results depicted that flux showed insignificant growth as ARDC increased to values slightly less than 100. However, as ARDC approached 100, flux was shown to grow from minimum to maximum periodically with increase in TDC. Additionally, the spikes in the waveform were observed as less pointed compared to previous observation made in Fig 4.20. It was noted that as the values of 'n' increased so that 10 < 'n' < 100, no significant change in the behavior of the waveform occurred as attested in Figure 4.21(ii). However, a slight variation between the two figures was evident as demonstrated by Figure 4.21(ii) which had

comparatively more uniform pointed waveforms than Figure 4.21(i). This was summed up to mean that higher ‘n’ values yielded more uniform discontinuous waveforms than smaller n values.

In a quest to gain more insight on the results, figure 4.19 - 4.21 were generated in 2-dimensions; this was accomplished as a plot between Flux and the ARDC and presented in Figure 4.13b,

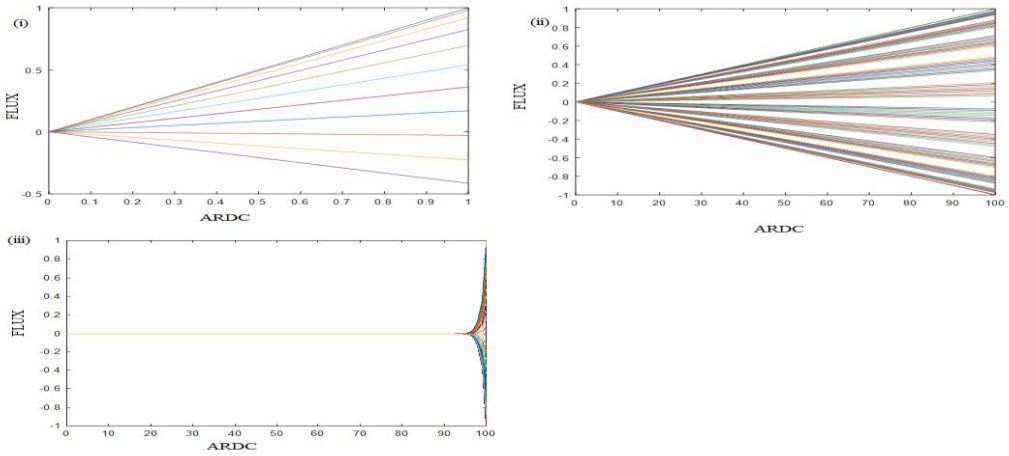

Figure 4. 22: 2-Dimensional Neutrons Flux Inside A Spheroid Reactor Core Using Jacobi Elliptic Theta Functions (‘N’=2, 3 And 5)
(Plotted using conditions in table 4.13).

Generally, when the value of ‘n’ was increased, neutron flux appeared to disperse more rapidly at larger ARDC values than at smaller values. This fact was exemplified when ‘n’ was set at ‘n’=2, 3 and 5, the graphs showed neutrons initial flux growth took place at approximately ARDC = 30, 80 and 98 for Figure 4.22 (i), Figure (ii) and Figure (iii) respectively. Another key observation made from the graphs was regarding the pattern of flux in which case the results at ‘n’=2 showed the flux growth assuming flux families’ lines as illustrated in Figure 4.22 (ii).

A slightly different deviation from this results was made when the lower boundary was maintained at L (0, 0) and the upper boundary adjusted to U (1,10), the TDC and ARDC components were both set at 0.01 and value of 'n'=10, furthermore, the wave function was maintained as equation , $\psi(\xi, \tau_q) = A_i \sum_{n=0}^{\infty} \tau_q^{n^2} e^{-2in\xi}$, after plotting, the graph 4.23 was obtained.

Table 4.15: Boundary conditions set 15

.	Lower Boundary	Upper Boundary	Interval	'n'
TDC	0	1	0.01	10
ARDC	0	10	0.01	

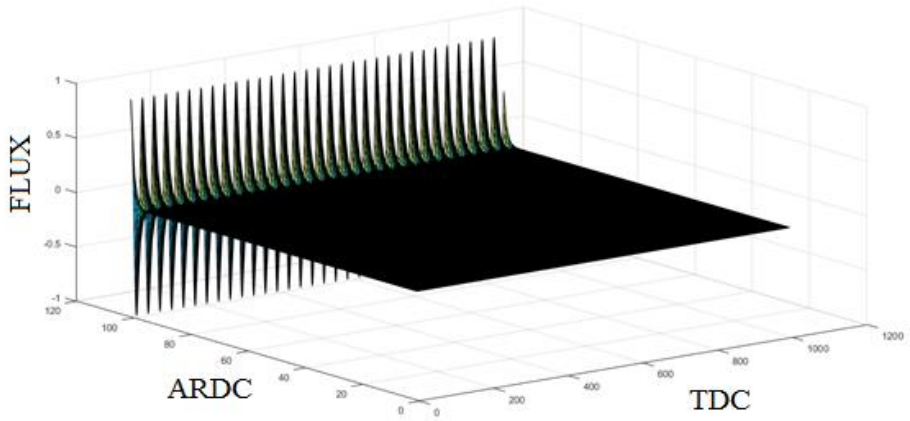

Figure 4.23: A 3-Dimensional Discontinuous Periodic wave at 'n'=10 using Jacobi elliptic theta function

(Plotted using conditions in Table 4.15)

The results showed that although there was no significant growth in flux exhibited as ARDC increased from zero towards 120, the flux wavelength for each wavelet appeared to have reduced significantly compared to those in Figures 4.18 - 4.22. Secondly, the wave peaks became sharper and more uniform than those of Figure 4.20 - and 4.21(i) and (ii), a behavior that was attributed to the interval set uniformly at 0.01 for both ARDC and TDC in the Figure 4.11 unlike other where different values of the intervals, (TDC = 0.01 and ARDC = 1) were adopted.

All the Figures 4.22 - 4.24 were all found to share a commonality of being discontinuous 3-dimensional periodic waves. However, a slight variation in size of the wavelength and the pattern and sharpness of the peaks was also evident as the BCs and the value of 'n' were varied.

Generally, rapid oscillations were observed for higher ARDC values (ARDC ≥ 90) than for smaller ARDC values in which case the oscillations were found to be highly damped. The behavior was also established to be periodic along TDC.

Another emergent behavior from the results in this study was the formation of waveforms each with four distinct regions. This results were produced when the boundary conditions were such that the lower boundary was maintained at L (0, 0), the upper boundary adjusted to U (1,10), the TDC and ARDC intervals both set at 0.01 while the value of 'n'=10, the wave function was maintained as equation $,\psi(\xi,\tau_q) = A_i \sum_{n=0}^{\infty} \tau_q^{n^2} e^{-2in\xi}$ and plotted in 2-dimensions to produce the Figure 4.24.

.

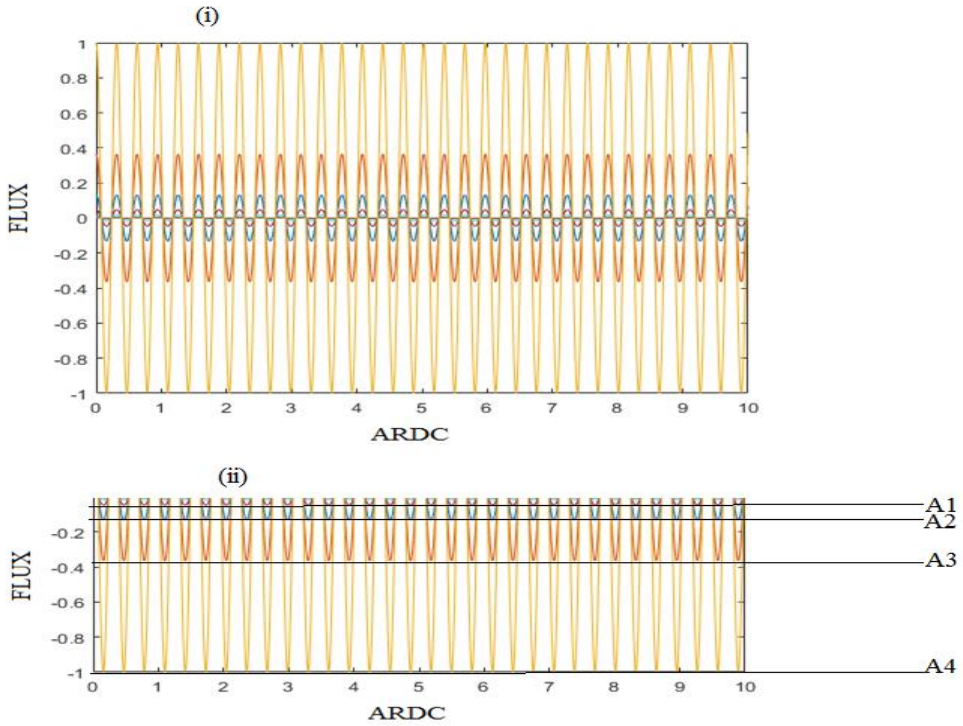

Figure 4. 24: 2-dimensional Periodic wave at 'n'=10 using Jacobi elliptic theta function

(Plotted using conditions in Table 4.17)

It was established that flux was periodic as ARDC increased between ARDC (0-10). The uniformity of the waveforms was also clearly manifest since all the wavelets were characterized by uniform periodicity (Figure 4.24). Secondly, each wavelet was observed to possess four distinct regions as shown by the amplitudes labeled as; A1, A2, A3 and A4 respectively. In addition, all the waveform amplitudes were superimposed such that A1 < A2 < A3 < A4. This observation was not new since similar findings are corroborated in (Alassar, 1999) where the full contours were found to be nearly circular near the source but slowly developed into elliptical shapes as neutrons moved outwards towards the boundaries of the reactor core. From the fact that similar findings as in other studies were observed reinforces both the methods and results adopted in this study.

4.2.4 Summary of Key findings from Jacobi elliptic theta functions

In summary, it was observed that for values of 'n' less than unity, the diffusion surfaces generated were largely influenced by the other conditions of the equation, $\psi(\xi, \tau_q) = A_i \sum_{n=0}^{\infty} \tau_q^{n^2} e^{-2in\xi}$. These conditions were mostly related to the values of ARDC and TDC. The interval between the values was shown to influence the smoothness of the surface while the amplitude was shown not to affect the surface type generated but only influenced the rate at which the flux reached its saturation. For instance, at 'n'= 0.1, the results produced both ternary surface and continuous periodic functions. At 'n'=0.5, periodic functions with sharp peak was witnessed. As 'n' was further reduced to 0.01, complex surfaces were generated that was characterized by multiple surfaces on different planes.

The diffusion surfaces obtained when 'n'=1 were mostly continuous periodic surfaces with tapering ends. Secondly, smaller intervals between ARDC and TDC were found to enhance the smoothness of the diffusion surface. In addition, the diffusion surfaces are mostly parabolic hyperboloids and asymmetrical continuous 3-dimensional surfaces with tapering ends. The later phenomenon was attributed to the attenuation of the waves as they propagate through the spheroid core.

As the value of 'n' became greater than unity, it was shown that the waves transformed from ternary surfaces to continuous and discontinuous 3-dimensional surfaces. It was further observed that as the value of 'n' increased progressively, the peak of the waves of the surfaces became smoother and uniform. This pointed to the saturation of the flux as explained by (Woods & Palmer, 2017)

4.3 Analysis of neutron flux using Analytic Method.

In this section, analysis of diffusion equation was carried out using analytic method. This was accomplished in two ways; by varying the conditions of equation 3.27 and secondly by modifying the terms of the same equation. The aim was to understand how the flux behaved when these changes were made.

4.3.1 Dominant Time-Dependent Component.

To start with, the equation derived in the function, $\psi(g_1, g_2) = G(g_1, g_2)e^{(g_1)}$, was plotted in 3- dimensions with conditions imposed such that the TDC and the ARDC had their lower boundary as L (0,0) and the upper boundary as U (100,0), the TDC had an interval of 0.1 while ARDC had a zero time component. The amplitude limits were set at L (0, 0) and U (100,100), a common interval of unity and the amplitude term as, $G(\eta, \xi) = -a + bi$, were adopted to plot the graph shown below.

Table 4.16: Boundary conditions set 16

	Lower Boundary	Upper Boundary	Interval
TDC (g_1)	0	1	0.01
ARDC(g2)	0	0	Not defined
a	0	100	1
b	0	100	1

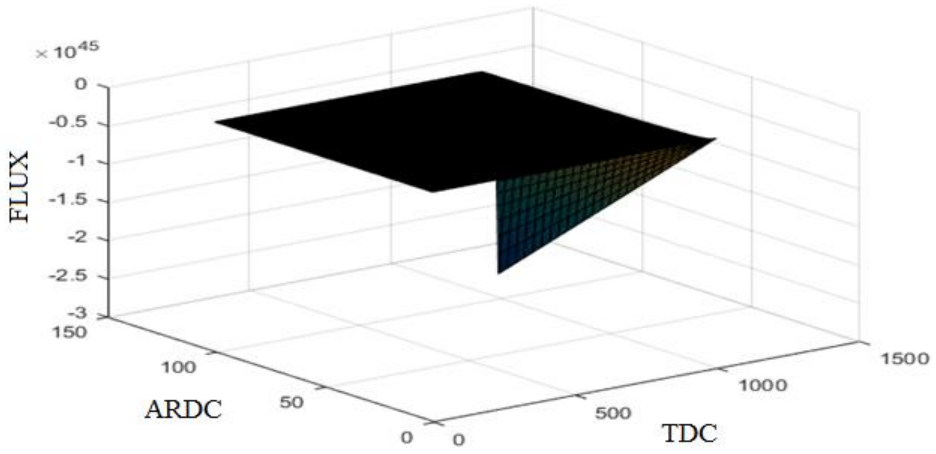

Figure 4. 25: Door-Hinge ternary surface generated using Analytic method
(Plotted using Table 4.16)

The formation of ternary surfaces with two 'wings' was also part of the spectrum of results established in this thesis. It was displayed in Figure 4.25 which showed flux assuming a maximum (-0.5) between ARDC (0 - 150), then remained constant as TDC was altered from Zero to slightly below 1000. However, as TDC approached 1000, the flux dropped from maximum, (-0.5) to minimum (-3) in a triangular planar surface.

In addition, attention was shifted to understand the nature of ternary surfaces that were produced as TDC and ARDC lower boundaries L (0, 0) and the upper boundary U (10, 0), with a TDC interval of 0.1 adopted. The amplitude term was, $G(\eta, \xi) = a + bi$ and the amplitude limits were set at L (0, 0) and U (10, 10) and both limits set with an interval of unity. The function; $\psi(g_{1,}g_2) = G(g_{1,}g_2)e^{(-g_1)}$.

Table 4. 17: Boundary conditions set 17

	Lower Boundary	Upper Boundary	Interval
TDC (g_1)	0	10	0.1
ARDC (g_2)	0	0	Not defined
a	0	10	1
b	0	10	1

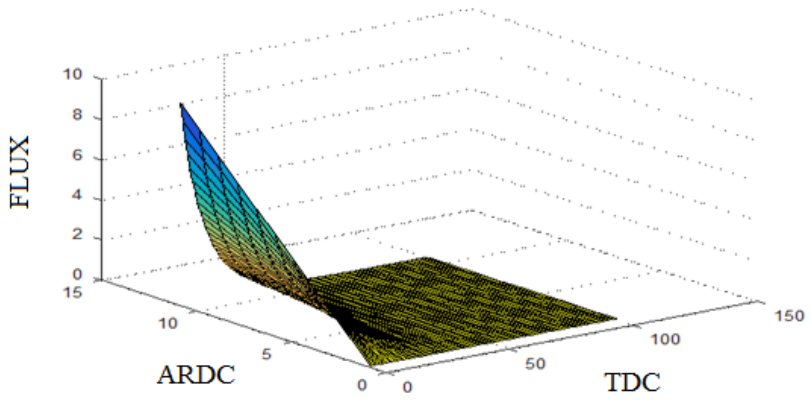

Figure 4.26: Hyperbolic paraboloid surface generated using Analytic method
(Plotted using conditions in Table 4.17)

The hyperbolic paraboloid in figure 4.26 depicted neutrons flux with two main surface orientations, the first orientation occurred between TDC (50-60) whereby the flux remains constant at zero even as ARDC increased. The second orientation occurred between TDC (0-50) when the diffusion followed a curved behavior with flux gradually increasing from 0 to 8 units as ARDC increased from 0 to 15 units.

In order to further understand the properties of figure 4.26, a 2-dimensional plot shown in graph 4.27 was plotted using conditions in Table 4.17.

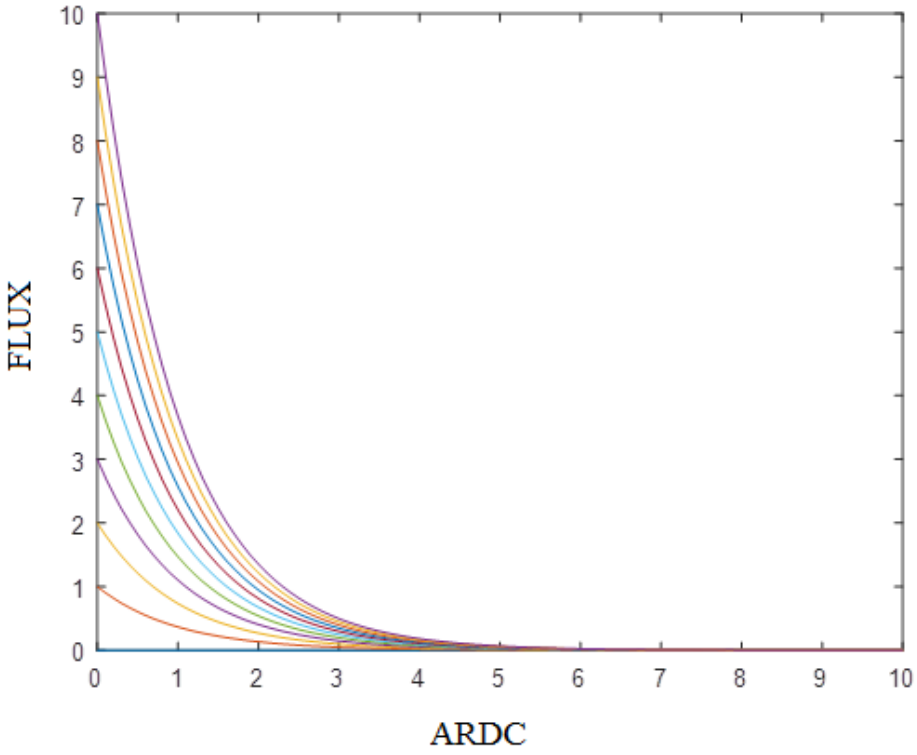

Figure 4. 27: A 2-dimensional plot generated using Analytic method
(Plotted using Conditions 4.17).

Deducing from Figure 4.27, it can be asserted that neutrons diffused along the Flux-ARDC plane while decreasing exponentially from maximum and converged for ARDC values between 6 - 7. In addition, it was apparent that the initial flux had vanished to zero within similar range of ARDC. The results therefore

suggested that flux underwent damping between ARDC (5-10) with neutrons with higher initial flux amplitude underwent rapid damping than those with smaller initial flux amplitude.

4.3.2 Flux for Diffusion equation with Dominant Axis Ratio Dependent Component

The Figure 4.18a was generated with conditions imposed such that the TDC and the ARDC had their lower boundary set at L (0, 0) and the upper boundary U (0,100), the TDC and ARDC both with an interval of 0.1. The amplitude terms, $G(\eta,\xi) = -a + bi$ and amplitude limits set at L (0, 0) and U (100,100), both with an interval of unity. The function; $\psi(g_{1,}g_2) = G(g_{1,}g_2)e^{g_2 i}$ was adopted.

Table 4.18a: Boundary conditions set 18.

	Lower Boundary	Upper Boundary	Interval
TDC (g_1)	0	1	0.01
ARDC (g_2)	0	0	Not defined
a	0	100	1
b	0	100	1

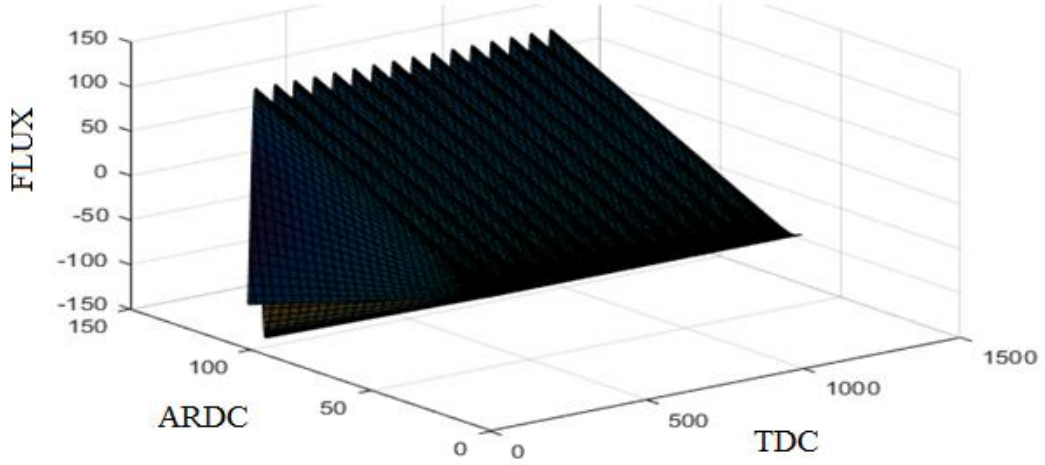

Figure 4. 28: Continuous periodic 3-dimensional graph generated using Analytic method

(Plotted using conditions in Table 4.18)

Part of the configuration of neutron flux under the stated conditions was the formation continuous periodic 3 - dimensional flux with increasing amplitudes as ARDC varied from zero towards 150. For instance, at TDC = 0, the flux amplitude of the wave was shown to increase gradually from zero to maximum (150); a behavior that was replicated periodically along the TDC axis between zero and 1500 units.

Using similar conditions in Table 4.18, a 2-dimensions figure 4.29 was developed. The results from showed that the neutrons diffusion behavior near the core was similar to an oblate spheroid shown as A4 in Figure 4.29 (ii). Similarly, it is understood that as neutrons diffuse outwards, they exhibited a behavior similar to a spherical surface (A3) and finally, prolate behavior (A2) in the Figure.

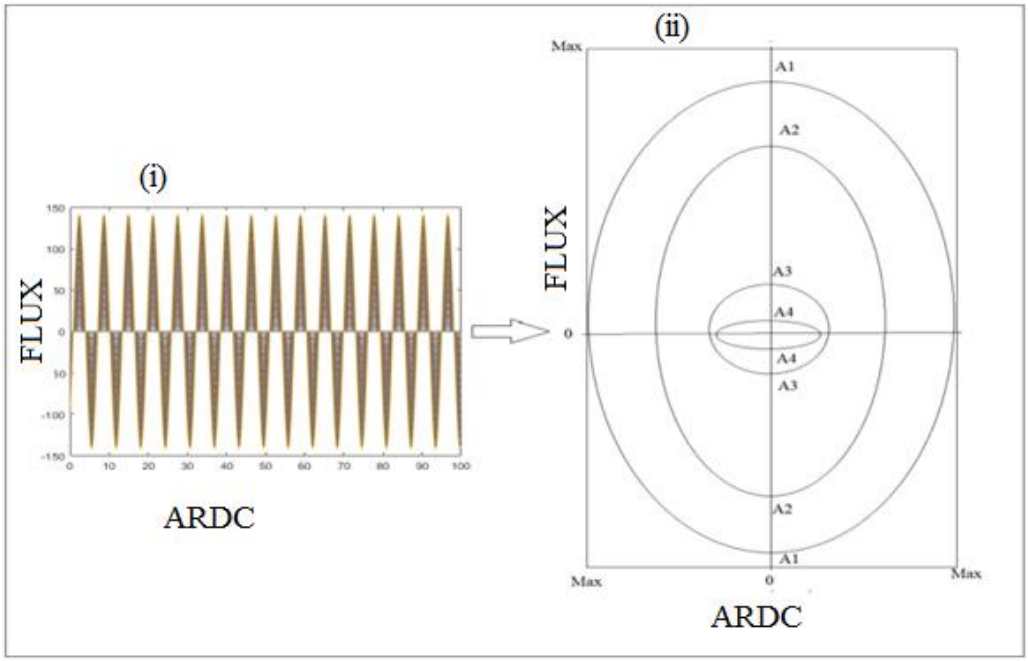

Figure 4. 29: 2-Dimensional graph generated using analytic method
(Plotted using conditions in Table 4.18)

These results elude to the fact that as time progressed, more neutrons are likely to be found near the surface of the spheroid and thus increase the probability of leakage outside the reactor similar to heat diffusion in spheroids (Alassar et al., 2014).The heat diffusion and the neutron diffusion problem have one major striking difference where unlike heat diffusion problem mentioned Figure 4.29 in (Alassar et al., 2014), the flux for each type of spheroid are not determined separately i.e. the distinction between the neutron flux for a prolate and oblate was not made.

In the study by Woods and Palmer (2017), a manufactured solution was adopted with discretization terms. The study revealed the formation of complex figures arising from different streaming and source terms, from the different Ω values as shown in the Figure 4.30.

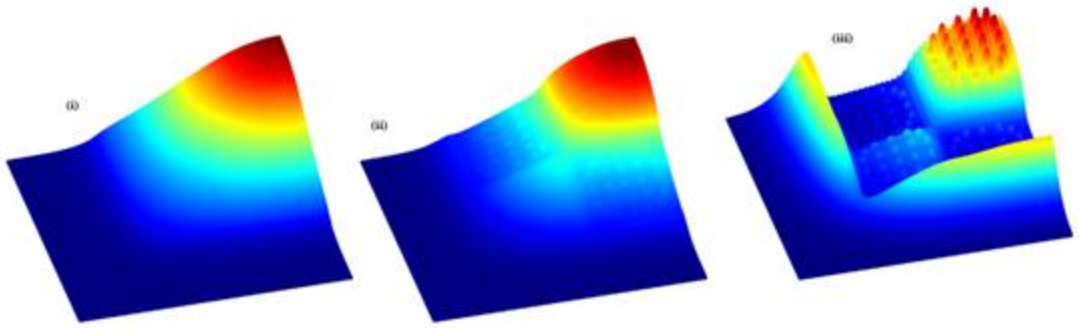

Figure 4. 30: Analytic solution for the transport equation using a manufactured solution

(Hannaske et al., 2013).

The results in this study particularly, those in Figure 4.15 and Figure 4.16 have been found to be in conformity to the results shown in Figure 4.30(c) (i-iii). The center of the diffusion problems represented by the red color indicated a high level of hotness compared to the edges of the spheroid. These hotter areas in Figure 4.30

may represent highly perturbed regions of the neutron flux mention in Figure 4.25-4.28 that were considered as hyperbolic paraboloids diffusion configuration.

Based on a study carried out to determine the relationship between flux and the semi focal distance of a spheroid (Lima et al., 2004) with results as shown in figure 4.18d, It was concluded that a slight deformation from the sphere does not affect the fundamental mode properties significantly but at least to the first order. Secondly it was found that a disk and a sphere were two limiting cases for spheroids that exhibited smooth transitions between two limits. Thirdly, full contours were found to be nearly circular near the source but slowly developed into elliptical shapes moving towards boundaries.

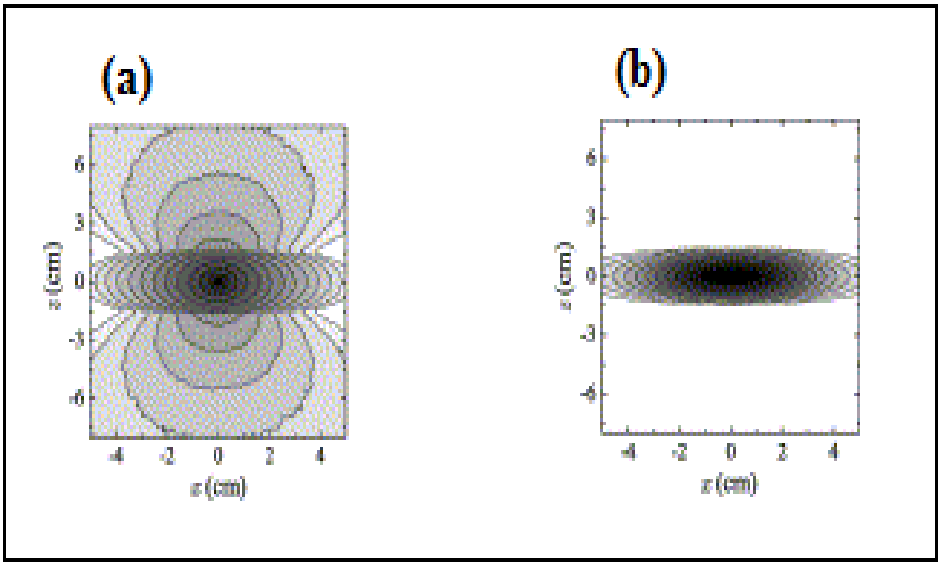

Figure 4. 31: Plot of flux against focal distance (a) monte carlo (b) analytical method

The results from Figure 4.31 further confirmed the fact that neutron flux at the core of a spheroid was spherical but became elliptical as the flux moves outwards that were deduced earlier in Figure 4.29 and Figure 4.30.

4.3.3 Flux for diffusion equation with both TDC and ARDC Dominant Component

It $\psi(g_{1,}g_2) = G(g_{1,}g_2)e^{-(g_1+g_2 i)}$ was adopted while the boundary conditions were altered such that both the boundaries for TDC as well as ARDC were set as L (0, 0) and U (100,100) respectively while their intervals were set at 0.1. The amplitude term remained as, $G(\eta, \xi) = -a + bi$ whle the amplitude boundary conditions were similarly set at L (0, 0) and U (100,100) with an interval of unity for both boundaries. Consequently the Figure 4.32 was obtained.

Table 4.18b: Boundary conditions set 19

	Lower Boundary	Upper Boundary	Interval
TDC (g_1)	0	100	0.1
ARDC (g_2)	0	100	0.1
a,b	0	100	1

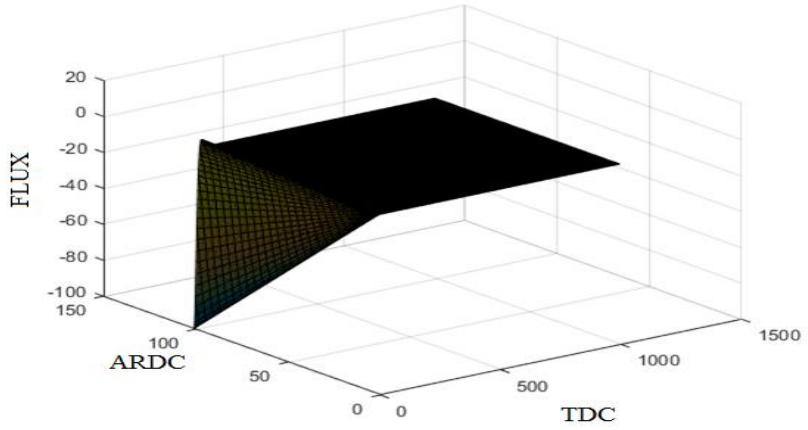

Figure 4. 32: A Door-Hinge ternary surface generated using Analytic method (Plotted using conditions Table 4.19).

It was deduced that the formation of a ternary surface occurred with two 'wings' similar to that in Fig 4.32 occurred. Initially, flux assumed a maximum (0) between ARDC (0-150) and thereafter dropped slightly below (0) then remained constant as TDC varied between 0 to slightly below 1500. Contrastingly, as TDC

approached Zero, a change in behavior was exhibited when flux dropped from maximum (0) to minimum (-100) in a characteristic curved triangular ternary surface. Additionally, a curved cylindrical surface was observed between the two ternary surfaces.

When similar boundary conditions were maintained as shown in Table 4.19 while the function $\psi(g_{1,}g_2) = G(g_{1,}g_2)e^{-(g_1+g_2 i)}$ was adopted from $\psi(g_{1,}g_2) = G(g_{1,}g_2)e^{(g_1-g_2 i)}$ that was adopted earlier and similarly the amplitude function was maintained as $(\eta, \xi) = -a + bi$.

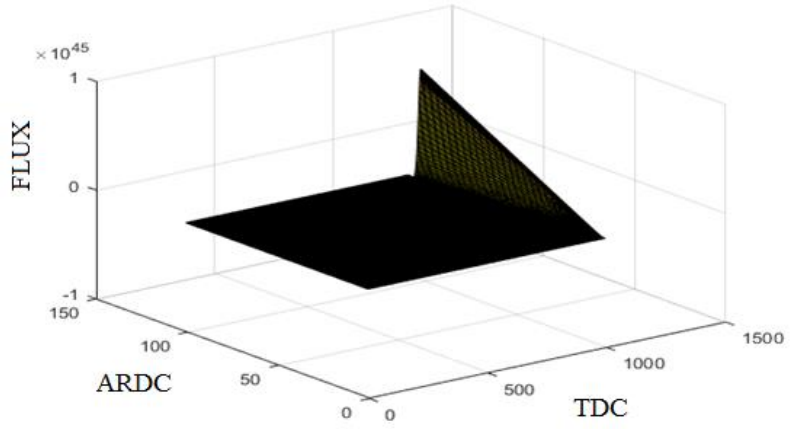

Figure 4.33: 'Dovetail-like' ternary surface generated using Analytic method
(Plotted using conditions in Table 4.19)

Based on the figure 4.32 and Figure 4.33, it was inferred from the result that there was rotation by 180 degrees in the clockwise direction. Another observation drawn from the study was regarding the formation of elliptic paraboloid surfaces. This was realized when conditions were imposed on equation 3.68 such that the TDC and ARDC boundary values were; lower boundary L (0, 0) and the upper boundary U (10, 10) the TDC and ARDC both with an interval of 0.1. The amplitude terms were set at, L (0,0) and, U (10,10) and both with an interval of unity. The function;

$\psi(g_{1,}g_2) = G(g_{1,}g_2)e^{(g_1-g_2 i)}$ was adopted and an amplitude term modified as, $G(\eta,\xi) = -a - bi$ the Fig 4.34 below was obtained;

Table 4. 19: Boundary conditions set 20

	Lower Boundary	Upper Boundary	Interval
TDC ($\sim g_1$)	0	10	0.1
ARDC ($\sim g_2$)	0	10	0.1
a	0	10	1
b	0	10	1

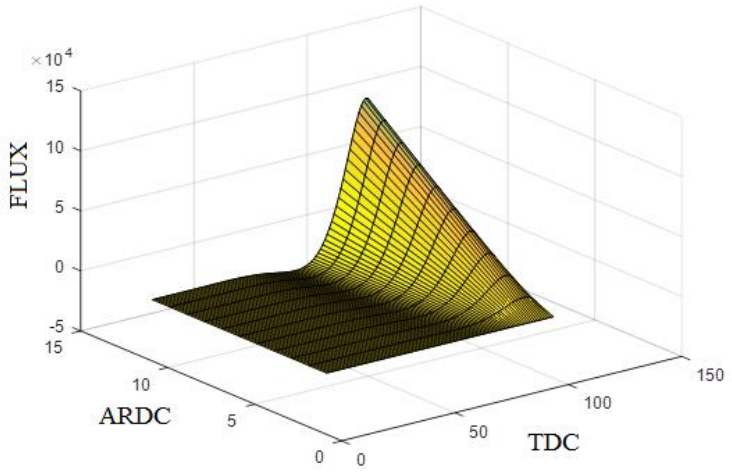

Figure 4. 34: An elliptic paraboloid surface generated using Analytic method (plotted using conditions 4.20)

The findings evidenced the formation of a ternary surface with two distinct planes; the first planes were largely rectangular surface that resembled a cone-like quadric surface. The rectangular surface showed that flux remained fairly constant as both ARDC and TDC were increased. However, as TDC approached 100, a cone like quadric surface emerged. Therefore, the diffusion demonstrated how neutron flux increased from minimum (0) and rose to maximum (10) following the two forms of surfaces. This feature was found to resemble an elliptic paraboloid surface (Li

et al., 2004)for ARDC (100-150) while ARDC (0-100) exhibited a hyperboloid paraboloid surface (Ivers, 2004)

When the wave function was varied to $\psi(g_{1,}g_2) = G(g_{1,}g_2)e^{(g_1+g_2 i)}$ and the amplitude function$G(\eta, \xi) = -a + bi$, the TDC and ARDC both with an interval of 1 an interval of 0.1 respectively while the other remaining variables held constant, Figure 4.35 was obtained.

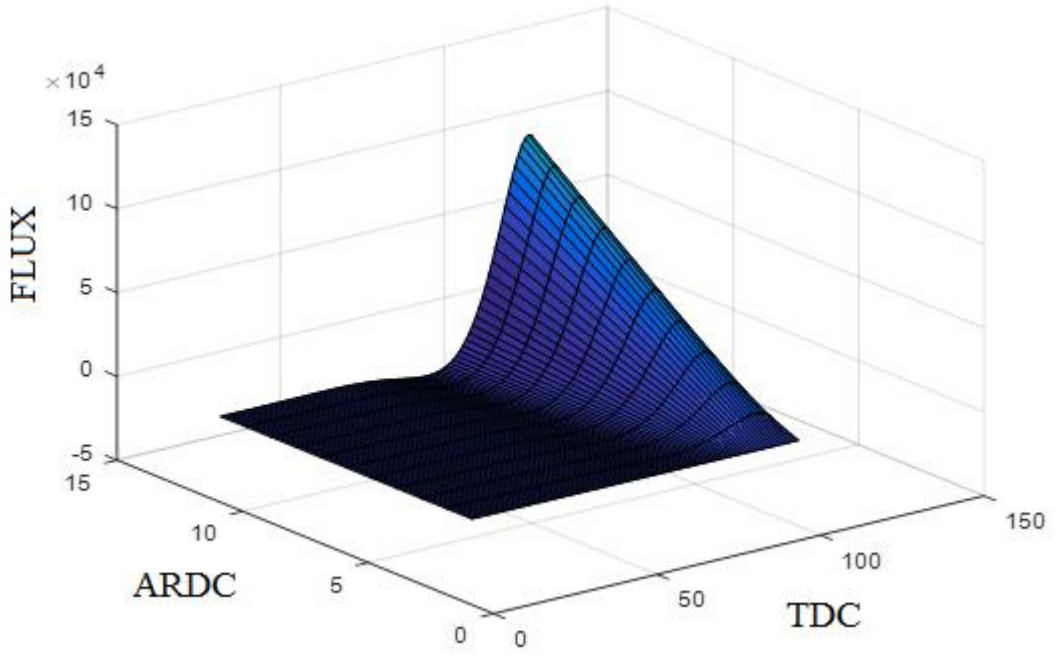

Figure 4.35: An elliptic paraboloid surface generated using Analytic method (Plotted using conditions in Table 4.20).

The two Figures 4.34 and Figure 4.35 were compared and found to be largely similar. In addition, it was also established that neutron flux was mildly affected by a change in signs adopted both in the equation and in the amplitude Coefficient terms. This meant that there was insignificant contribution made by changing of signs of TDC and ARDC and also in their respective coefficient terms. This was justified by the graphs that remained identical before and after the changes had been introduced.

In comparison, figures 4.36 (i), (ii) and (iii) possesses similar findings as those in figure 4.33, 4.34 and 4.35.

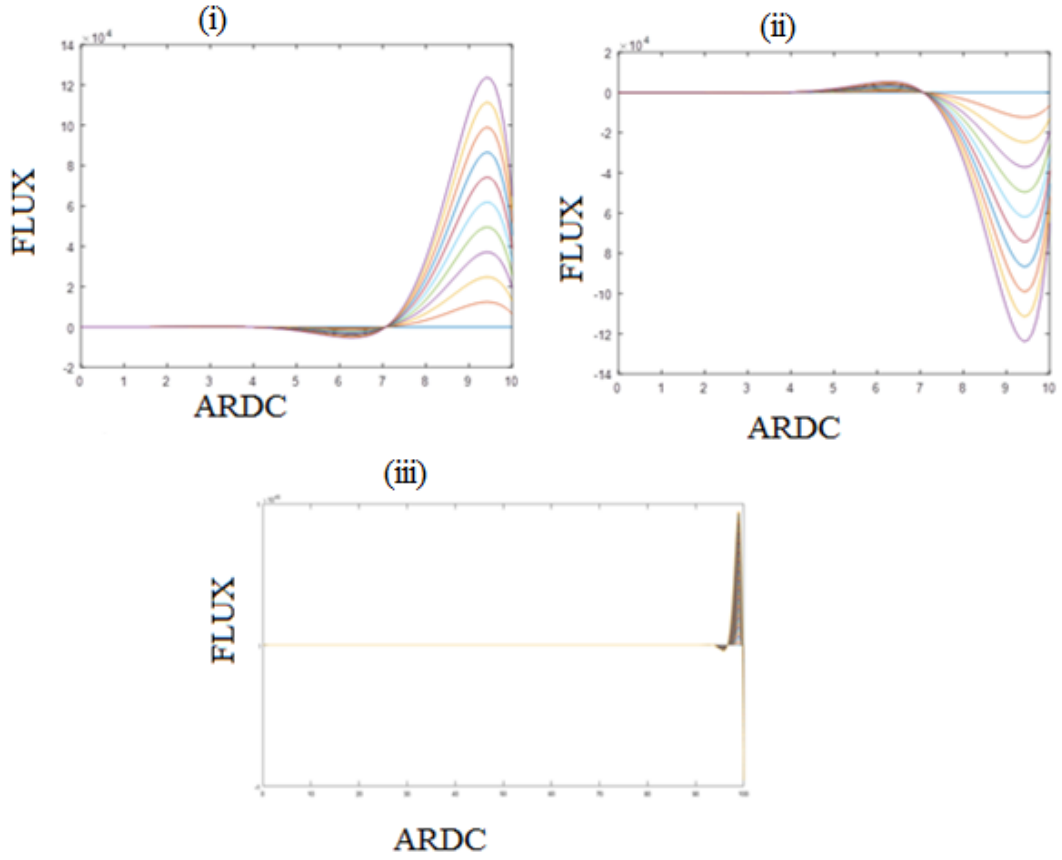

Figure 4. 36: A 2-dimensional figure generated using Analytic method
(Plotted using conditions in Table 4.19 and Table 4.20)

The results generally depicted the formation of a 2-dimensional plots showing neutron flux with two distinct points. In essence, the flux at higher ARDC had two points of inflections. The first inflection appeared smaller than the second inflection for all the graphs. Fig 4.36 (ii) appeared to be inversion of graph Fig 4.36 (i) arising as a result of the change of exponent sign of the wave function. In the study by Cai and Kittelmann (2020) predicted this kind of behavior whereby flux contours were near spherical near the source but develop into spheroid geometry with increasing semi focal distance. Thus, the study confirmed that the

diffusion of neutrons along the focal semi distance (Cai & Kittelmann, 2020) and along axis ratio was related.

Furthermore, when the initial conditions were varied so that TDC and ARDC lower boundary set as L (0, 0) the upper boundary at U (10, 10), the TDC and ARDC were both set with an interval of 0.1. An amplitude term $G(\eta,\xi) = -a + bi$ was adopted with amplitude limits set at L (0, 0) and U (10, 10) and both with an interval of unity. The function;$\psi(g_{1,}g_2) = G(g_{1,}g_2)e^{g_1+g_2 i}$was adopted resulting in the formation of the Figure 4.37.

Table 4. 20: Boundary conditions set 21

	Lower Boundary	Upper Boundary	Interval
TDC ($\sim g_1$)	0	10	0.1
ARDC ($\sim g_2$)	0	10	0.1
a	0	10	1
b	0	10	1

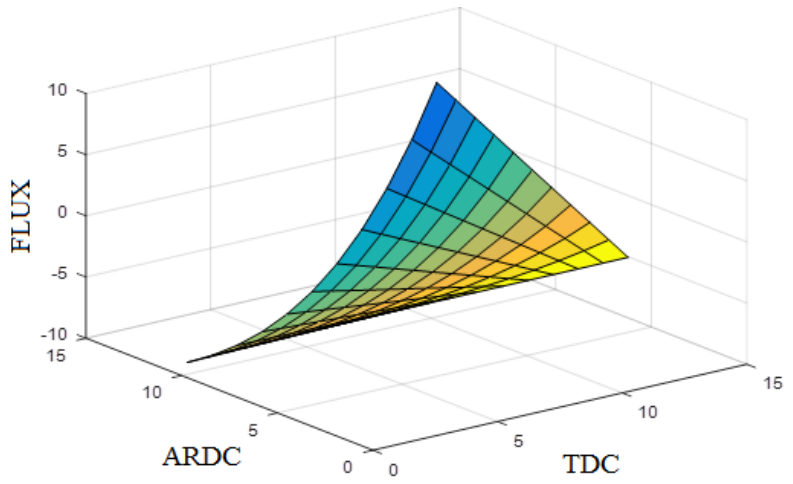

Figure 4. 37: A hyperbolic paraboloid surface generated using Analytic method

(Plotted using conditions in Table 4.21).

The ternary surface showed neutrons flux in a twisted rectangular topological surface. As ARDC progressed from 0 towards 15, the flux decreased from maximum (10) to minimum (-10). At ARDC = 10, it was found that the flux had covered the widest spatial surface. This graph illustrated indeed another form of a hyperbolic parabolic surface

In addition, the study focused on ternary surfaces that was produced when TDC and the ARDC lower boundaries were set L, (-1, -1), the upper boundary U (1, 1), with a common interval of 0.01 adopted. The amplitude terms,$G(\eta,\xi) = -a + bi$ were set at L (0, 0) and U (100,100) and both with an interval of unity. The function $\psi(g_{1,}g_2) = G(g_{1,}g_2)e^{-g_1+g_2 i}$ was applied resulting in the formation of Fig 4.38.

Table 4.21: Boundary conditions set 22

	Lower Boundary	Upper Boundary	Interval
TDC ($\sim g_1$)	-1	1	0.01
ARDC ($\sim g_2$)	-1	1	0.01
a	0	100	1
b	0	100	1

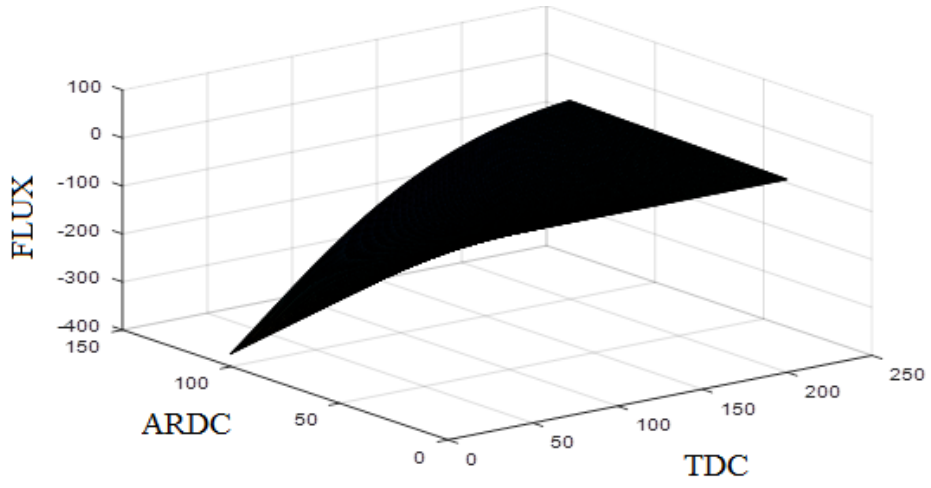

Figure 4. 38: A Parabolic cylindrical surface generated using Analytic method
(Plotted using conditions in Table 4.21).

A characteristic ternary surface with a triangular surface curvature was obtained as shown in Figure 4.38 upon applying conditions table 4.22 on the diffusion equation. It characterized flux spreading from a point source to cover a wider spatial area as TDC increased from 0 to 250. Secondly, it was evident that as ARDC progressed from 0 towards 150, the flux similarly covered a triangular surface that was symmetric at about ARDC=100. It was observed that the diffusion behavior under these conditions was indeed a parabolic surface diffusion configuration.

Similar studies to Figure 4.37- 4.38 were found in the study highlighted in (Welch et al., 2017). This study indeed confirmed the formation of ternary surfaces as shown in Fig 4.22b. The study was an investigation of multi-group neutron diffusion flux n spheroids using a manufactured solution.

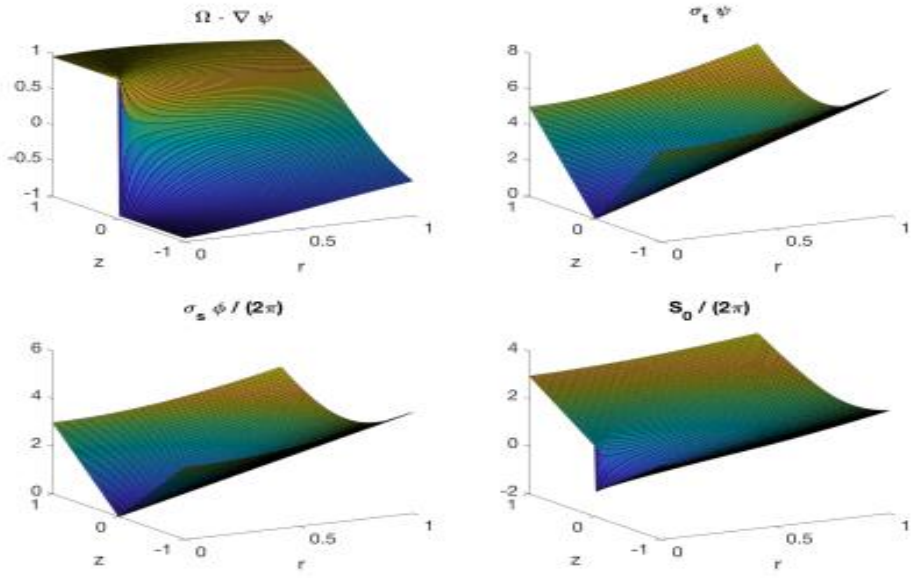

Figure 4. 39: Analytic graphs using various neutron sources using manufactured solution

(Shqair, 2019)

4.3.4 Summary of findings using Analytic method.

Using analytical method, it was shown that for real component and zero complex components, the diffusion exhibited mostly ternary surfaces. As the real component went to zero and the imaginary component became dominant, the surfaces became discontinuous periodic surfaces similar to those observed using Jacobi elliptic theta functions. Lastly, as both imaginary and real component became dominant, the diffusion surfaces were largely ternary surfaces such as elliptic paraboloids, hyperbolic paraboloids and cylindrical paraboloids. The findings were also corroborated by similar studies such as the one mentioned in (Woods & Palmer, 2017)

4.4 Comparison Between Analytic and Jacobi Elliptic Theta Behaviors

The two methods of Jacobi elliptic theta function and analytic method were adopted in this study with the former as the main technique. Intriguingly it emerged that the two methods presented similar findings in ternary surfaces that characterize neutron diffusion problem.

The existence of hyperbolic paraboloid surfaces, continuous periodic surfaces, and elliptic parabolic surfaces reinforced a major similarity between the surfaces. Figure 4.40 shows a one to comparison in the behavior of diffusion distinguished between the two methods.

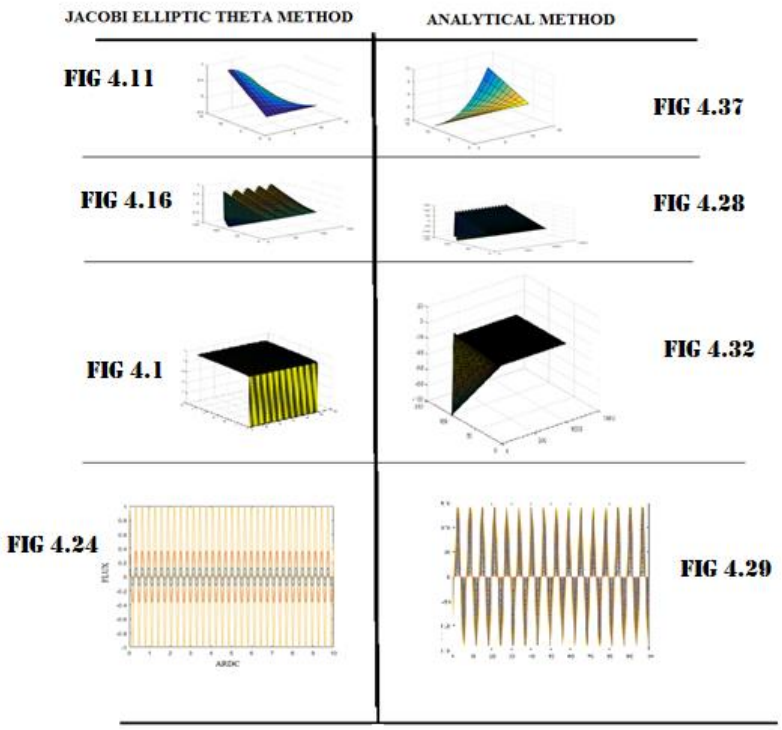

Figure 4.40: A comparative graph showing the graphs obtained using Analytical and Jacobi elliptic theta function

One major difference was that more configurations were obtained using Jacobi elliptic theta function than analytic method under similar conditions. Jacobi elliptic theta method gave a wider number of these configurations enabled neutron diffusion problems in spheroids to be visualized better.

Furthermore, the variation of 'n' in the Jacobi elliptic theta method provided a simplified method of dealing with eigen-value problems that were encountered in similar problems in the past. Jacobi elliptic theta method thus provided a more realistic analysis for understanding the behavior of neutron diffusion in spheroids than analytic methods.

4.5 Behavior of Neutron Leakage in Spheroids

The behavior of neutron leakage rate was considered by plotting the function; $L = \left[\frac{kc^2}{9.86+19.72c^2}\right]^{\frac{1}{2}}$ for prolate and $L = \left[\frac{kc^2}{19.72+9.86c^2}\right]^{\frac{1}{2}}$ for oblate in the range of ARC (0,

10) at an interval of 0.01. The values of k were set at k (0, 10, 100, 500, 1000). The results for neutron leakage rate in the oblate spheroid was shown in Fig 4.41 (i), that of the prolate spheroid was shown in Fig 4.42 (ii) and lastly, that of combined i.e prolate and oblate was presented in Fig 4.41.

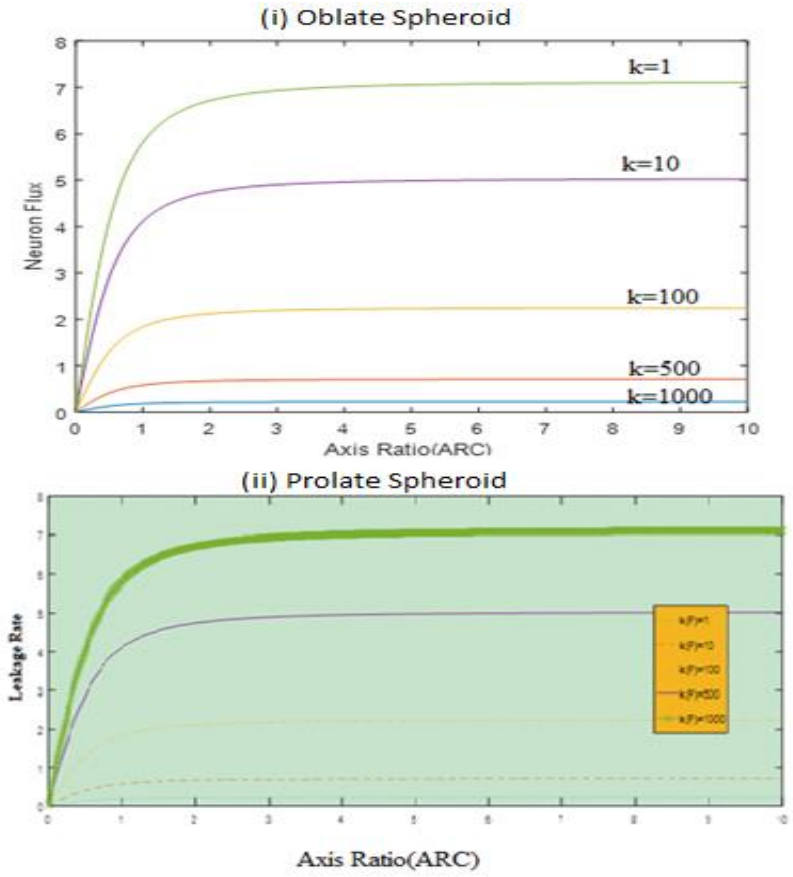

Figure 4. 41: Neutron Leakage rates versus Axis ratio, Oblate (i) and Prolate (ii)

From the results, it was evident that the neutron leakage rate was mildly affected by the changes in the axis ratio for both spheroids at large axis ratios, however, oblate spheroids tended to exhibit relatively higher neutron leakage rate at smaller axis ratios compared to prolate spheroids of the same volume. The probable explanation was that at smaller axis ratios, an oblate spheroid had a larger surface area compared to a prolate of a similar volume.

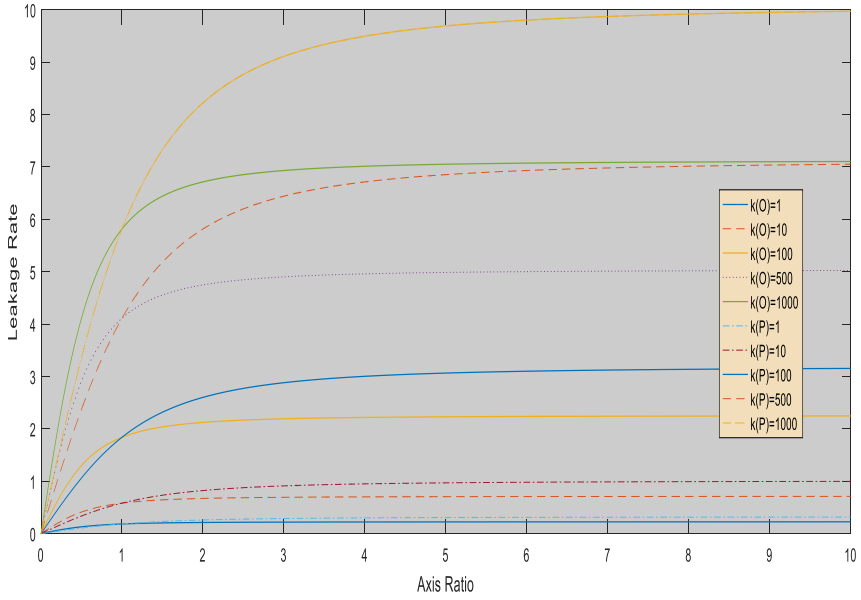

Figure 4. 42: Neutron Leakage rates versus Axis ratio for oblate and prolate spheroid

Generally, each of the graphs could be divided into two sections; the first section for axis ratio between 0 and 1(Refer to Figure 4.42). In this section, the neutron leakage rate for the oblate Spheroid appeared higher than that of prolate spheroid of the same volume at any given value of k.This observation was explained as follows; at small axis ratios, the surface area of an oblate spheroid was much larger than the surface area of a prolate spheroid with the same volume (Hannaske et al., 2013).

Secondly, it was observed that when the axis ratio was unity, the neutron leakage rate for the oblate spheroid and prolate spheroid converges since all values of this point represent the special case of sphere. In addition, it was found that at large axis ratio; there was little dependence of the neutron leakage rate on the axis ratio of the spheroid. This was possibly because at such axis ratios, the probability of neutrons with large energy values reaching the surface of the reactor core may

have been significantly reduced, consequently, the probability of neutron leakage was also reduced.

Thirdly as the axis ratio became greater than unity, the neutron leakage rate for prolate spheroid overtook that of oblate spheroid because the surface area of the Prolate spheroid became larger than that of Oblate spheroids of the same volume.

Lastly, it was found that at large value of (k) e.g. k > 1000, the neutron leakage rate for both prolate and oblate spheroids almost superimposed. This was because for large neutron leakage constant, k, the other terms in equations (3.10) and (3.13) tended to converge for both Oblate and Prolate spheroids respectively.

A possible application of this concept would be in the design of reactors whose reaction rates could be altered by simply by varying the axis ratios of the core. Such reactors would be able to mitigate the effects of adverse events like earthquakes. Finally, it was observed that the findings in this work were in agreement with the findings made in the study of heat diffusion in spheroids (Plompen et al., 2020)

4.6 Reactor Core Criticality Behavior under varying axis Ratio

The relationship between axis ratio and reactor core reactivity was formulated in equation , $\rho = 1 - \frac{19.72+(9.86+\beta^2)c^2}{(19.72+9.86c^2)\Omega}$, for oblate spheroid and equation , $\rho = 1 - \frac{9.86+(19.72+\beta^2)c^2}{(9.86+19.72c^2)\Omega}$, for prolate spheroids. In these two equations, two terms were introduced Ω (average neutron per fission) and β was defined by equation $\beta = kB^2$. The relationships were used to explain the behavior of reactivity versus axis ratio.

To start with, the equation; $\rho = 1 - \frac{19.72+(9.86+\beta^2)c^2}{(19.72+9.86c^2)\Omega}$, with the value of Ω = 5 and β (0.1,0.5,1,2.5,5) was adopted in the range of ARDC (0,5) with an interval of 0.01, the Fig 4.43 was generated

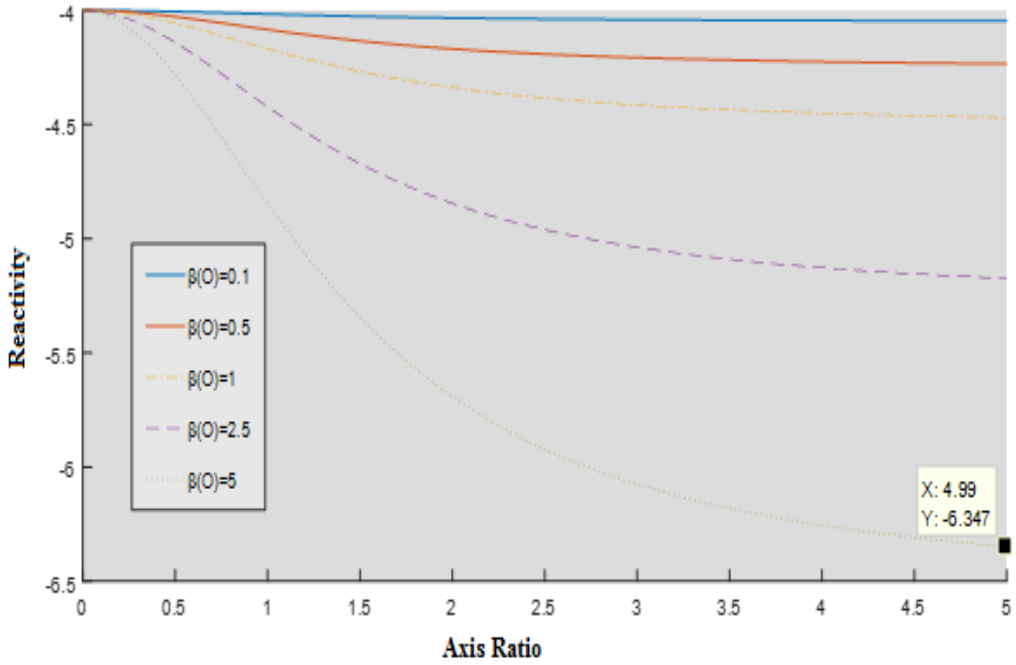

Figure 4.43: Reactor core criticality versus axis ratio for oblate spheroid

It was observed that as ARDC increased from 0 to 5, the core reactivity decreased exponentially from -4 to lower values dependent on the value of β (Figure 4.43). For instance, for β (0.5), ARDC was - 6.347 at axis ratio equal to 4.99. It was further established that smaller β values caused the reactor reactivity to decay faster than larger β values. Furthermore, it was evident that smaller β values almost produced linear graphs signifying that the reactor core reactivity was least affected by such β values.

For a prolate spheroid, the equation; $\rho = 1 - \frac{9.86+(19.72+\beta^2)c^2}{(9.86+19.72c^2)\Omega}$, with the value of Ω =5 and β (0.1, 0.5,1,2.5,5) were adopted in the range of ARDC (0,5) with an interval of 0.01, the Fig 4.44 was obtained.

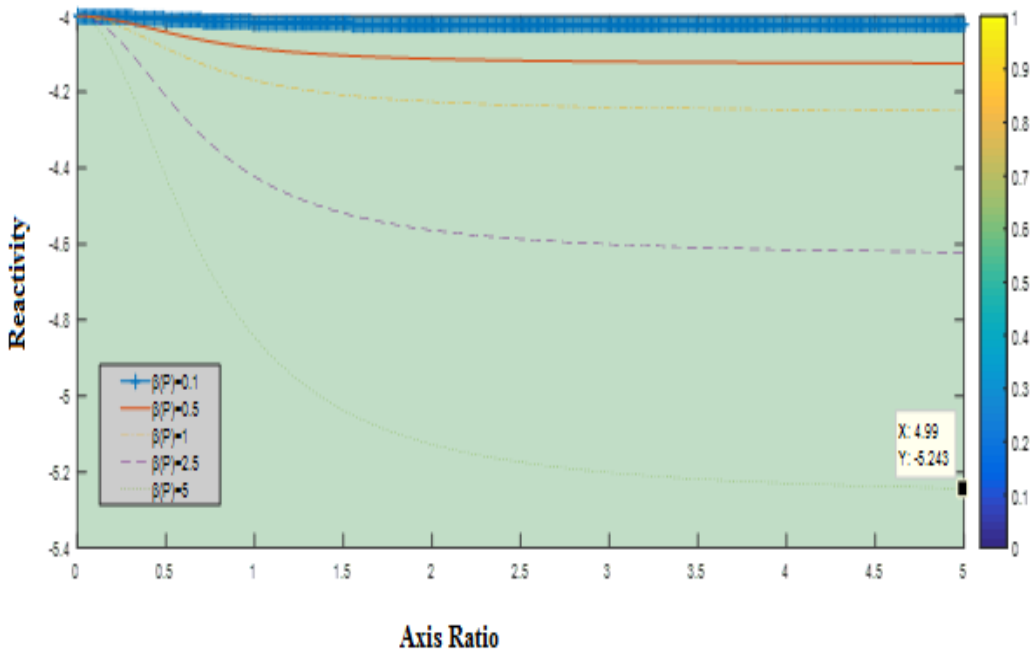

Figure 4. 44: Reactor core criticality versus Axis ratio for prolate spheroid

Resonating results for Figure 4.43 and Figure 4.44 were observed. In particular, as ARDC increased from 0 to 5, it was noted that the reactor core reactivity decreased exponentially from - 4 to lower values depending on the values of β. In particular, smaller β values were linked to hasten reactor reactivity than larger β values. In addition, smaller β values almost produced linear graphs implying that the reactivity was least affected at such values

Comparing the results presented by Figure 4.26 with that of Figure 4.25, it was established that the reactor criticality decayed to comparatively smaller values for similar ARDC values. It was also shown that higher ARDC values affected reactor core reactivity more than smaller values.

Secondly, when the equation, $\rho = 1 - \frac{19.72+(9.86+\beta^2)c^2}{(19.72+9.86c^2)\Omega}$, and $\rho = 1 - \frac{9.86+(19.72+\beta^2)c^2}{(9.86+19.72c^2)\Omega}$, were combined while the value of Ω =5 and β (0.1,0.5,1,2.5,5) were adopted in the range of ARDC (0,5) with an interval of 0.01, the Figure 4.45 was developed.

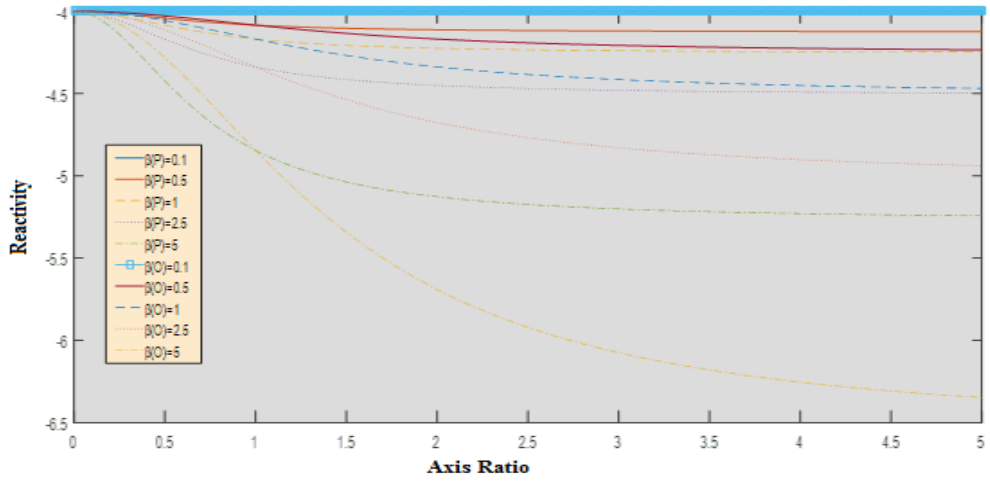

Figure 4. 45: Reactor core criticality versus Axis ratio for prolate and oblate spheroid at Ω=5

The outlying differences between the reactor core criticality for an oblate and prolate spheroid clearly displayed (Figure 4.45). First it was shown that for ARDC values less than unity, prolates portrayed lower reactor core criticality values compared to oblates of the same volume. Secondly it was emerged that at ARDC=1, the reactor core reactivity for both prolate and oblate spheroid coincided. Lastly, as the ARDC values became greater than unity, the reactor core reactivity for prolate became greater than that of oblate spheroid of the same volume.

Thirdly, when the equation; $\rho = 1 - \frac{9.86+(19.72+\beta^2)c^2}{(9.86+19.72c^2)\Omega}$, and $\rho = 1 - \frac{19.72+(9.86+\beta^2)c^2}{(19.72+9.86c^2)\Omega}$ were adopted while the value of β maintained at β =5 and Ω values (Ω = 0,0.5,1,2,5) adopted in the range of ARDC (0,5) with an interval of 0.01, the Figure 4.46 was arrived at.

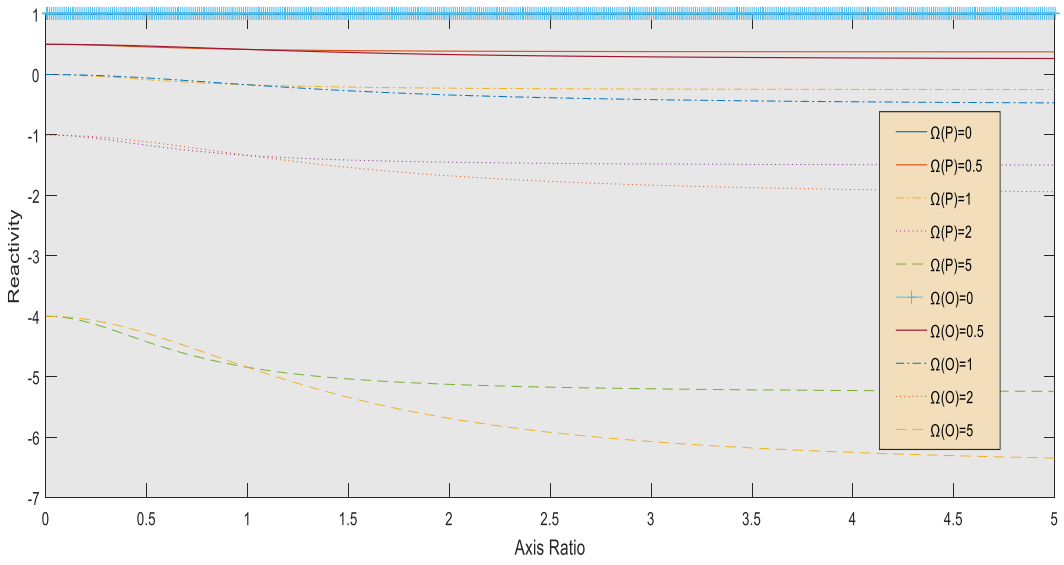

Figure 4. 46: A Combined Graph showing the reactor core criticality versus Axis ratio for prolate and oblate spheroid at β = 5

Although similar findings were found in Figure 4.46 compared to Figure 4.45, a divergent observation was observed. Whenever the value of β was kept constant but that of, **Ω** varied, there was dispersion of curves from the origin into distinct values determined by the initial reactor core reactivity.

Lastly, when the equation; $\rho = 1 - \frac{9.86+(19.72+\beta^2)c^2}{(9.86+19.72c^2)\Omega}$, and $= 1 - \frac{19.72+(9.86+\beta^2)c^2}{(19.72+9.86c^2)\Omega}$, were applied with the value of β = 10 and **Ω** (0,0.5,1,2,5) adopted in the range of ARDC (0,5) with an interval of 0.01, the Figure 4.47 was generated.

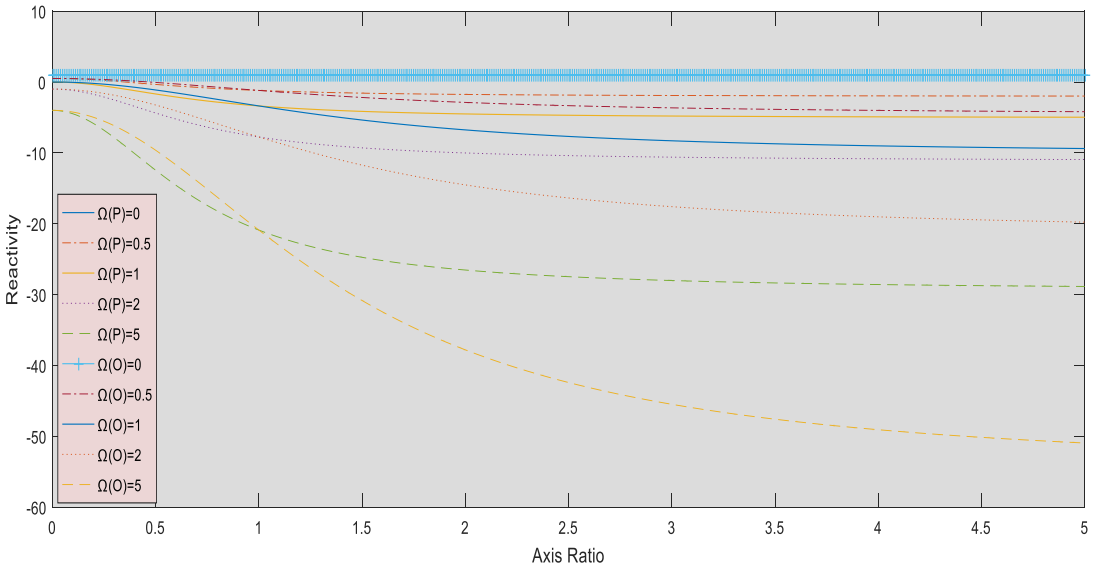

Figure 4. 47: A Combined graph showing the reactor core criticality versus Axis ratio for prolate and oblate spheroid at β=10

From the Figure 4.47, similar findings were found compared to Figure 4.46 and 4.45, however, it was established that when the value of β was kept constant but that of **Ω** varied as stated, there was not only the dispersion of curves into separate initial values of reactor core reactivity but also an observed increase in the gradient between ARDC (0-5).

4.7 Summary of Key Findings

In summary, it was observed that for values of 'n' less than unity, the diffusion surface generated was largely influenced by the other conditions of the equation 3.68. These conditions were mostly related to the values of ARDC and TDC. The interval between the values was shown to influence the smoothness of the surface while the amplitude was shown not to affect the surface type generated but only influenced the rate at which the flux reached its maximum. For instance, at 'n'= 0.1, the results produced both ternary surface and continuous periodic functions. At 'n'= 0.5, periodic functions with sharp peak was witnessed. As 'n' was further

reduced to 0.01, complex surfaces were generated that was characterized by multiple surfaces on different planes.

The nature of diffusion surfaces obtained when ‘n’=1 were mostly continuous periodic surface with tapering ends. Smaller intervals between ARDC and TDC were found to enhance the smoothness of the diffusion surface. The diffusion surfaces were mostly parabolic hyperboloids and asymmetrical continuous 3-dimensional surfaces with tapering ends. The later was attributed to the attenuation of the waves as they propagate through the spheroid core.

As the value of ‘n’ became greater than unity, it was shown that the waves changed from ternary surfaces to continuous and discontinues 3-dimensional surfaces. It was further observed that as the value of ‘n’ was increased progressively, the peak of the waves of the surfaces became smoother and uniform. This pointed to the saturation of the flux as explained by (Woods & Palmer, 2017)

Using analytical method, it was shown that for real component and zero complex components, the diffusion surfaces were mostly ternary surfaces. As the real component became zero and the imaginary component became dominant, the surfaces became discontinuous periodic surfaces similar to those observed using Jacobi elliptic theta functions. Lastly, as both imaginary and real component became dominant, the diffusion surfaces were largely ternary surfaces such as elliptic paraboloids, hyperbolic paraboloids and cylindrical paraboloids.

Concerning neutron leakage rates, it was evident that the axis ratio for both spheroids at large axis ratios than at smaller axis ratio. The neutron leakage rate for the oblate Spheroid has been found was always higher than that of prolate spheroid at any given value of α. Subsequently, as the axis ratio became greater

than unity, the neutron leakage rate for prolate spheroid overtakes that of oblate spheroid because the surface area of the prolate spheroid became larger than that of oblate spheroids of the same volume. At axis ratio of unity, the neutron leakage rate for the oblate spheroid and prolate spheroid converges since all values of this point represent the special case of sphere. Furthermore, large axis ratio, there was little dependence of the neutron leakage rate on the axis ratio of the spheroid. Lastly, it was found that at large value of (k) e.g. **k** > 1000, the neutron leakage rate for both Prolate and Oblate spheroids almost superimpose. This was because for large neutron leakage constant, k, the other terms in equations (3.10) and (3.13) tend to converge for both Oblate and Prolate spheroids respectively.

The relationship between reactor criticality and the axis ratio was investigated. It was established that smaller ß values caused the reactor reactivity to decay faster than larger ß values. It was evident that smaller ß values almost produced linear graphs signifying that the reactor core reactivity was least affected by such ß values.

It was shown that for ARDC values less than unity, prolate exhibited lower reactor core criticality values compared to oblates. Secondly it was shown that at ARDC=1, the reactor core reactivity for both prolate and oblate spheroid coincided. Thirdly, as the ARDC values became greater than unity, the reactor core reactivity for Prolate became greater than that of oblate spheroid of the same volume. Although similar findings were found compared to Figure 4.42, it was established that when the value of ß was kept constant but that of, **Ω** varied as stated, there was separation of curves into separate initial values of reactor core reactivity.

CHAPTER FIVE

CONCLUSIONS

5.1 Introduction

Fick's neutron diffusion equation has been transformed analytically into a new neutron diffusion formula. Thereafter, it was modified into a new Jacobi elliptic function, subjected to appropriate Boundary Conditions and the results generated and analyzed using Python software. The results were later compared with similar models in other studies. The current study confirms previous findings and contributes to our understanding of the role of axis ratio in influencing the flux, leakage rates and reactor core reactivity.

It was found that the magnitude of the wave amplitude, value of '**n**' and quantities of the variables ARDC and TDC were critical in influencing the type of diffusion surface obtained. Generally, some of the diffusion surfaces obtained include; hyperboloid paraboloid, cylindrical and parabolic surfaces. There was also the formation of waves that included; continuous periodic 3 - dimensional waves among others. Some earlier findings were confirmed by the study that include; saturation of waves at higher order polynomials, for instance, a**s** the value of '**n**' was increased to higher values such as, '**n'** > 5**.** When smaller intervals between TDC and ARDC were adopted, it was found that surfaces were relatively smoother than when larger intervals were adopted. waves were found to undergo rapid oscillation at higher ARDC values and damping for smaller ARDC values; spherical to spheroid behaviour of flux contours with increasing axis ratios, flux contours were formed that are near-spherical near the source but develop into spheroid geometry at increasing axis ratio. Although, the results obtained using both the analytic and Jacobi elliptic theta methods were largely in agreement, it

was established that the later provided a quicker and a more simplified method of visualising the neutron flux in spheroids compared to the former.

The study was also aimed at understanding the effects of variation of axis ratio on neutron leakage rate. This was executed for axis ratios less than unity, equal to unity and greater than unity. First, for axis ratios less than unity, the neutron leakage rate for an oblate spheroid was established to be relatively higher than that of prolate of equal volume. In addition, it was found that the neutron leakage rate is mildly affected at relatively large axis ratios than at smaller axis ratio for both prolate and oblate spheroids. Secondly, for larger values of axis ratio, the converse is true, this is because at large axis ratios, the surface area of the prolate became larger than that of oblate of the same volume. Thirdly, at axis ratio equal to unity, the neutron leakage rate for the oblate and prolate converges since all values of this point represent the special case of a sphere. In addition, at large values of neutron leakage constant term**,** **k**, for instance, **k** >1000, the neutron leakage rate for both Prolate and oblate spheroids almost superimpose. This shows that large neutron leakage constant terms tend to dominate the formulated leakage equation.

Furthermore the study has added to the body of knowledge about the understanding of reactor core reactivity. In particular, three main variables i.e. ß, **Ω** and axis ratio were found to affect the reactor core reactivity. First, it was noted that smaller ß values induced decay faster than larger ß values and was mildly affected by relatively smaller ß values. Secondly**,** it was established that when the value of ß was kept constant but that of, **Ω** varied, there was the segregation of curves into various reactor core reactivity values at the origin. Thirdly, it was found that for axis ratios less than unity, Prolate exhibited lower reactor core reactivity values

compared to oblates of the same volume. At axis ratio equal to unity, the reactor core reactivity for both Prolate and oblate spheroid were observed to nearly superpose. Also, as the axis ratio became greater than unity, the reactor core reactivity for Prolate became greater than that of the oblate spheroid of the same volume.

The findings in this study will useful in the enhancement of reactor cores designs that for the attainment of robust, safe and economical designs. Furthermore, it will widen the existing understanding on the behaviour of reactor cores occurring due to deformation by extreme events that are bound to alter the axis ratio of the spheroid.

5.2 Recommendations

The model has been used to study diffusion of thermal neutrons. Similar work may be extended to study multi-group diffusion problem. Secondly there is need to differentiate the flux behaviour for each type of spheroid (oblate and prolate) separately using a similar model. Furthermore, Flux, Leakage rates and Reactivity for similar models with reflective walls need to be carried out.

REFERENCES

Agency, I. A. E. (2015). *The Fukushima Daiichi Accident*. IAEA.

Al Zain, J., El Hajjaji, O., El Bardouni, T., Boukhal, H., & Jaï, O. (2018). Validation of DRAGON4/DONJON4 simulation methodology for a typical MNSR by calculating reactivity feedback coefficient and neutron flux. *Results in Physics*, *9*, 1155-1160.

Alassar, R. (1999). Heat conduction from spheroids. *ASME Journal of Heat transfer*, Vol 121,pp 498-499.-21

Alassar, R., Abushosha, M., & El-Gebeily, M. (2014). Transient heat conduction from spheroids. *Transactions of the Canadian Society for Mechanical Engineering*, *38*(3), 373-389.

Amano, Y. (2011). Radiation protection and safety of radiation sources: International basic safety standards. .IAEA,Geneva

Apostol, T., Olver, F., Lozier, D., Boisvert, R., & Clark, C. (2010). *NIST handbook of mathematical functions.*

Ayyoubzadeh, S. M., Vosoughi, N., & Ayyoubzadeh, S. M. (2012). On an improved Direct Discrete Method and its application in two dimensional multi-group neutron diffusion equation. *Annals of Nuclear Energy*, *44*, 1-7.

Bektas, S. (2017). Design of hyperboloid structures. *Journal of Architectural Research and Development*, *1*(2).

Blokhin, A., Zhuravlev, B., Talalaev, V., & Sipachev, I. (2015). Spectra of leakage neutrons from a Pb–Li spherical shell with central 252Cf and 14 MeV neutron sources and verification of evaluated neutron data. *Nuclear Energy and Technology*, *1*(2), 122-125.

Cai, X.-X., & Kittelmann, T. (2020). NCrystal: A library for thermal neutron transport. *Computer Physics Communications*, *246*, 106851.

Caldicott, H. (2013). The impact of the nuclear crisis on global health. *Australian Medical Student Journal*, *4*(2).

Carayannis, E. G., Draper, J., & Iftimie, I. A. (2020). Nuclear fusion diffusion: Theory, policy, practice, and politics perspectives. *IEEE Transactions on Engineering Management*.

Carmo, J., & Lima, A. (2008). Mass transfer inside oblate spheroidal solids: modelling and simulation. *Brazilian journal of chemical engineering*, *25*(1), 19-26.

Cohen, E., Hen, O., Piasetzky, E., Weinstein, L., Duer, M., Schmidt, A., . . . Akbar, Z. (2018). Center of Mass Motion of Short-Range Correlated Nucleon Pairs studied via the A (e, e′ p p) Reaction. *Physical Review Letters*, *121*(9), 092501.

Falloon, P. E., Abbott, P., & Wang, J. (2003). Theory and computation of spheroidal wavefunctions. *Journal of Physics A: Mathematical and General*, *36*(20), 5477.

Findlay, T. (2010a). The future of nuclear energy to 2030 and its implications for safety, security and nonproliferation. Center for International Governance Innovation, Ontario, Canada.

Findlay, T. (2010b). Part 1–The Future of Nuclear Energy to 2030. *Waterloo: The Centre for International Governance Innovation (CIGI)*.

Goldberg, S., & Rosner, R. (2011). *Nuclear reactors: Generation to generation*. .American Academy of Sciences, USA

Hannaske, R., Elekes, Z.,Kögler, T. (2013). Neutron total cross section measurements of gold and tantalum at the nELBE photoneutron source. *The European Physical Journal A*, *49*(11), 1-11.

Ho, S. (2020). *Introduction to Monte Carlo*. Springer Press services.Institut Polytechnique de Paris Palaiseau Cedex, France

Ivers, D. (2004). An angular spectral method for solution of the heat equation in spheroidal geometries. *ANZIAM Journal*, *46*, C854-C870.

Jeffrey, F. (2007). Plasma physics and fusion energy. *Massachusetts Institute of Technology*.

Kim, D.-S., & Kim, Y. H. (2013). Some characterizations of spheres and elliptic paraboloids II. *Linear algebra and its applications*, *438*(3), 1356-1364.

King, L. V. (1924). *On the direct numerical calculation of elliptic functions and integrals*. The University Press.

Lamarsh, J. R., & Baratta, A. J. (2001). *Introduction to nuclear engineering* (Vol. 3). Prentice hall Upper Saddle River, NJ.

Li, L.-W., Kang, X.-K., & Leong, M.-S. (2004). *Spheroidal wave functions in electromagnetic theory*. John Wiley & Sons.

Lima, D., Farias, S., & Lima, A. (2004). Mass transport in spheroids using the Galerkin method. *Brazilian journal of chemical engineering*, *21*(4), 667-680.

Linde, S. (1960). *The multigroup neutron diffusion equations/1 space dimension*. AB Atomenergi, Stockholm (Sweden)

Masterson, R. E. (2017). *Nuclear Engineering Fundamentals: a practical perspective*. CRC Press.

Murray, R., & Holbert, K. E. (2014). *Nuclear energy: an introduction to the concepts, systems, and applications of nuclear processes*. Elsevier.

Murty, K. L., & Charit, I. (2013). *An introduction to nuclear materials: fundamentals and applications*. John Wiley & Sons.

Ongena, J. (2016). Nuclear fusion and its large potential for the future world energy supply. *Nukleonika*, *61*(4), 425-432.

Patra, P., Das, D., & Dash, R. B. (2018). A comparative study of Gauss–Laguerre quadrature and an open type mixed quadrature by evaluating some improper integrals. *Turkish Journal of Mathematics*, *42*(1), 293-306.

Petrov, Y. V., Nazarov, A., Onegin, M., Petrov, V. Y., & Sakhnovsky, E. (2006). Natural nuclear reactor at Oklo and variation of fundamental constants: Computation of neutronics of a fresh core. *Physical Review C*, *74*(6), 064610.

IAEA. Safety of radioacticve waste disposal.Proceedings of an Internal conference Tokyo, 3 - 7 October 2005. *International Atomic Energy Agency*, Vienna

Plompen, A. J., Cabellos, O., De Saint Jean, C., Fleming, M., Algora, A., Angelone, M., . . . Blokhin, A. (2020). The joint evaluated fission and fusion nuclear data library, JEFF-3.3. *The European Physical Journal A*, *56*(7), 1-108.

Prasolov, V. V. e., & Solov_ev, I. U. P. (1997). *Elliptic functions and elliptic integrals* (Vol. 170). American Mathematical Soc.

Qvist, S., & Greenspan, E. (2012). Inherent Safety of Minimum Burnup Breed-and-Burn Reactors. Proc. Int. Congress Advances in Nuclear Power Plants (ICAPP'12),

Ragheb, M. (2006). Two Group Diffusion Theory for Bare and Reflected Reactors. *Lecture Notes*. University of Illnois, USA.

Ragheb, M. (2015a). Multidimensional reactor systems in diffusion theory. *Lectures given at Department of Nuclear, Plasma, and Radiological Engineering, University of Illinois*.

Ragheb, M. (2015b). Natural nuclear reactors, the Oklo phenomenon. In *Chapter 6 of Nuclear, Plasma and Radiation Science*.

Ripani, M. (2015). Energy from nuclear fission. EPJ Web of Conferences. INFN, Sezione di Genova - Genova, Italy

Röhrlich, E. (2013). Eisenhower's Atoms for Peace. The speech that inspired the creation of the IAEA. *IAEA Bulletin (Online)*, *54*(4), 3-4.

Shqair, M. (2019). Developing a new approaching technique of homotopy perturbation method to solve two-group reflected cylindrical reactor. *Results in Physics*, *12*, 1880-1887.

Shqair, M., El-Ajou, A., & Nairat, M. (2019). Analytical solution for multi-energy groups of neutron diffusion equations by a residual power series method. *Mathematics*, *7*(7), 633.

Sjoestrand, N. (1958). Calculation of the geometric buckling for reactors of various shapes. Aktiebolaget Atomenergi Stockholm, Sweden.

Sjöstrand, N., Mednis, J., & Nilsson, T. (1959). Geometric buckling measurements using the pulsed neutron source method.

Srivastava, R. K. (2020). Impacts of Sustainable Energy Resource Use on the Health of the Environment. In *Environmental Biotechnology Vol. 1* (pp. 145-180). Springer.

Van Dam, H., Van der Hagen, T., & Hoogenboom, J. (2005). Nuclear reactor physics. *Delft University of Technology, Department of Nuclear Engineering*.

Vega Carrillo, H. R. (2014). Subcritical Nuclear Assembly. Cusco, Peru

Walters, W. J., Roskoff, N. J., & Haghighat, A. (2018). The rapid fission matrix approach to reactor core criticality calculations. *Nuclear Science and Engineering*, *192*(1), 21-39.

Welch, J., Kópházi, J., Owens, A., & Eaton, M. (2017). Isogeometric analysis for the multigroup neutron diffusion equation with applications in reactor physics. *Annals of Nuclear Energy*, *101*, 465-480.

Williams, M. (1986). Neutron diffusion in spheroidal, bispherical, and toroidal systems. *Nuclear Science and Engineering*, *94*(3), 251-263.

Woods, D. N., & Palmer, T. S. (2017). Diffusion Synthetic Acceleration for High Order S {sub N} Transport on Meshes with Curved Surfaces. *Transactions of the American Nuclear Society*, *116*.

Yip, S., Yanch, J. C., & Zhu, X. (2002). 22.54 Neutron Interactions and Applications, Spring 2002.

Zelevinsky, V., & Volya, A. (2017). *Physics of Atomic Nuclei*. John Wiley & Sons.

Zeppenfeld, M. (2009). Solutions to Maxwell's equations using spheroidal coordinates. *New Journal of Physics*, *11*(7), 073007.

ANNEX I: ALGORITHMS

Annex 1: Jacobi Elliptic Theta Functions- Method

Throughout Annex 1, during the coding process, substitutions were made as follows;-

$t = \tau_q$; f = ξ; n=n; $R = \psi(\xi, \tau_q)$

1. Generation of Figure 4.5

```
>> t=[0:0.01:1];

f=[0:1:100];

n = 0.01;

R = ((t.^(n.^2))'*(exp(-f*2*i*n)));
```

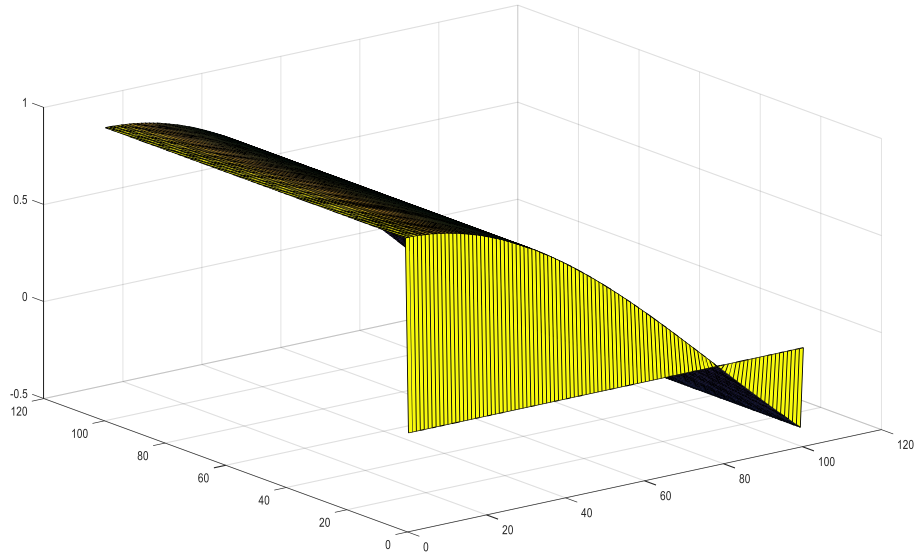

2. Generation of Figure 4.7

```
>> t=[0:0.01:1];

f=[0:1:100];

n=0.1;

R = ((t.^(n.^2))'*(exp(-f*2*i*n)));
```

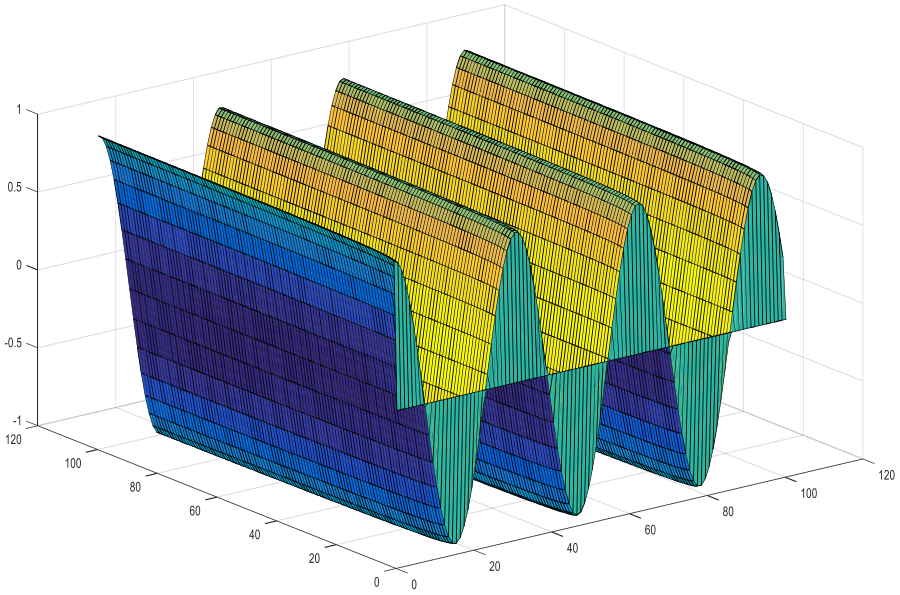

3. Generation of Figure 4.8

```
>> t=[0:0.01:1];

f=[0:1:100];

n=0.5;

R = ((t.^(n.^2))'*(exp(-f*2*i*n)));
```

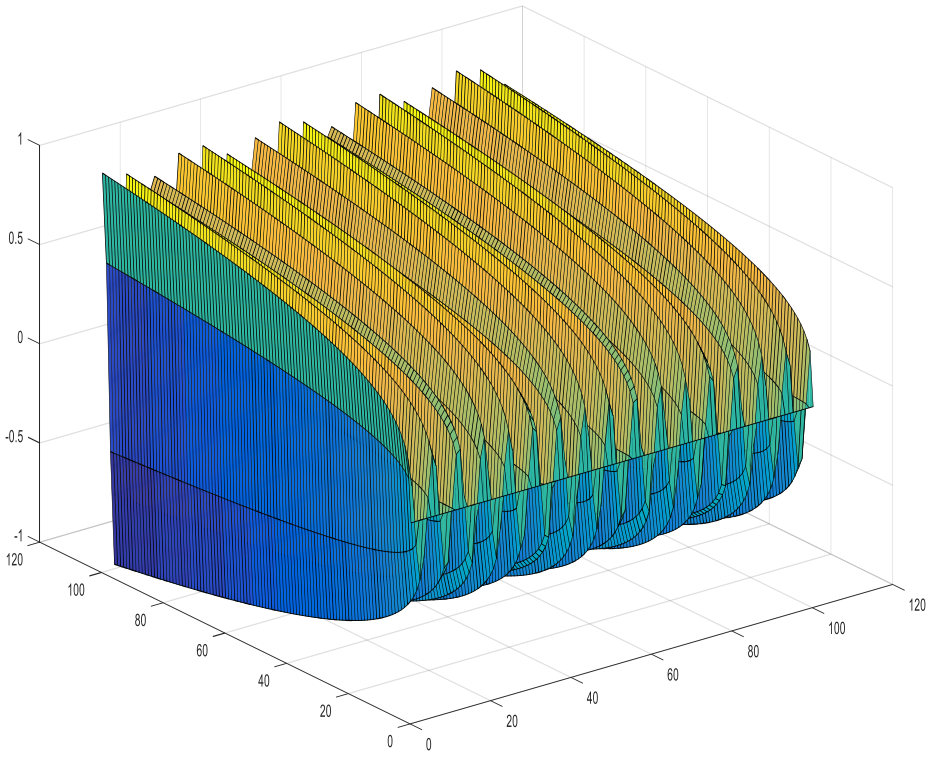

4. Generation of Figure 4.15

```
>> t=[0:0.01:1];

f=[0:1:100];

n=1;

R = ((t.^(n.^2))'*(exp(-f*2*i*n)));
```

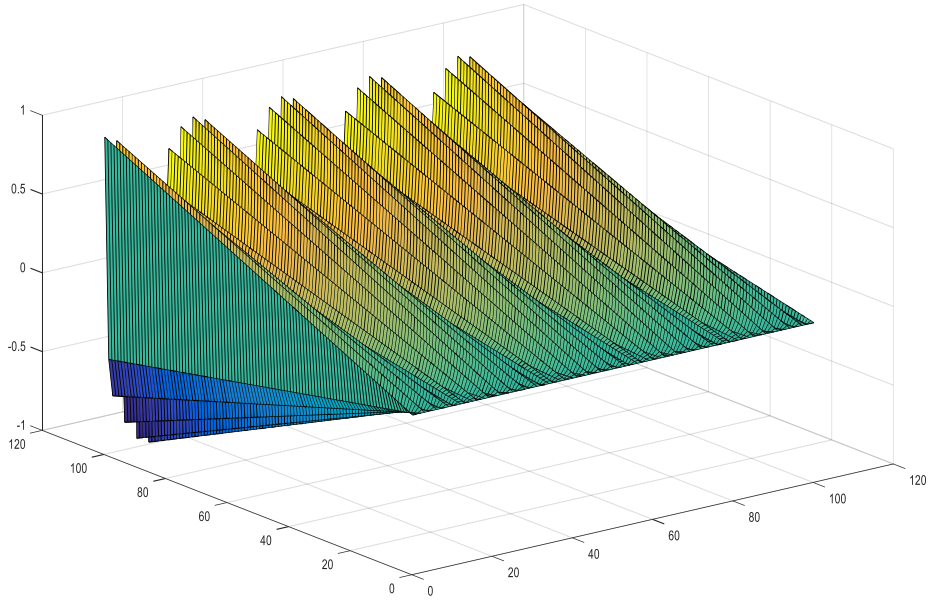

5. Generation of Figure 4.17

```
>> t=[0:0.01:1];

f=[0:1:100];

n=2;

R = ((t.^(n.^2))'*(exp(-f*2*i*n)));

surf(real(R),imag(R));
```

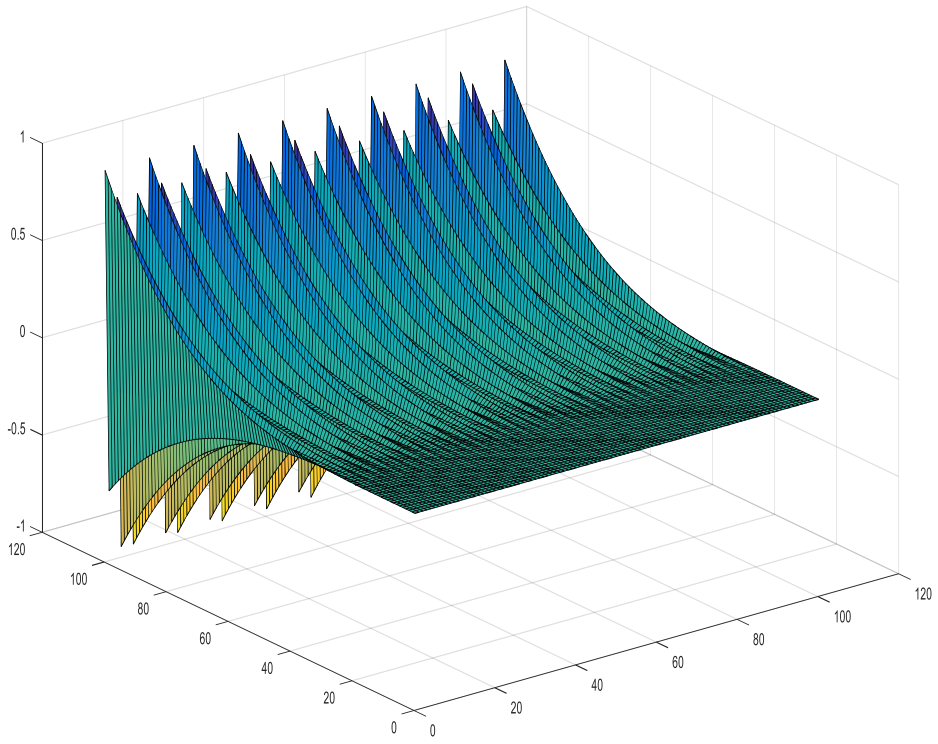

6. Generation of Figure 4.18

```
>> t=[0:0.01:1];

f=[0:0.01:1];

n=5;

R =  ((t.^(n.^2))'*(exp(-f*2*i*n)));
```

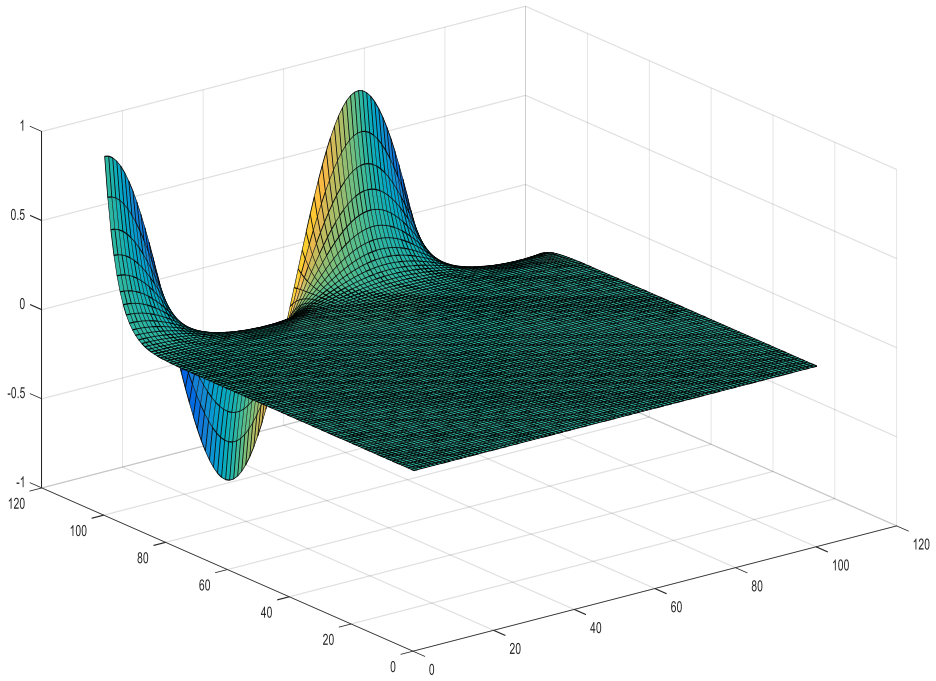

7. Generation of Figure 4.20

```
>> t=[0:0.01:1];

f=[0:1:100];

n=5;

R = ((t.^(n.^2))'*(exp(-f*2*i*n)));
```

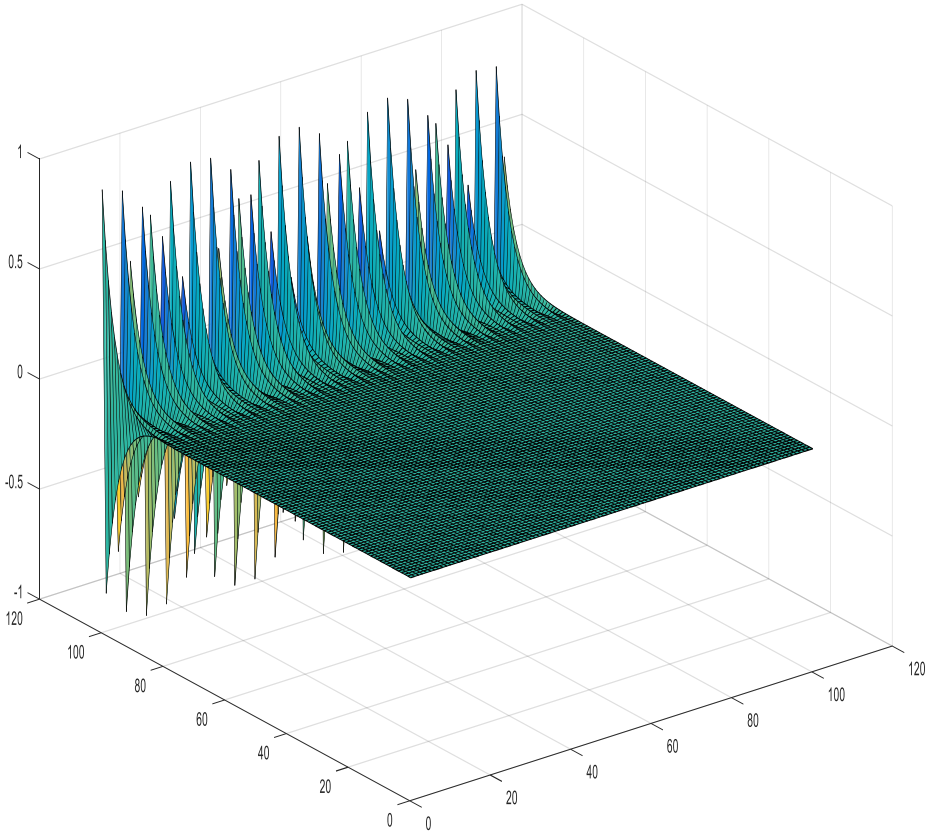

8. Generation of Figure 4.21

```
>> t=[0:0.01:1];

f=[0:1:100];

n=10;

R = ((t.^(n.^2))'*(exp(-f*2*i*n)))
```

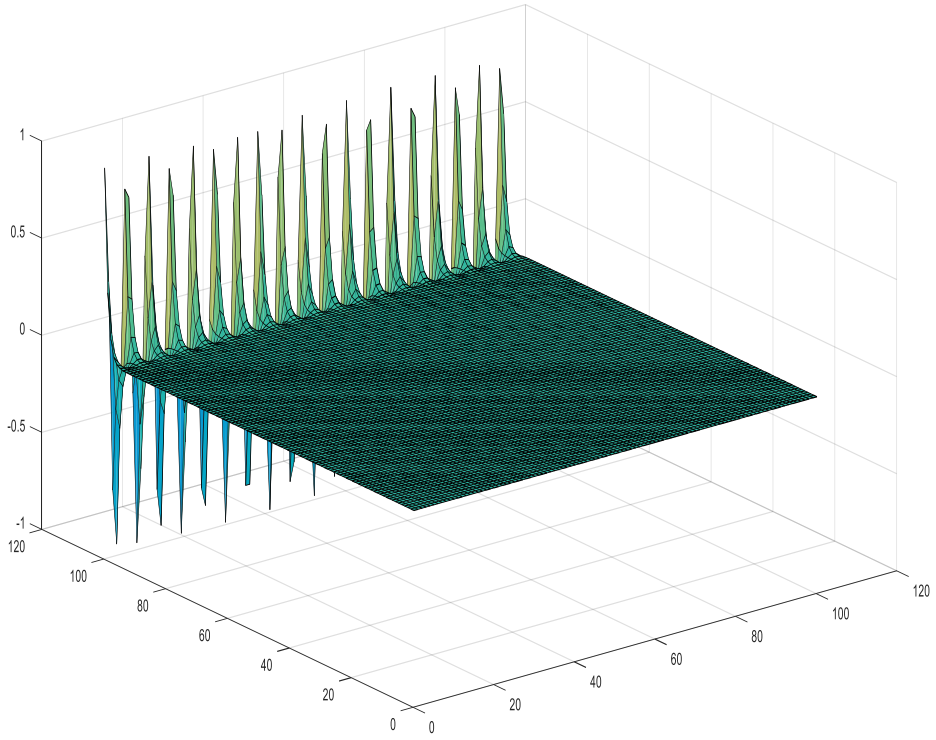

9. Generation of Figure 4.23

```
>> t= [0:0.01:1];

f= [0:1:100];

n=100;

R = ((t.^(n.^2))'*(exp(-f*2*i*n)));
```

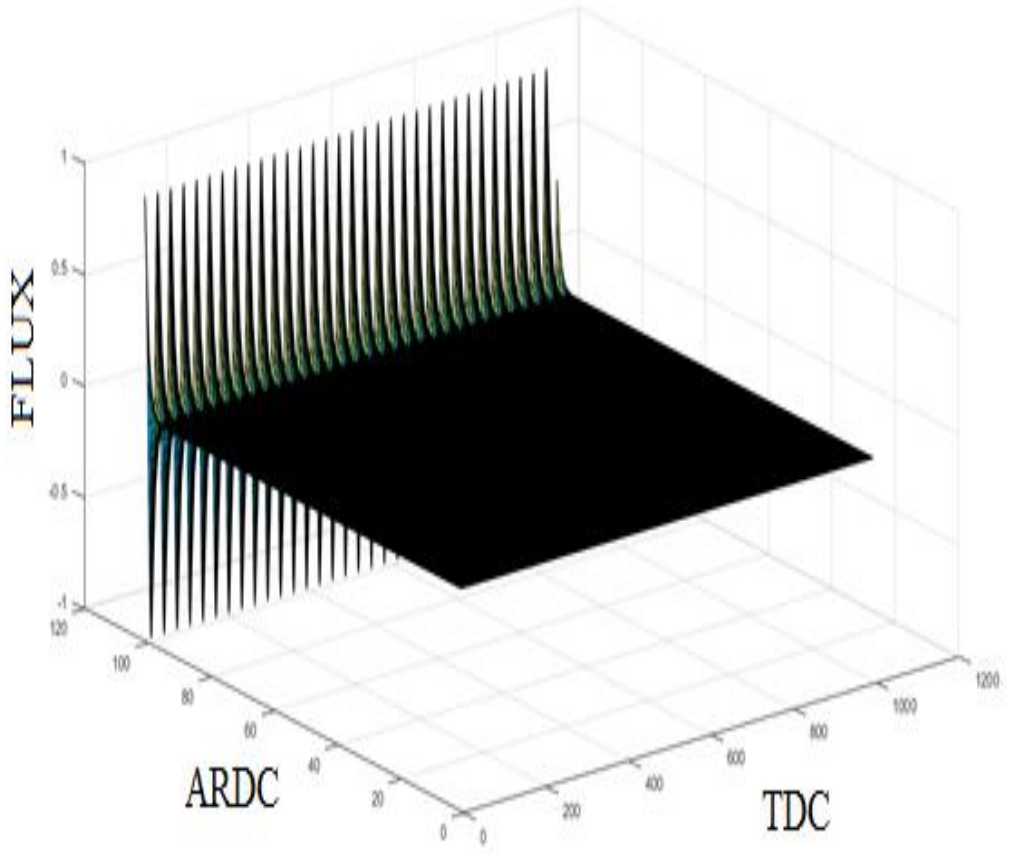

ANNEX 2: ANALYTICAL METHOD

1. Generation of Figure 4.25

```
a = [0:1:100];

 b = [0:1:100];

g1 = [0:0.1:100];

G = (i*a-b);

Y= G'*exp(g1);
```

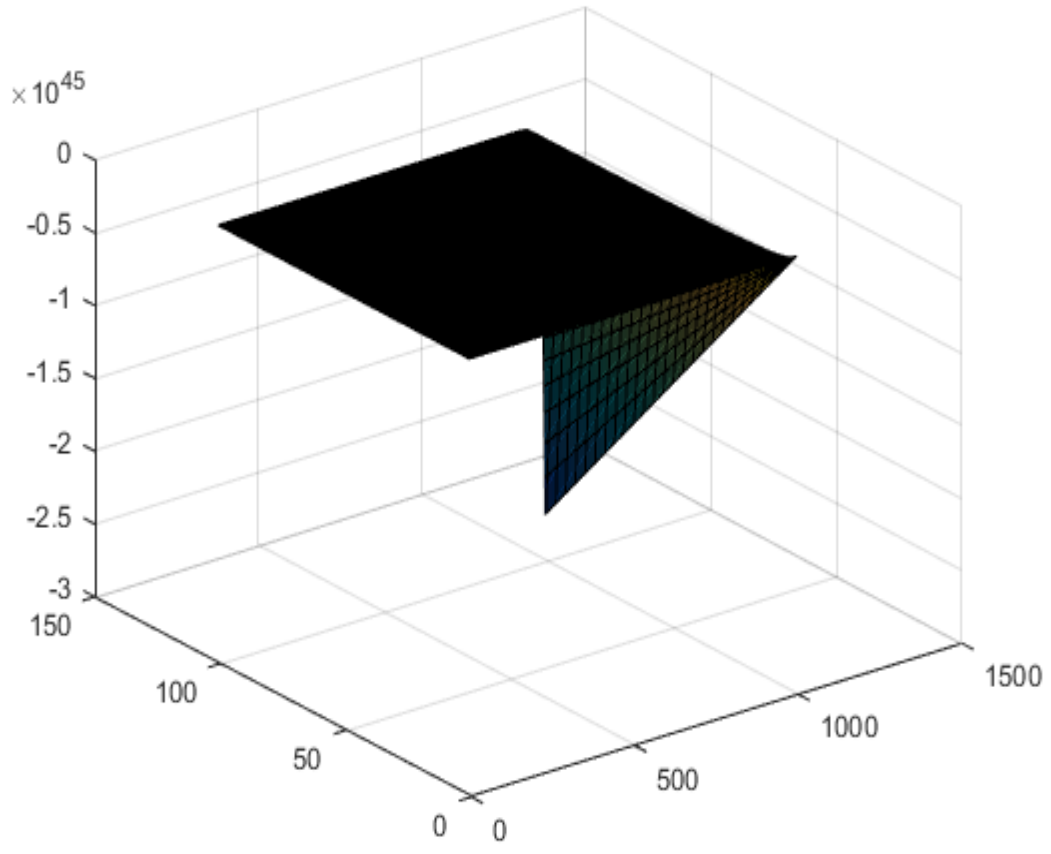

2. Generation of Figure 4.28

```
a = [0:1:100];

 b = [0:1:100];

g2 = [0:0.1:100];

G = (i*a-b);

Y= G'*exp(i*g2);
```

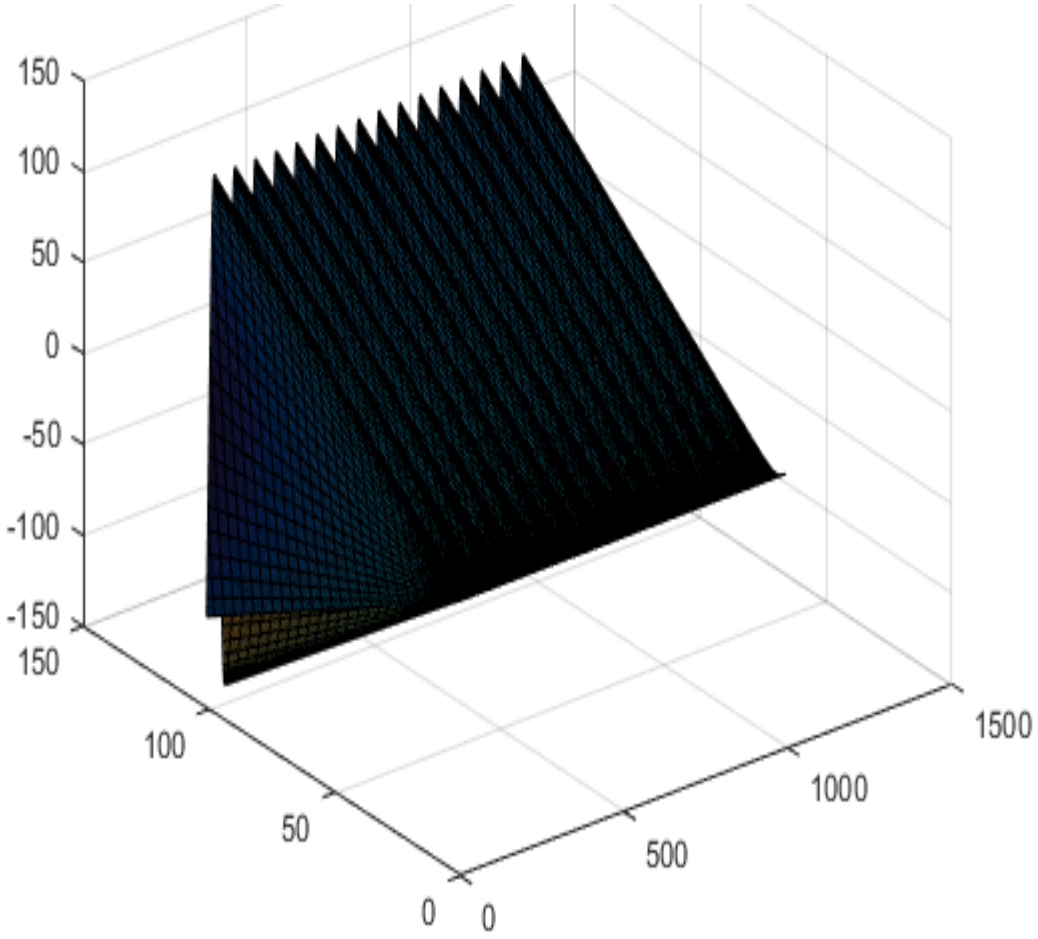

3. Generation of Figure 4.29

```
a = [0:1:100];

 b = [0:1:100];

g2 = [0:0.1:100];

G = (i*a-b);

Y= G'*exp(i*g2);
```

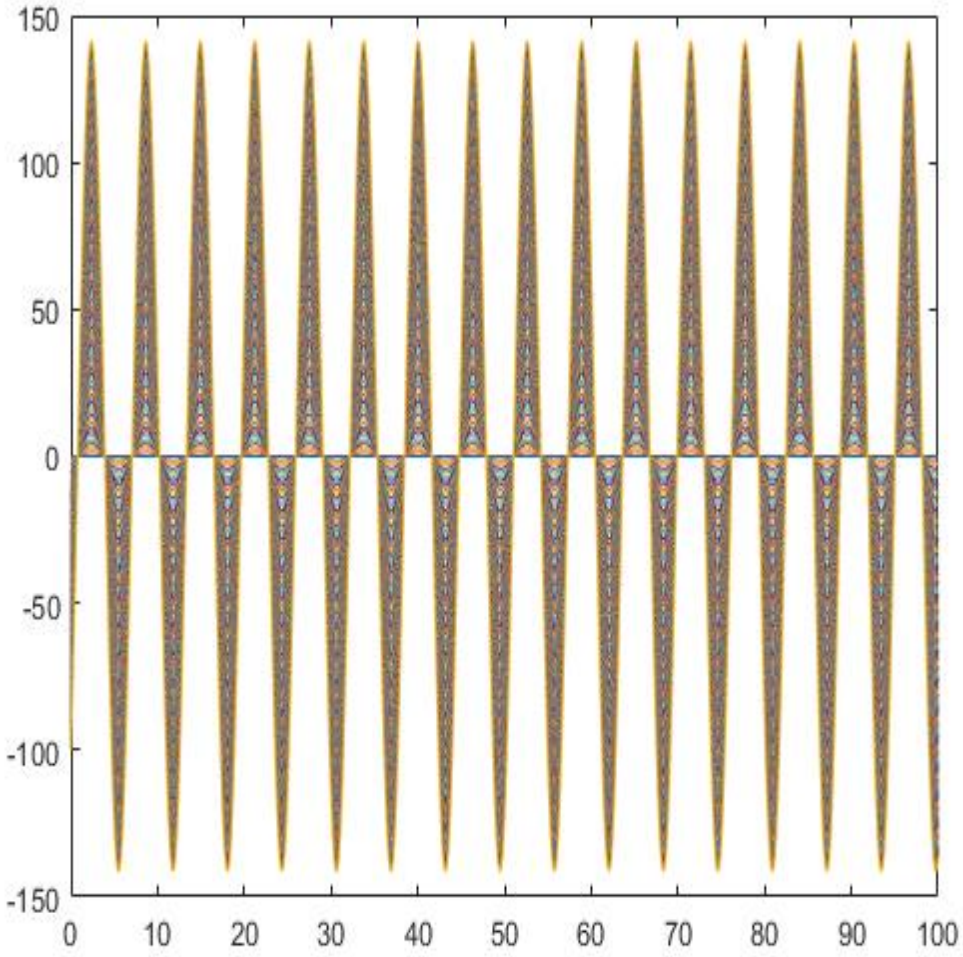

4. Generation of Figure 4.34

```
a = [0:1:10];

b = [0:1:10];

g1 = [0:0.1:10];

g2 = [0:0.1:10];

G = (i*a-b);

Y= G'*exp (g1+i*g2);
```

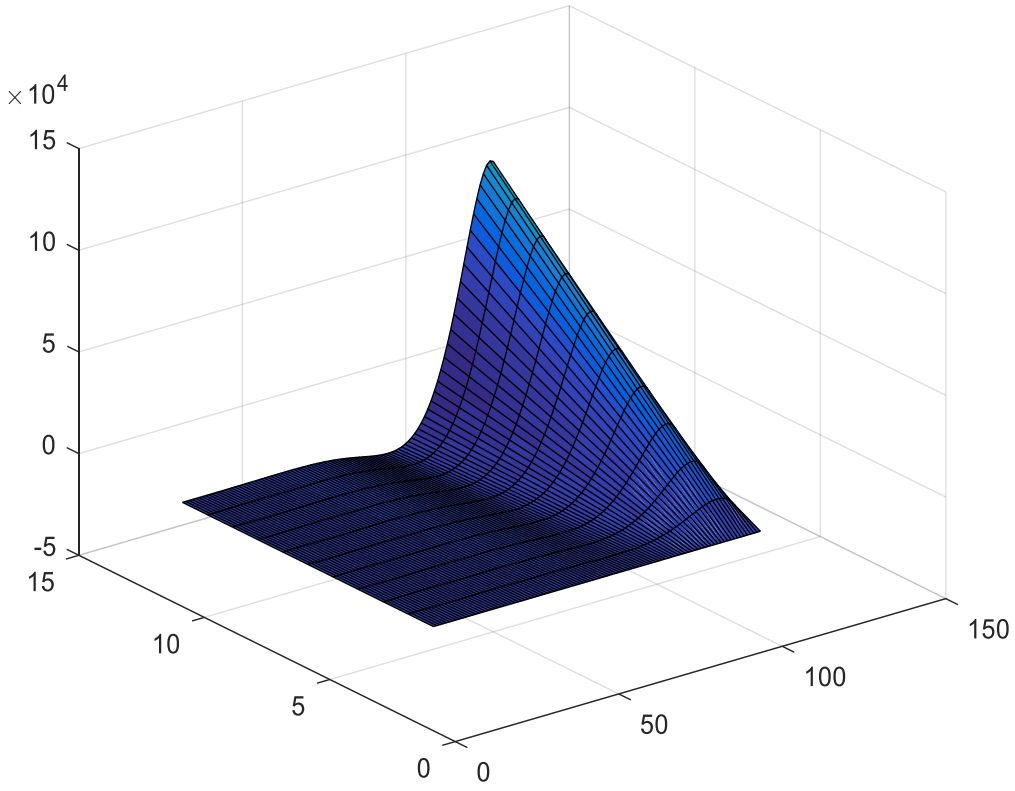

5. Generation of Figure 4.36(iii)

```
a = [0:1:100];

b = [0:1:100];

g1 = [0:0.1:100];

g2 = [0:0.1:100];

G = (i*a-b);

Y= G'*exp (g1-i*g2);
```

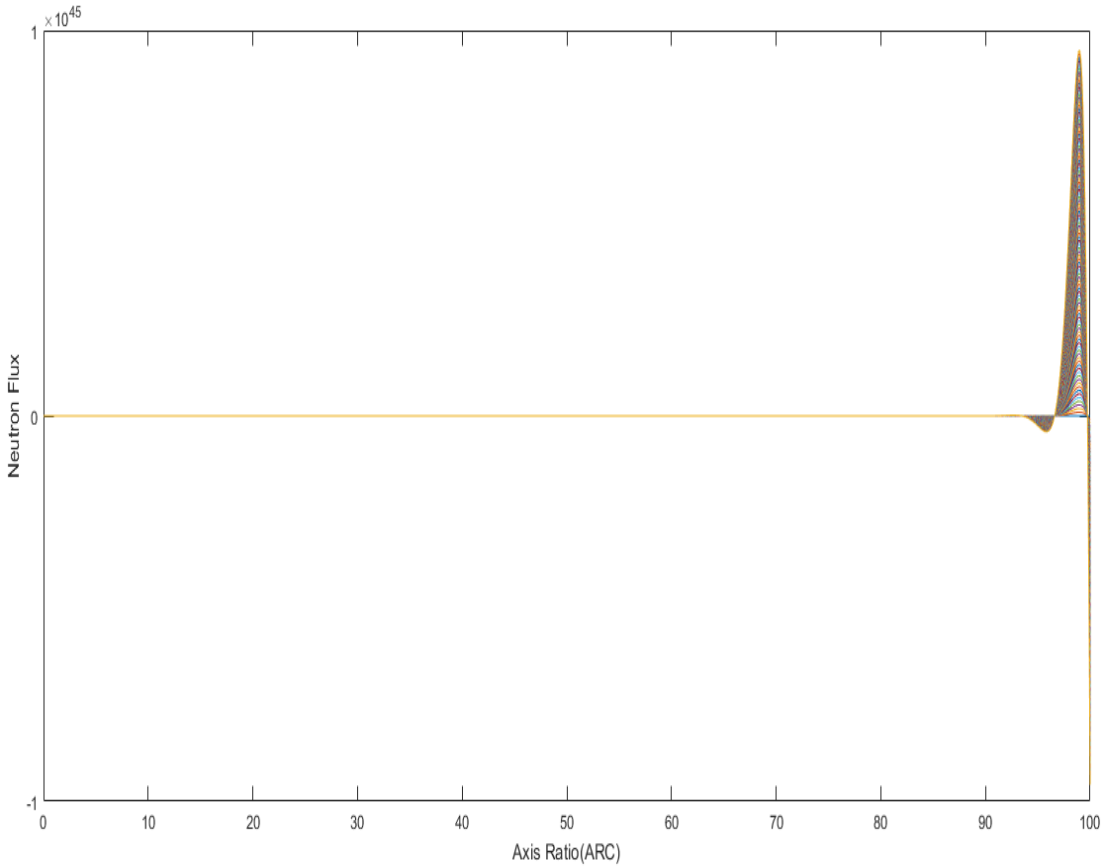

6. Generation of Figure 4.38

```
>> a=[0:1:100];

>> b=[0:1:100];

>> g1=[-1:0.01:1];

>> g2=[-1:0.01:1];

>> G=(i*a-b)';

>> Y=G*exp(i*g2-g1);
```

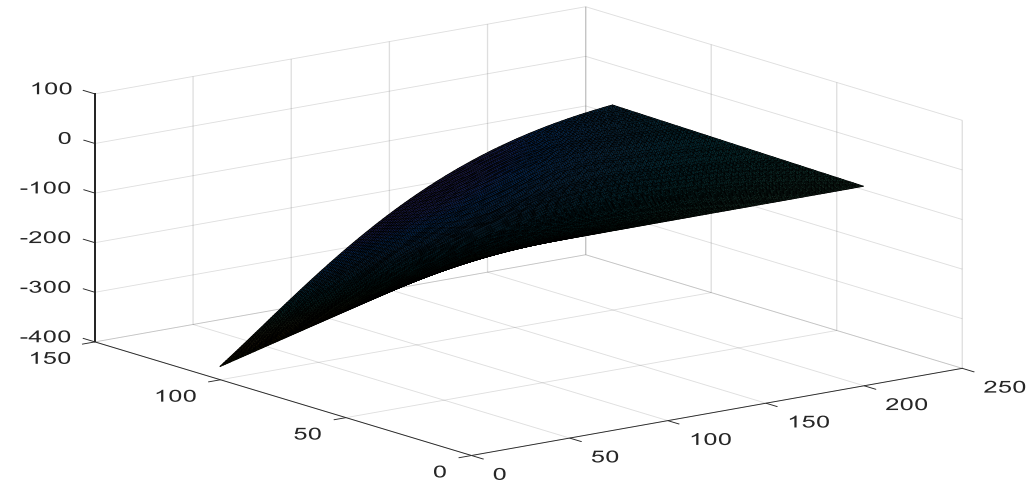

7. Generation of additional figure 1

```
a = [0:1:100];

 b = [0:1:100];

g1 = [0:0.1:100];

G = (i*a-b);

Y= G'*exp(g1);
```

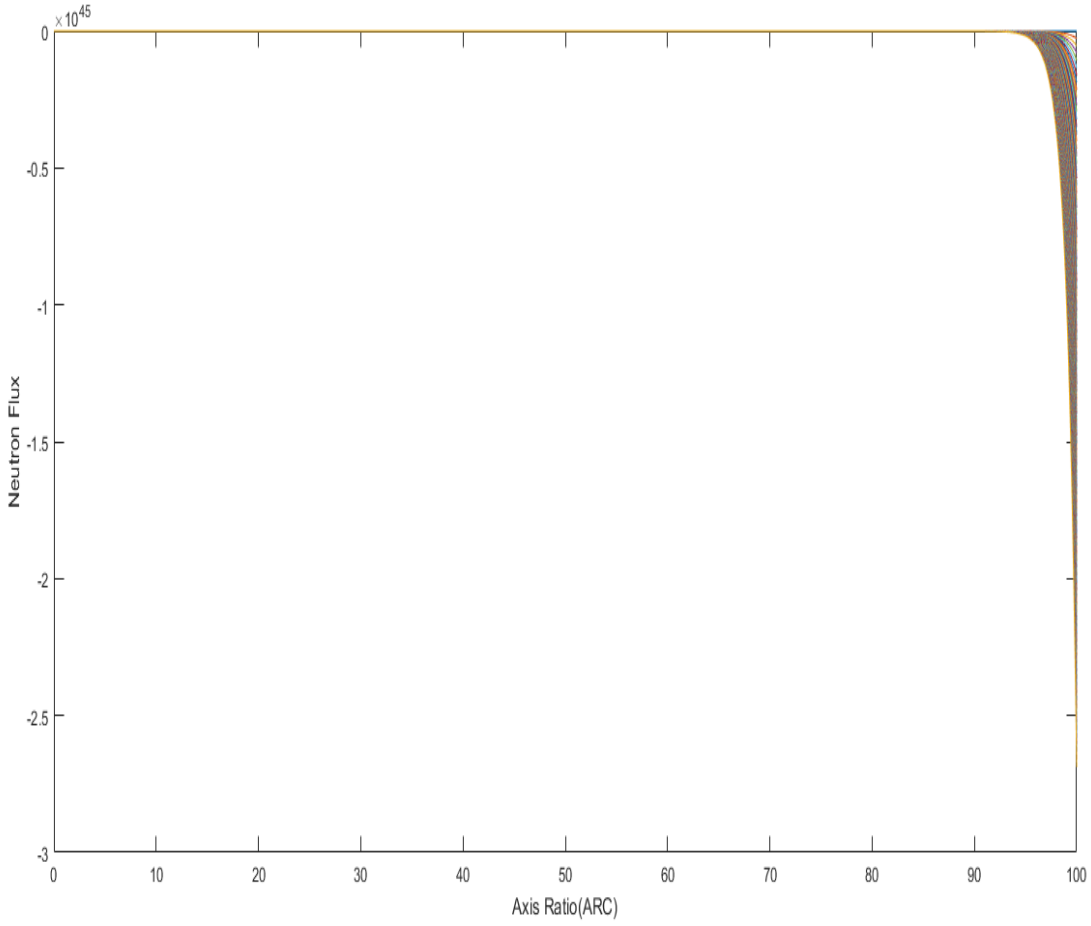

8. Generation of additional Figure 2

```
a = [0:1:10];

 b = [0:1:10];

g1 = [0:0.1:10];

g2 = [0:0.1:10];

G = (i*a-b);

Y= G'*exp (g1+i*g2);
```

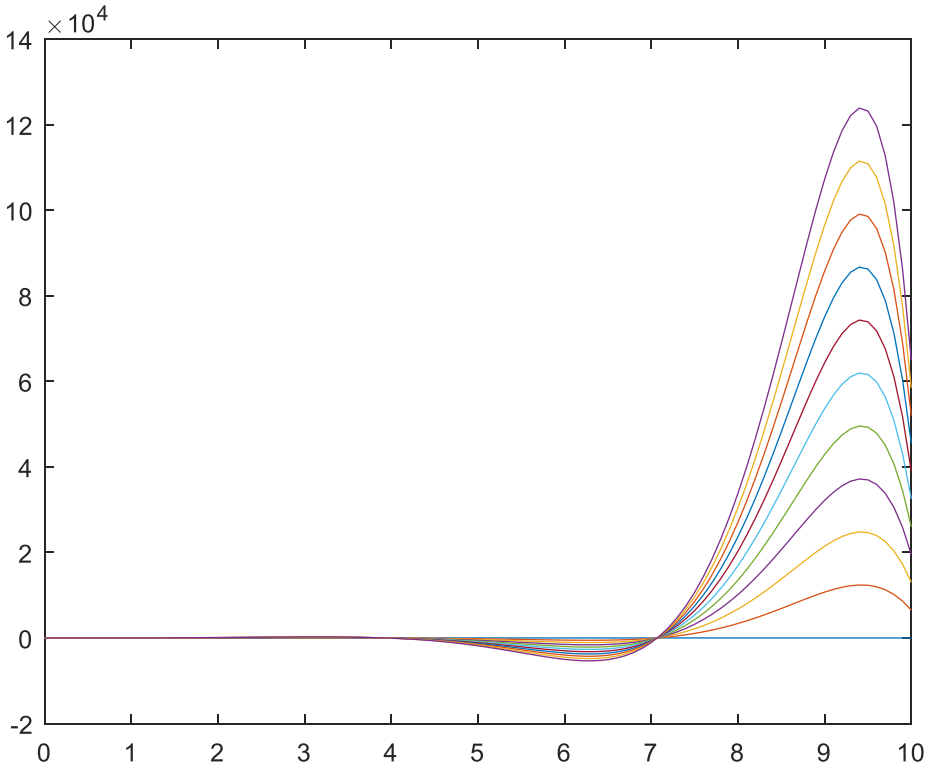

ANNEX 3: LEAKAGE RATES VERSUS AXIS RATIOs

1. Generation of Figure 4.41(ii)

Leakage rates (Prolate Spheroid)

```
k0=1;

k1=10;

k2=100;

k3=500;

k4=1000;

c=[0:0.01:10];

L0=((k0*c.^2)./(9.86+19.72*c.^2)).^0.5;

L1=((k1*c.^2)./(9.86+19.72*c.^2)).^0.5;

L2=((k2*c.^2)./(9.86+19.72*c.^2)).^0.5;

L3=((k3*c.^2)./(9.86+19.72*c.^2)).^0.5;

L4=((k4*c.^2)./(9.86+19.72*c.^2)).^0.5;

Plot(c,L0,c,L1,c,L2,c,L3,c,L4)
```

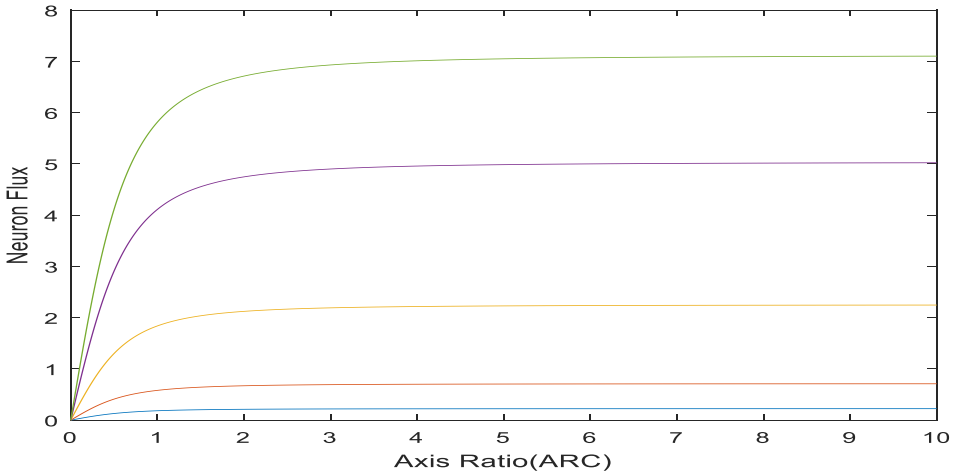

2. Generation of Figure 4.41(i)

Leakage rates(Oblate Spheroid)

```
k5=1;

k6=10;

k7=100;

k8=500;

k9=1000;

c=[0:0.01:10];

L5=((k5*c.^2)./(19.72+9.86*c.^2)).^0.5;

L6=((k6*c.^2)./(19.72+9.86*c.^2)).^0.5;

L7=((k7*c.^2)./(19.72+9.86*c.^2)).^0.5;

L8=((k8*c.^2)./(19.72+9.86*c.^2)).^0.5;

L9=((k9*c.^2)./(19.72+9.86*c.^2)).^0.5;

Plot(c,L5,c,L6,c,L7,c,L8,c,L9)
```

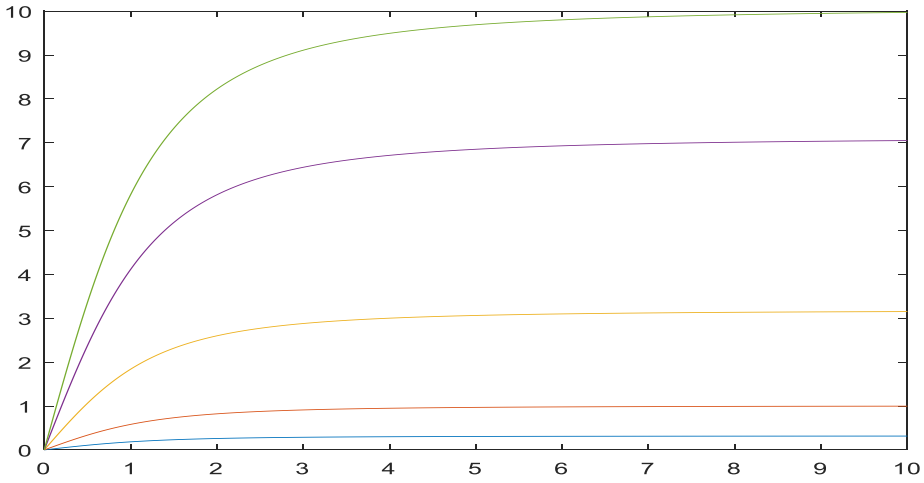

3. Generation of Figure 4.42

Combination of prolate and Oblate

```
k0=1;k1=10;k2=100;k3=500;k4=1000;c=[0:0.01:10];

L0=((k0*c.^2)./(9.86+19.72*c.^2)).^0.5;

L1=((k1*c.^2)./(9.86+19.72*c.^2)).^0.5;

L2=((k2*c.^2)./(9.86+19.72*c.^2)).^0.5;

L3=((k3*c.^2)./(9.86+19.72*c.^2)).^0.5;

L4=((k4*c.^2)./(9.86+19.72*c.^2)).^0.5;

L5=((k0*c.^2)./(19.72+9.86*c.^2)).^0.5;

L6=((k1*c.^2)./(19.72+9.86*c.^2)).^0.5;

L7=((k2*c.^2)./(19.72+9.86*c.^2)).^0.5;

L8=((k3*c.^2)./(19.72+9.86*c.^2)).^0.5;

L9=((k4*c.^2)./(19.72+9.86*c.^2)).^0.5;

plot(c,L0,c,L1,c,L2,c,L3,c,L4,c,L5,c,L6,c,L7,c,L8,c,L9);
```

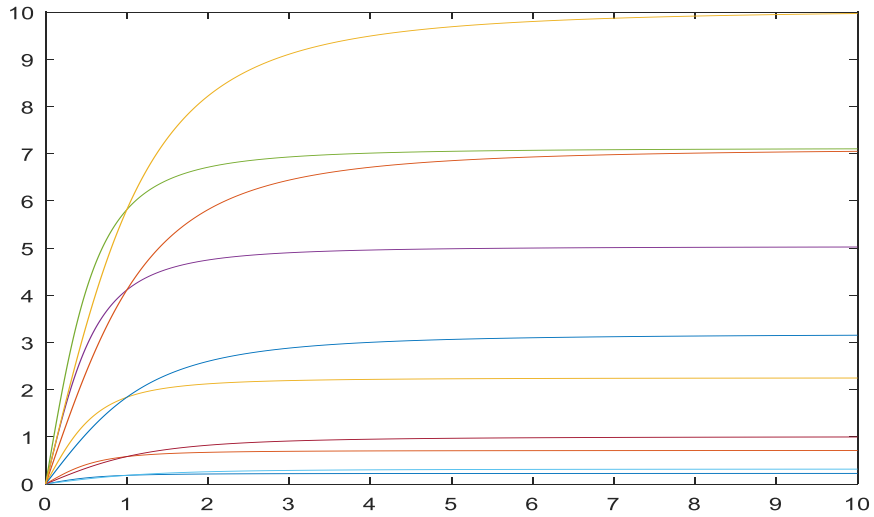

ANNEX 4: REACTIVITY VS AXIS RATIO

In Annex 4, during coding, substitutions were made as follows;- $O = \Omega$; $B = \beta$; $\rho = e$

1. Generation of Figure 4.43

Prolate

```
>> O=5;>> B1=0.1;>> B2=0.5;>> B3=1;>> B4=2.5;>> B5=5;>> c=[0:0.01:5];

>> e1=[1-((9.86+(19.72+B1)*c.^2)./(9.86+19.72*c.^2)*O)];

>> e2=[1-((9.86+(19.72+B2)*c.^2)./(9.86+19.72*c.^2)*O)];

>> e3=[1-((9.86+(19.72+B3)*c.^2)./(9.86+19.72*c.^2)*O)];

>> e4=[1-((9.86+(19.72+B4)*c.^2)./(9.86+19.72*c.^2)*O)];

>> e5=[1-((9.86+(19.72+B5)*c.^2)./(9.86+19.72*c.^2)*O)];

plot(c,e1,c,e2,c,e3,c,e4,c,e5)
```

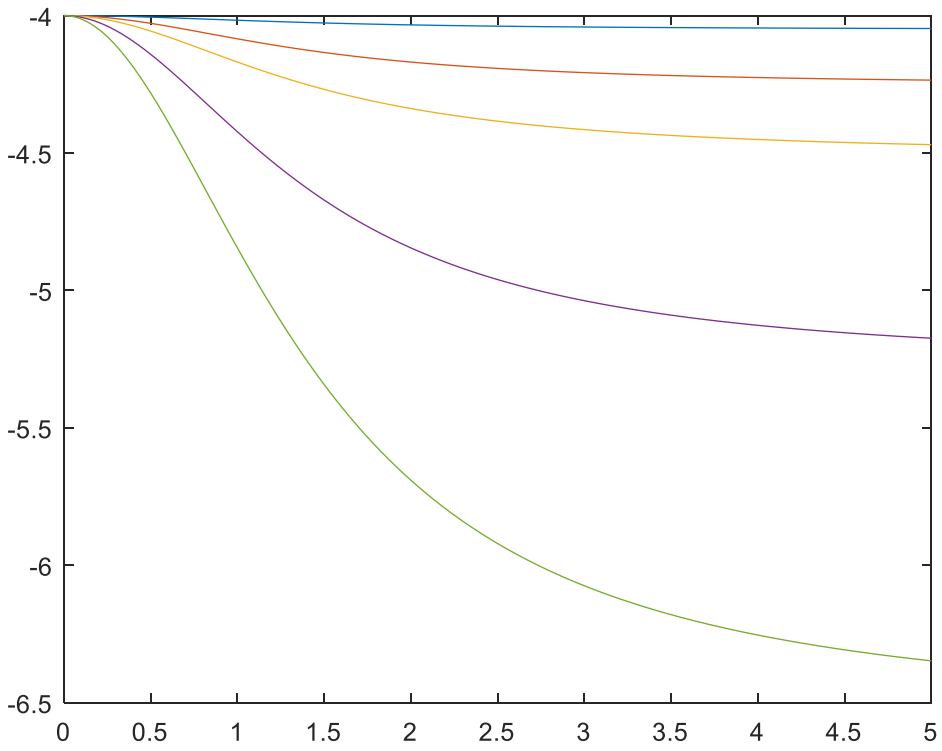

2. Generation of Figure 4.45

Combined

```
>> O=5;>> B1=0;>> B2=0.5;>> B3=1;>> B4=2;>> B5=5;>> c=[0:0.01:5];

>> e1=[1-((9.86+(19.72+B1)*c.^2)./(9.86+19.72*c.^2)*O)];

>> e2=[1-((9.86+(19.72+B2)*c.^2)./(9.86+19.72*c.^2)*O)];

>> e3=[1-((9.86+(19.72+B3)*c.^2)./(9.86+19.72*c.^2)*O)];

>> e4=[1-((9.86+(19.72+B4)*c.^2)./(9.86+19.72*c.^2)*O)];

>> e5=[1-((9.86+(19.72+B5)*c.^2)./(9.86+19.72*c.^2)*O)];

>> e6=[1-((19.72+(9.86+B1)*c.^2)./(19.72+9.86*c.^2)*O)];

>> e7=[1-((19.72+(9.86+B2)*c.^2)./(19.72+9.86*c.^2)*O)];

>> e8=[1-((19.72+(9.86+B3)*c.^2)./(19.72+9.86*c.^2)*O)];

>> e9=[1-((19.72+(9.86+B4)*c.^2)./(19.72+9.86*c.^2)*O)];

>> e10=[1-((19.72+(9.86+B5)*c.^2)./(19.72+9.86*c.^2)*O)];

plot(c,e1,c,e2,c,e3,c,e4,c,e5,c,e6,c,e7,c,e8,c,e9,c,e10)
```

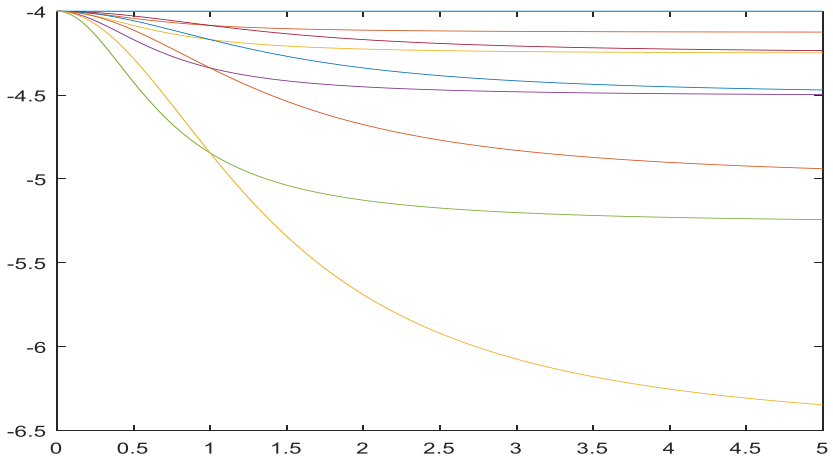

3. Generation of Figure 4.46

Combined(B5)

```
>> B=5;>> O1=0;>> O2=0.5;>> O3=1;>> O4=2;>> O5=5;>> c=[0:0.01:5];

>> e1=[1-((9.86+(19.72+B)*c.^2)./(9.86+19.72*c.^2)*O1)];

>> e2=[1-((9.86+(19.72+B)*c.^2)./(9.86+19.72*c.^2)*O2)];

>> e3=[1-((9.86+(19.72+B)*c.^2)./(9.86+19.72*c.^2)*O3)];

>> e4=[1-((9.86+(19.72+B)*c.^2)./(9.86+19.72*c.^2)*O4)];

>> e5=[1-((9.86+(19.72+B)*c.^2)./(9.86+19.72*c.^2)*O5)];

>> e6=[1-((19.72+(9.86+B)*c.^2)./(19.72+9.86*c.^2)*O1)];

>> e7=[1-((19.72+(9.86+B)*c.^2)./(19.72+9.86*c.^2)*O2)];

>> e8=[1-((19.72+(9.86+B)*c.^2)./(19.72+9.86*c.^2)*O3)];

>> e9=[1-((19.72+(9.86+B)*c.^2)./(19.72+9.86*c.^2)*O4)];

>> e10=[1-((19.72+(9.86+B)*c.^2)./(19.72+9.86*c.^2)*O5)];

plot(c,e1,c,e2,c,e3,c,e4,c,e5,c,e6,c,e7,c,e8,c,e9,c,e10);
```

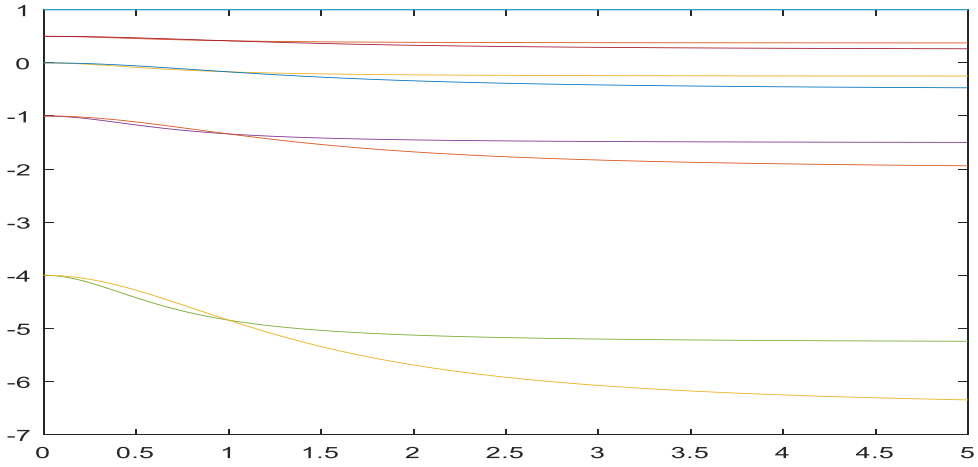

4. Generation of Figure 4.47

```
>> B=10;>> O1=0;>> O2=0.5;>> O3=1;>> O4=2;>> O5=5;>> c=[0:0.01:5];

>> e1=[1-((9.86+(19.72+B)*c.^2)./(9.86+19.72*c.^2)*O1)];

>> e2=[1-((9.86+(19.72+B)*c.^2)./(9.86+19.72*c.^2)*O2)];

>> e3=[1-((9.86+(19.72+B)*c.^2)./(9.86+19.72*c.^2)*O3)];

>> e4=[1-((9.86+(19.72+B)*c.^2)./(9.86+19.72*c.^2)*O4)];

>> e5=[1-((9.86+(19.72+B)*c.^2)./(9.86+19.72*c.^2)*O5)];

>> e6=[1-((19.72+(9.86+B)*c.^2)./(19.72+9.86*c.^2)*O1)];

>> e7=[1-((19.72+(9.86+B)*c.^2)./(19.72+9.86*c.^2)*O2)];

>> e8=[1-((19.72+(9.86+B)*c.^2)./(19.72+9.86*c.^2)*O3)];

>> e9=[1-((19.72+(9.86+B)*c.^2)./(19.72+9.86*c.^2)*O4)];

>> e10=[1-((19.72+(9.86+B)*c.^2)./(19.72+9.86*c.^2)*O5)];

plot(c,e1,c,e2,c,e3,c,e4,c,e5,c,e6,c,e7,c,e8,c,e9,c,e10);
```